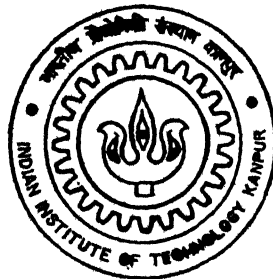


# **ASSESSMENT OF STRUCTURAL INTEGRITY OF A NUCLEAR REACTOR PRESSURE VESSEL WITH A NOZZLE - CORNER CRACK USING FEM**

**By**

**Vivek Shrivastav**



**NUCLEAR ENGINEERING AND TECHNOLOGY PROGRAM  
INDIAN INSTITUTE OF TECHNOLOGY KANPUR**

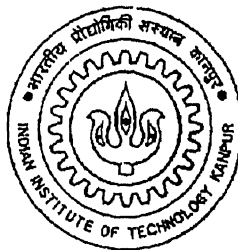
**AUGUST, 2003**

# **ASSESSMENT OF STRUCTURAL INTEGRITY OF A NUCLEAR REACTOR PRESSURE VESSEL WITH A NOZZLE-CORNER CRACK USING FEM**

A Thesis Submitted  
In Partial Fulfillment of the Requirements  
for the Degree of  
**Master of Technology**

by

Vivek Shrivastav



to the

**NUCLEAR ENGINEERING AND TECHNOLOGY PROGRAM  
INDIAN INSTITUTE OF TECHNOLOGY KANPUR  
INDIA**

August, 2003

*Dedicated to*

*The vision of a developed India,*

*My Parents and Sister*

*and*

*Maa Saraswati.*

25 SEP 2003

पुरुषोत्तम क. गीनाथ केजकर पुस्तकालय  
भारतीय प्रौद्योगिकी संस्थान काठपुर  
अवधि क्र० A. .... 145108



A145108

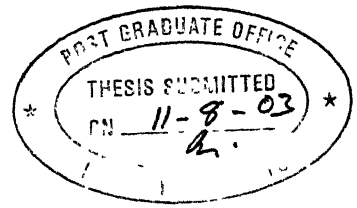
*Dedicated to*

*The vision of a developed India,*

*My Parents and Sister*

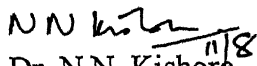
*and*

*Maa Saraswati.*



## CERTIFICATE

It is certified that the work contained in the thesis entitled “**Assessment of Structural Integrity of a Nuclear Reactor Pressure Vessel with a Nozzle-Corner Crack using FEM**”, by **Mr. Vivek Shrivastav**, has been carried out under our supervision and that this work has not been submitted elsewhere for a degree.

  
Dr. N.N. Kishore

Professor and Head,  
Deptt. of Mechanical Engineering,  
Indian Institute of Technology,  
Kanpur.



Dr. Prashant Kumar  
Professor,  
Deptt. of Mechanical Engineering,  
Indian Institute of Technology,  
Kanpur.

August, 2003.

# Acknowledgements

This work has made me realize that any good work is a result of efforts of many, may be directly or indirectly. I think it would not be an exaggeration if I address the present work as a team work. First and foremost, I would like to express my deep sense of respect and admiration for my thesis supervisor **Dr. N.N. Kishore**.

My interaction with Dr. Kishore began during my course work, when I took up the FEM course offered by him. It was right from then, that I started admiring him, and I felt very happy when I was told that I will be doing my thesis work under his supervision.

I would like to mention a small incident here. In the very early stages of my work, I took a plot of stress variation along a particular path of the structure I have worked upon, and showed it to Dr. Kishore. Without asking what the plot was about, he said “this is wrong”. I was surprised how he could tell that it was wrong. On the other hand I did not want to believe that it was wrong, after all, I had spent weeks to get to it. Anyhow, I worked out the things again, spent another week over it and finally found that it was wrong indeed. When I looked at the right plot and compared it with the wrong one, I realized that the things that occur naturally are usually very systematic, while my previous plot was far from being so.

I thank Dr. N.N. Kishore for his invaluable guidance, numerous discussions and suggestions, constant encouragements, patient listening that he gave to my problems, and for all the knowledge that I have acquired from him. His friendly way of interacting and systematic approach made the work enjoyable. I am indebted to him for encouraging me to work on crack growth analysis, which is a rather difficult job in 3D.

I thank **Dr. Prashant Kumar**, my thesis co-supervisor, for introducing me to the wonderful subject of Fracture Mechanics and for putting me on the right track when I was about to begin my work. During his course, I and my colleague Amit Pawar tried to do an experiment for the determination of critical Stress Intensity Factor of EN24, under his guidance, as our term project. Although the experiment could not be completed successfully in time, but we learnt a lot. We realized what kind of effort goes in to such a work.

Special thanks go to **Dr. Sumit Basu** for generously helping me out in my effort to do a 3D quasi static crack growth analysis using cohesive zone technique. In fact he is the person who

introduced me to the cohesive zone technique. I thank him for always finding out time for discussions in spite of his busy schedule. I appreciate and admire the modesty of Dr. Basu, who has been so kind to personally come to my lab and sit with me at times when I was stuck.

I would also like to express my deep sense of love and gratitude for my institute, the **Indian Institute of Technology, Kanpur**. This work would not have been possible without the excellent facilities provided by the institute; the computational facilities, the digital subscription of journals, the grand central library, just to name a few. The beautiful work culture, high learning rate and the overall atmosphere of the campus have brought major significant improvements in my personality, attitude and thinking.

I express my deep gratitude to the **Department of Atomic Energy** for sponsoring my M.Tech. program at IIT Kanpur. I thank the Pressure Vessels Section of the Light Water Reactor Division of **Bhabha Atomic Research Centre** for providing me the opportunity to work on the present problem. Special thanks go to **Mr. R.N. Sen** and **Mr. R.S. Yadav** of the Light Water Reactor Division for their invaluable suggestions and discussions during my one month stay in BARC, which was intended to understand the problem and get the micro details required.

At this moment of success and satisfaction, I am not able to find words which can suitably thank my parents **Smt. Shobha Shrivastav** and **Shri Deen Bandhu Shrivastav**, and my sister **Archana Shrivastav**, because of whom, today I am, what I always wanted to be. I thank them from the bottom of my heart for all their support, inspiration and encouragement.

I sincerely thank my classmate **U.B. Jayadeep** who familiarized me with the Finite Element code ANSYS and always made himself available whenever I was stuck with the software. I express my sincere thanks to my lab-mates **Bhanu** and **Mukul Shukla** sir who made me familiar with the Finite Element code ABAQUS and always helped me in figuring out the associated problems through discussions and personal involvement. In this context, I would also like to thank **Ms. Renuka Srinivasan** of the ABAQUS customer support, who helped me figuring out the problems associated with the software over e-mails.

I thank my juniors **Vinay Pahlajani** and **Rajat Saxena** for extending their support and concern for the success of my work. Vinay helped me a lot in modeling the geometry of my problem in IDEAS, which I needed specifically for crack growth analysis in ABAQUS. Rajat helped me a lot by taking care of my extra-academic jobs during the final stages of my work, due to which I could completely concentrate on the work.



I thank the **NET-SMD** brigade, comprising of Amit Pawar, Manas Ranjan Gartia, Vinay Kumar, Amar Singh, Rajit Ram, Rajneesh Chaudhary, Suryaprakash Dewangan, Sudesh Pandit, Sachin Singh Gautam, Rajiv Sharma, Saurabh Naik, Rajat Saxena and Santosh Rao, for all the affection, help and support that they extended to me during my two-year stay at IITK, and for all those moments of cherish that we enjoyed together. Particularly, I would like to thank Pawar, Sachin, Naik, Rajat, Vinay and Manas for the technical discussions that we have been doing.

Finally, I thank the **Almighty** for always showing me the right path and providing me the strength and courage to move on.

August 7, 2003  
IIT Kanpur

Vivek Shrivastav

# Abstract

Nuclear energy is emerging as a major alternative to the rapidly depleting conventional sources of energy. Safety is one of the major concerns of the nuclear power industry. The pressure vessel containing the nuclear reactor assembly has a number of inlet and outlet nozzles welded to it. It is important to demonstrate the structural integrity of the containment vessel to ensure a safe operation. One of the most important aspects in this regard is the consideration of the surface cracks in the crotch region of the nozzle-vessel intersection, called nozzle-corner cracks.

The crack characterizing parameter, stress intensity factor, is used to estimate the severity of a crack, within the framework of Linear Elastic Fracture Mechanics. Due to the complexity of geometry, the stress intensity factor for nozzle-corner cracks can only be evaluated using either approximate methods, or more accurately, by using numerical techniques such as the Finite Element method.

In the present work, the Finite Element method has been used to evaluate the stress intensity factor variation along the profile of a nozzle-corner crack, modeled as a quarter ellipse, in a given nozzle-vessel intersection. Two types of load conditions have been considered: A simple internal pressure load, representing the normal operational condition; and a pressurized thermal shock, representing a faulted or accidental condition.

Firstly, for the normal operational condition, a three-dimensional static stress analysis of the nozzle-vessel intersection without crack has been performed to demonstrate the validity of the partial modeling of the structure and the boundary conditions used. The corner crack is then included in the model and the stress analysis has been repeated, with singular elements near the crack front. Stress intensity factor has been evaluated from the displacement field near the crack profile, as obtained from the stress analysis. The results have been validated by solving two test problems and also by comparison with an empirical formula. Parametric study has been done for different crack and geometrical parameters.

Secondly, for the faulted condition, a given crack configuration, with crack depth equal to half the vessel thickness, has been studied. A transient thermal stress analysis has been performed and the stress intensity factors have been evaluated at different points in the time domain, and are compared with the critical stress intensity factor for crack initiation. The particular half-thickness crack considered here has been estimated to be critical.

Further, as an attempt towards the estimation of stable growth of nozzle-corner cracks, a three-dimensional formulation of the cohesive-zone method for crack growth analysis has been presented. The method has been applied for the crack growth analysis of a Double Cantilever Beam Specimen and the results have been found to match qualitatively well with the available literature. The method is then applied for the estimation of growth of a given nozzle-corner crack under normal operational load and the pattern of crack growth has been found to be consistent with the SIF results obtained.

# Contents

1. INTRODUCTION.....	1
1.1 General Introduction .....	1
1.2 Literature Review.....	4
1.3 Overview of the Present Work.....	6
1.4 Organization of the Thesis .....	7
2. FE FORMULATIONS FOR STRESS AND HEAT TRANSFER ANALYSES .....	8
2.1 Introduction .....	8
2.2 FE Formulation for 3D Static Stress Analysis.....	8
2.3 FE Formulation for 3D Transient Heat Transfer Analysis.....	13
2.4 Closure .....	17
3. STRESS ANALYSIS OF UNCRACKED NOZZLE-VESSEL INTERSECTION.....	18
3.1 Introduction .....	18
3.2 Geometry.....	18
3.3 Material .....	19
3.4 Solid Modeling and FE Analysis .....	20
3.4.1 Load and Boundary Conditions .....	22
3.5 Results and Discussion.....	23
3.6 Closure .....	30

4. EFFECT OF NORMAL OPERATIONAL LOAD ON NOZZLE-CORNER CRACKS	
4.1 Introduction.....	31
4.2 Crack Configuration.....	31
4.3 FE Modeling and Analysis.....	33
4.3.1 Load and Boundary Conditions .....	37
4.3.2 Comparison of Results for Full and Half Models .....	37
4.4 Stress Analysis Results and Discussion .....	38
4.5 Stress Intensity Factor .....	46
4.6 SIF for Three-Dimensional Crack Problems.....	49
4.7 Numerical Evaluation of SIF .....	50
4.8 SIF Results and Discussion.....	54
4.9 Validation of SIF Results .....	56
4.9.1 2D Test Problem .....	56
4.9.2 3D Test Problem .....	57
4.9.3 Comparison with Approximate Empirical Formula.....	57
4.10 Parametric Study .....	61
4.10.1 Normalization of the Parameters.....	61
4.10.2 Discussion .....	62
4.11 Closure .....	69
5. EFFECT OF LOCA ON NOZZLE-CORNER CRACKS .....	70
5.1 Introduction .....	70
5.2 Problem Definition.....	71
5.3 FE Modeling and Analysis.....	73

5.4	Results and Discussion.....	74
5.5	Closure .....	80
6.	ESTIMATION OF STABLE CRACK GROWTH.....	81
6.1	Introduction .....	81
6.2	Constitution of the Cohesive Zone.....	82
6.3	Finite element Formulation .....	84
6.3.1	Variational form of the boundary value problem.....	84
6.3.2	Finite element discretization .....	88
6.3.2	Global assembly .....	92
6.4	Crack Growth Analysis .....	93
6.4.1	One Element Tension Test Problem .....	94
6.4.2	Crack Growth Analysis of a DCB Specimen.....	96
6.4.3	Crack Growth Analysis of a nozzle-corner crack .....	99
6.4.4	Results and Discussion.....	100
6.5	Closure .....	107
7.	CONCLUSIONS AND SCOPE FOR FUTURE WORK.....	108
7.1	Conclusions .....	108
7.2	Scope for Future Work.....	109
	References .....	110

# List of Figures and Tables

Figure 2.1 Domain and Boundary Conditions for Stress Analysis. ....	9
Figure 2.2 Domain and Boundary Conditions for Heat Transfer Analysis.....	9
Figure 3.1 Geometry of the nozzle-vessel intersection.....	19
Figure 3.2 Solid model of nozzle-vessel intersection. ....	21
Figure 3.3 FE Discretization of the model. ....	22
Figure 3.4 Stresses on the inside of the vessel (Path A-B). ....	24
Figure 3.5 Stresses on the outside of the vessel (Path C-D). ....	25
Figure 3.6 Stresses on the inside of the nozzle (Path A-E). ....	25
Figure 3.7 Stresses on the outside of the nozzle (Path C-F). ....	26
Figure 3.8 Hoop stress on the inside of the vessel (Path A-B). ....	26
Figure 3.9 Longitudinal stress on the inside of the vessel (Path A-B).....	27
Figure 3.10 Hoop stress on the outside of the vessel (Path C-D). ....	27
Figure 3.11 Longitudinal stress on the outside of the vessel (Path C-D).....	28
Figure 3.12 Hoop stress on the inside of the nozzle (Path A-E). ....	28
Figure 3.13 Longitudinal stress on the inside of the nozzle (Path A-E). ....	29
Figure 3.14 Hoop stress on the outside of the nozzle (Path C-F). ....	29
Figure 3.15 Longitudinal stress on the outside of the nozzle (Path C-F).....	30
Figure 4.1 Crack Configuration and dimensional parameters. ....	32
Figure 4.2 Solid model of nozzle-vessel intersection with corner crack. ....	33
Figure 4.3 Enlarged view of the near-crack region. ....	34
Figure 4.4 FE discretization of the near-crack region.....	35

Figure 4.5 Half model with definitions of paths and coordinate axes. ....	36
Figure 4.6 Stress in X-direction along path G-H. ....	39
Figure 4.7 Stress in Y-direction along path G-H. ....	39
Figure 4.8 Stress in Z-direction along path G-H. ....	40
Figure 4.9 Stress in X-direction along path I-J. ....	40
Figure 4.10 Stress in Y-direction along path I-J. ....	41
Figure 4.11 Stress in Z-direction along path I-J. ....	41
Figure 4.12 Stress in X-direction along the crack front. ....	42
Figure 4.13 Stress in X-direction along Path A-B. ....	42
Figure 4.14 Stress in Y-direction along Path A-B. ....	43
Figure 4.15 Stress in Z-direction along Path A-B. ....	43
Figure 4.16 Stress in X-direction along Path A-E. ....	44
Figure 4.17 Stress in Y-direction along Path A-E. ....	44
Figure 4.18 Stress in Z-direction along Path A-E. ....	45
Figure 4.19 Square root nature of singularity near the crack tip along Path A-B. ....	45
Figure 4.20 Square root nature of singularity near the crack tip along Path A-E. ....	46
Figure 4.21 Through-thickness Crack in an infinite flat plate. ....	47
Figure 4.22 Stress field around an embedded elliptical flaw. ....	47
Figure 4.23 Quarter point Elements for simulation of singularity. ....	52
Figure 4.24 Variation of SIF along the crack front for Crack-I. ....	55
Figure 4.25 Variation of SIF along the crack front for Crack-II. ....	55
Figure 4.26 SENB specimen (2D test problem). ....	59



Figure 4.27 Geometry of the 3D test problem. ....	59
Figure 4.28 Comparison of SIF for 3D test problem. ....	60
Figure 4.29 Comparison of SIF for 80 mm deep qtr-circular nozzle-corner crack with the results obtained from empirical formula [9]. ....	60
Figure 4.30 Variation of SIF along the profiles of cracks with different depths for the given Geometry. ....	63
Figure 4.31 Variation of SIF along the profiles of cracks with different depths for three different Geometries. ....	64
Figure 4.32 Variation of SIF along the profile of an 80 mm deep crack for two different Geometries. ....	64
Figure 4.33 Variation of SIF along the profile of an 80 mm deep crack for three different Geometries. ....	65
Figure 4.34 Variation of SIF along the profiles of cracks with a given depth for three different aspect ratios. ....	65
Figure 4.35 Variation of normalized SIF along the profiles of cracks with a given depth for three different aspect ratios. ....	66
Figure 4.36 Variation of normalized average SIF with respect to crack aspect ratio for a given Geometry and crack depth. ....	66
Figure 4.37 Variation of normalized average SIF with respect to normalized crack depth for a given Geometry. ....	67
Figure 4.38 Variation of normalized average SIF with respect to $d/D$ . ....	67
Figure 4.39 Variation of normalized average SIF with respect to $t/T$ . ....	68
Figure 4.40 Variation of normalized average SIF with respect to $D/T$ . ....	68
Figure 5.13 Given PTS transient. ....	72
Figure 5.14 Variation of temperature along the crack front (Time points 1-5). ....	76
Figure 5.15 Variation of temperature along the crack front (Time points 6-10). ....	76
Figure 5.16 Variation of temperature along the crack front (Time points 11-15). ....	77
Figure 5.17 Variation of SIF along the crack front (Time points 1-5). ....	77

Figure 5.18 Variation of SIF along the crack front (Time points 6-10).....	78
Figure 5.7 Variation of SIF along the crack front (Time points 11-15).....	78
Figure 5.19 Variation of vessel side SIF with time.....	79
Figure 5.20 Variation of nozzle side SIF with time.....	79
Figure 5.21 Variation of average SIF with time. ....	80
Figure 6.1 Solid body with fixed and moving boundaries (cracks). ....	83
Figure 6.2 Local coordinate system defined for each element.....	83
Figure 6.3 Traction-displacement relationship for a pure normal separation. ....	85
Figure 6.4 Separation of Cohesive zone from the bulk material.....	85
Figure 6.5 Parent element for interpolation and integration. ....	90
Figure 6.6 Crack opening displacement in Mode I. ....	90
Figure 6.7 One-element Tension test problem.....	95
Figure 6.8 Response of the cohesive element under Tension test problem. ....	95
Figure 6.9 Crack growth analysis of a DCB Specimen. ....	96
Figure 6.10 Crack propagation with increasing load line displacement. ....	97
Figure 6.11 Variation of crack opening load with the load-line displacement. ....	98
Figure 6.12 Crack growth resistance curve.....	98
Table 3.1 Chemical composition of SA 508-Class 3 steel.....	20
Table 3.2 Material Properties for SA 508-Class 3 steel.....	20
Table 5.3 Given PTS transient. ....	72

# **Chapter 1**

## **INTRODUCTION**

### **1.1 General Introduction**

Pressure vessels are leak-proof containers supposed to sustain high temperature and pressure, usually under adverse environmental conditions, which typically include corrosion, neutron bombardment, hydrogen embrittlement, etc. The ever-increasing use of vessels for storage, industrial processing, power generation, chemical industries, space and nuclear applications has given special emphasis to analytical and experimental methods for determining their operating stresses. High pressures, extremes of temperature, severity of functional performance requirements, and above all, safety requirements, pose exacting design problems. One of the key aspects of design is the identification of the most likely modes of damage or failure.

Especially, when it comes to applications like nuclear power generation, the requirements of safety increase manifolds. With the rapid depletion of the conventional sources of energy, nuclear energy is emerging as a major alternative. Owing to the abundant thorium reserves, India has a huge potential for the nuclear power industry. This makes the integrity of containment systems of nuclear reactors, an important field of study. One of the most significant modes of failure of nuclear reactor pressure vessels is fracture. Fracture could be initiated at existing defects or at cracks grown to a critical size by fatigue.

Pressure vessels usually have a number of inlet and outlet nozzles attached. Under the action of internal pressure, there exists a high stress concentration at the inner corner of the nozzle-

vessel intersection. Besides, due to the difficulty of welding, it is possible to produce initial flaws at the intersection. This makes the nozzle crotch corner region susceptible to damage through fatigue and subsequent failure through fracture. Hence, the fatigue and fracture of nozzle-corner cracks is one of the most important considerations in the assessment of integrity of pressure vessels.

There are two types of fracture that can be observed in a single crystal; brittle fracture and ductile fracture. A brittle fracture takes place without substantial plastic flow and occurs when the normal stress on one of the principal planes of the crystal reaches the critical value. When large plastic deformation occurs, consisting of sliding along crystallographic planes, prior to fracture, the failure is called a ductile fracture. These two types of fracture are also characteristic of polycrystalline materials. The brittle type exhibits little deformation and has a flat fracture surface essentially perpendicular to the direction of maximum stress; whereas, the ductile type exhibits gross deformation and the fracture surface has the familiar cup-and-cone form with shear-lips.

The thicker a component, the greater is the tendency for brittle, rather than ductile fracture to occur. Hence, linear elastic fracture mechanics (LEFM) theory can be used to assess the severity of cracks in thick pressure vessels, such as those employed in light water reactors (LWR). To ensure the structural integrity of a pressure vessel, it must be shown that sufficient safety margins exist between crack sizes which can be safely detected and those crack sizes which can lead to failure, under operational, as well as faulted conditions.

The crack characterizing parameter, stress intensity factor (SIF), proposed by Irwin in 1957, is used for this purpose within the framework of LEFM. The stress intensity factor is an important quantity in both fatigue and brittle fracture situations. In the former, the SIF range can be related to fatigue crack growth and in the latter, SIF can be compared with the material fracture toughness (critical stress intensity factor) to assess the likelihood of brittle fracture. Although the evaluation of SIF is fairly simple for cracks in the cylindrical part of the vessel, the situation is much more complicated for nozzle-corner cracks. Because of the complexity of the geometry, it is not possible to derive analytical solution. It can be estimated only by an approximate method. The approximate methods that have been used so far to estimate the value of SIF can be roughly categorized into the following three kinds:

- 1) Approximate analysis: Among these, Kobayashi's approximate analysis, Besuner's influence function method and Mohamed's approximate method are the most well known. However for all these methods, the stress distribution at the uncracked geometry must be known beforehand.
- 2) Experimental methods: These involve mainly the fatigue crack growth method, photo-elasticity method etc. The advantage of these methods is that their results are reliable as they involve the effect of all the factors on the SIF. But the shortcomings are the effort and cost in model making and testing.
- 3) Finite element method (FEM): The main advantage of this method is its general purpose nature and that it can be used to study the cracks of any shape under any kind of loading. Its results are relatively reliable. However it is costly in computation.

Since, none of these methods can fetch the value of SIF instantly, it is desirable to apply one or all of these, and compile SIF data for a number of nozzle-vessel geometries in a given range, and a number of crack shapes and sizes.

Besides the consideration of the normal operational load condition of the Reactor Pressure Vessel (constant internal pressure load), it is also important to consider the accidental conditions. Under normal circumstances, the temperature gradients in the nozzle-vessel intersection are such that they produce compression on the inner surface, and hence the thermal stresses do not cause any adverse effect on a nozzle-corner crack. Therefore, in the normal operational condition, it is sufficient to consider only the internal pressure load to study the behaviour of nozzle-corner cracks.

But in a special situation, commonly referred to as the "thermal shock" problem, which arises during a typical accidental condition due to a sudden loss of the Reactor coolant, the thermal stresses can prove fatal for a nozzle-corner crack. Thermal shock involves the possibility of fracture of a nuclear reactor pressure vessel during a loss of coolant accident (LOCA) under circumstances that are most likely to occur in a pressurized water reactor (PWR) plant. During a LOCA, cold water is splashed on the inner surface of the vessel by the emergency core cooling system (ECCS). This produces thermal stresses which can cause a nozzle-corner crack, which is otherwise safe, to become critical. For this reason, the thermal shock problem is of profound concern to the nuclear power industry.

## 1.2 Literature Review

Three dimensional finite element methods have primarily been employed to determine stress intensity factors for a crack at the crotch of a nozzle in a pressure vessel. The first SIF solution for such cracks was published by Rashid and Gilman [1], who based their finite element solution on strain energy release rate.

Shah and Kobayashi [2] gave the solution of an embedded elliptical crack exposed to arbitrary normal pressure.

Hellen and Dowling [3] gave the SIF solutions around the profiles of four crack configurations at the inner crotch of a typical LWR nozzle-vessel intersection. Three dimensional finite element techniques were used, incorporating quadratic isoparametric elements with special singularity elements around the crack profile. Direct substitution in the displacement field solution near the crack tip, and virtual crack extension techniques were used for the calculation of SIF.

Schmitt [4] used a numerical technique based on the Westergaard stress function to calculate the value of SIF at mid points of straight-front cracks of the nozzle of a vessel.

Schmitt [5] analysed a nozzle-corner crack by FEM using crack tip singularity elements and compared the SIF values along the crack front with the crack initiation fracture toughness ( $K_{Ic}$ ) and the crack arrest fracture toughness ( $K_{Ia}$ ) to demonstrate the structural integrity.

Broekhoven [6] used so-called semi-analytical procedure to find SIF for the cracks at the corner of a nozzle-plate intersection. The technique is a modification of the solution of an embedded elliptical crack by Shah and Kobayashi [2].

Bessuner et al. [7] employed the influence function (IF) method to calculate average SIF for cracks of various sizes and locations at the inside of a nozzle attached to a vessel. The method involves the use of an influence function which is independent of the loading but depends only on the crack shape, nozzle geometry and boundary conditions.

Kobayashi et al. [8] has obtained SIF values for nozzle-corner cracks by employing the results of a quarter-elliptical crack at a quarter space exposed to different loading conditions. These results were obtained using the so-called alternating technique.

Mohamed and Schroeder [9] used the existing solutions for corner cracks at the intersections of nozzles with plates or vessels to develop an empirical relationship for SIF of such

cracks. They also proposed a general method to predict SIF values of corner cracks using stress concentration for pressure loading only.

W. Schmitt et al. [10] gave the SIF solutions for two different nozzle geometries and different crack sizes for pressure and thermal loading using three dimensional elastic finite element models. They also proposed a procedure to estimate the maximum SIF for arbitrary crack size and loading conditions.

Guozhong and Qichao [11] simplified the iso-stress lines at a nozzle-corner into straight lines at an angle of  $45^\circ$  with the walls of the cylinder and nozzle, and based on this, derived an SIF solution for an arbitrary point on the crack front of a nozzle-corner crack by means of an approximate analysis. Following from this, they proposed approximate expressions for maximum and average SIF.

Baisong et al. [12] proposed an improved 3-D collapsed isoparametric singular element with quarter-points for crack analysis using FEM. They also analysed a corner crack in the interior wall of a nozzle of a Reactor pressure vessel using the proposed element, and calculated the SIF using the William's formula for displacement field near a stationary crack, as well as the least-squares linear fitting method.

The only known experimental results for nozzle-corner cracks are those of Derby [13], Broekhoven [14], Smith et al. [15] and Ruiz [16]. Derby [13] conducted burst tests on two groups of epoxy models of intersections of nozzles with vessels. The average SIF at burst was taken to be equal to the fracture toughness of the material. Smaller sizes of the models were also investigated experimentally by Smith et al. [15] using the frozen-stress photoelastic technique, which permits the evaluation of variations in SIF values along the crack fronts.

Broekhoven [14] correlated the propagation rates obtained for nozzle-corner cracks with those of standard specimens of the same material. He obtained minor variation of SIF values on the crack front.

Ruiz [16] also used the frozen-stress photoelastic technique to determine the average SIF for straight-front cracks at the corner of several models of tees (intersection of two cylinders).

Smith et al. [17] used a method which is a combination of frozen stress photoelasticity and a computerized least-squares data analysis for measuring SIF distributions at nozzle-corner cracks. The authors have emphasized on the importance of using actual flaw shapes in analysis.

### 1.3 Overview of the Present Work

The problem considered in the present work is given for study by the **Pressure Vessels Section** of the **Light Water Reactor Division (LWRD)** of **Bhabha Atomic Research Centre (B.A.R.C.)**, Mumbai. The problem is concerned with the assessment of structural integrity of a typical, thick, high pressure vessel having a nozzle-corner crack. Although, design codes, such as the ASME Boiler and Pressure Vessel code [18], describe methods to roughly estimate SIF for cracks in pressure vessels, they are often over conservative and do not reveal the true picture; and experiments, as stated previously, are costly and more time consuming. In lieu of the above, numerical methods like FEM offer a viable and reliable solution.

The present work can be subdivided in to three main parts, as detailed below, along with a brief description of each part:

- I. Calculation of Stress Intensity Factors for nozzle-corner cracks under normal operational load condition:
  - 1) Stress analysis of the uncracked nozzle-vessel intersection and its validation.
  - 2) Stress analysis of the intersection with corner crack.
  - 3) Evaluation of SIF along the crack front using the results of stress analysis, and its validation.
  - 4) Parametric study of SIF of nozzle-corner cracks for different geometrical and crack parameters.
  
- II. Study of the behaviour of a given nozzle-corner crack during a LOCA:
  - 1) Transient thermal-stress analysis of nozzle-vessel intersection with corner crack.
  - 2) Evaluation of SIF along the crack front at different time points.
  - 3) Plotting of SIF at different points of the crack front as functions of time and their comparison with material fracture toughness for crack initiation.



### III. Prediction of the amount of stable crack growth using cohesive-zone method:

- 1) Incorporation of the special cohesive elements in to the Finite Element (FE) model and inclusion of the corresponding FE equations in to the general purpose FE code ABAQUS, through a user subroutine written in FORTRAN.

## 1.4 Organization of the Thesis

The thesis consists of seven chapters in all. The organization of the thesis is as follows:

- 1) Chapter 2 gives the FE formulations of 3D stress and heat transfer analyses.
- 2) Chapter 3 presents the results and validation of stress analysis of nozzle-vessel intersection without crack.
- 3) Chapter 4 deals with the effect of the normal operational load on nozzle-corner cracks. The Chapter presents the results of stress analysis of the nozzle-vessel intersection with a corner crack. The SIF is then evaluated for the corner cracks using the method described in the Chapter and the results are verified. This is followed by the parametric study of SIF.
- 4) Chapter 5 is dedicated to the study of effect of a LOCA on a nozzle-corner crack.
- 5) Chapter 6 gives the formulation of a 3D cohesive zone element and presents the results of crack growth analysis.
- 6) Chapter 7 concludes the work and suggests the scope for future work.

## Chapter 2

# FE FORMULATIONS FOR STRESS AND HEAT TRANSFER ANALYSES

### 2.1 Introduction

The study of a physical phenomenon usually involves two major tasks: Mathematical modeling of the physical process resulting in algebraic, differential or integral equations and solution of the resulting equation.

While the derivation of the governing equations for most problems is not unduly difficult, their solution by exact methods of analysis is a difficult task. In such cases, approximate methods of analysis provide alternative means of finding solutions.

The Finite Element (FE) method is one of the most popular methods of numerical analysis, in which, a given domain is represented as a collection of simple sub-domains, called finite elements, so that, it is possible to systematically construct the approximation functions over each element, needed in a variational or weighted-residual approximation of the solution of a problem.

In this chapter, the FE formulations for a 3D static stress analysis, and a 3D transient heat transfer analysis have been presented.

### 2.2 FE Formulation for 3D Static Stress Analysis

Consider an arbitrary three-dimensional solid body  $\Omega$  with volume  $V$  and boundary  $\Gamma$  as shown in Figure 2.1.

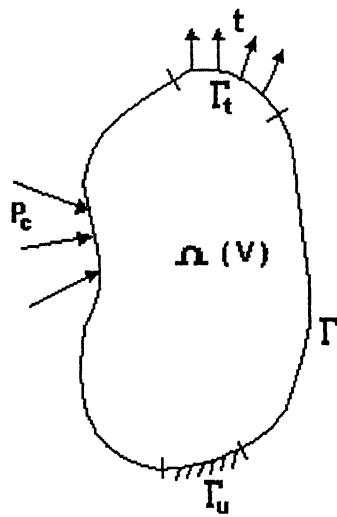


**Figure 2.1 Domain and Boundary Conditions for Stress Analysis.**

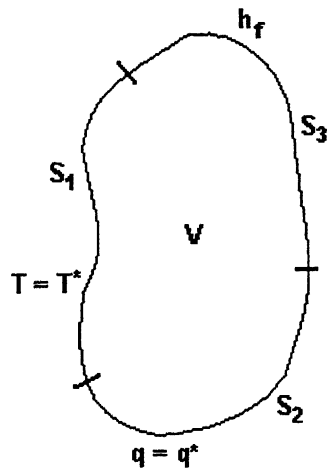


**Figure 2.2 Domain and Boundary Conditions for Heat Transfer Analysis.**

With reference to the Figure,  $\Gamma_u$  represents the boundary on which displacement is specified. Traction  $\mathbf{t}$  is specified on the boundary  $\Gamma_t$  and  $\mathbf{P}_c$  represents the concentrated forces acting on the body.

The principle of virtual work states that for a virtual perturbation in the displacement field at equilibrium, the virtual change in the internal strain energy ( $\delta U$ ) must be balanced by an identical change in the external work ( $\delta W$ ) due to the applied loads, that is:

$$\delta U = \delta W, \quad (2.1)$$

$$\text{or,} \quad \sum_e \delta U_e = \sum_e \delta W_e, \quad (2.2)$$

where,  $\delta U_e$  and  $\delta W_e$  are the contributions of the finite element  $e$  to the virtual change in strain energy and external work respectively.

Now,

$$\delta U_e = \int_{V_e} \{\delta \varepsilon\}^T \{\sigma\} dV_e, \quad (2.3)$$

where,

$V_e$  represents the volume of the element  $e$ ,

$$\{\varepsilon\} = \text{Strain vector} = [\varepsilon_x \quad \varepsilon_y \quad \varepsilon_z \quad \varepsilon_{xy} \quad \varepsilon_{yz} \quad \varepsilon_{xz}]^T,$$

$$\{\sigma\} = \text{Stress vector} = [\sigma_x \quad \sigma_y \quad \sigma_z \quad \sigma_{xy} \quad \sigma_{yz} \quad \sigma_{xz}]^T.$$

Assuming an isotropic linear elastic material behaviour, Equation 2.3 may be expanded as:

$$\delta U_e = \int_{V_e} (\{\delta \varepsilon\}^T [D] \{\varepsilon\} - \{\delta \varepsilon\}^T [D] \{\varepsilon_{th}\}) dV_e, \quad (2.4)$$

where,

$[D]$  is the material property matrix given by:

$$[D] = \frac{E}{(1+\nu)(1-2\nu)} \begin{bmatrix} 1 & \nu & \nu & 0 & 0 & 0 \\ \nu & 1 & \nu & 0 & 0 & 0 \\ \nu & \nu & 1 & 0 & 0 & 0 \\ 0 & 0 & 0 & \frac{1-2\nu}{2} & 0 & 0 \\ 0 & 0 & 0 & 0 & \frac{1-2\nu}{2} & 0 \\ 0 & 0 & 0 & 0 & 0 & \frac{1-2\nu}{2} \end{bmatrix},$$

where,  $E$  is the Young's modulus of the material and  $\nu$  is the Poisson's ratio;

and  $\{\varepsilon_{th}\} = \text{Thermal strain vector} = \Delta T [\alpha \quad \alpha \quad \alpha \quad 0 \quad 0 \quad 0]^T$ , (2.5)

where,  $\Delta T = T - T_{ref}$ ,

$\alpha = \text{Coefficient of thermal expansion of the material,}$

where,  $T = \text{Current temperature at the point in question,}$

$T_{ref} = \text{Reference (strain-free) temperature.}$

The strains are related to the displacements as:

$$\{\varepsilon\} = \left[ \frac{\partial u}{\partial x} \quad \frac{\partial v}{\partial y} \quad \frac{\partial w}{\partial z} \quad \left( \frac{\partial u}{\partial y} + \frac{\partial v}{\partial x} \right) \quad \left( \frac{\partial v}{\partial z} + \frac{\partial w}{\partial y} \right) \quad \left( \frac{\partial u}{\partial z} + \frac{\partial w}{\partial x} \right) \right]^T, \quad (2.6)$$

where,  $u$ ,  $v$  and  $w$  represent the displacements of any arbitrary point within the element, in  $x$ ,  $y$  and  $z$  directions respectively, and are interpolated from the nodal displacements through the element shape functions as:

$$\begin{Bmatrix} u \\ v \\ w \end{Bmatrix} = [N] \{u_e\}, \quad (2.7)$$

where,  $[N]$  is the element shape function matrix and  $\{u_e\}$  is the element nodal displacement vector.

From Equations 2.6 and 2.7,

$$\{\varepsilon\} = [B]\{u_e\}, \quad (2.8)$$

where,  $[B]$  is the strain-displacement matrix based on the derivatives of the element shape functions.

Combining Equations 2.4 and 2.8, and noting that  $\{u_e\}$  does not vary over the volume of the element:

$$\delta U_e = \{\delta u_e\}^T \int_{V_e} [B]^T [D] [B] dV_e \{u_e\} - \{\delta u_e\}^T \int_{V_e} [B]^T [D] \{\varepsilon_{th}\} dV_e. \quad (2.9)$$

Now,

$$\delta W_e = \{\delta u_e\}^T \int_{\Gamma_t^e} [N]^T \{t^e\} d\Gamma_t^e + \{\delta u_e\}^T \{P_c^e\}, \quad (2.10)$$

where,

$\Gamma_t^e$  is the area of the element that falls on  $\Gamma_t$ ,

$\{t^e\}$  = Traction vector on  $\Gamma_t^e = [t_x^e \quad t_y^e \quad t_z^e]^T$ ,

$\{P_c^e\}$  = Concentrated nodal force vector.

Finally, substituting Equations 2.9 and 2.10 into Equation 2.2 and writing the Equation on element basis to give:

$$\sum_e \left( \{\delta u_e\}^T \int_{V_e} [B]^T [D] [B] dV_e \{u_e\} - \{\delta u_e\}^T \int_{V_e} [B]^T [D] \{\varepsilon_{th}\} dV_e \right) = \sum_e \left( \{\delta u_e\}^T \int_{\Gamma_t^e} [N]^T \{t^e\} d\Gamma_t^e + \{\delta u_e\}^T \{P_c^e\} \right) \quad (2.11)$$

Now, since  $\{\delta u_e\}^t$  is arbitrary, Equation 2.11 reduces to:

$$\sum_e [K_e] \{u_e\} = \sum_e \{F_e'\} + \sum_e \{P_e^e\} + \sum_e \{F_e^{th}\}, \quad (2.12)$$

where,

$$[K_e] = \int_{V_e} [B]^T [D] [B] dV_e = \text{Element stiffness matrix},$$

$$\{F_e'\} = \int_{\Gamma_e^e} [N]^T \{t^e\} d\Gamma_e^e = \text{Element traction load vector},$$

$$\{F_e^{th}\} = \int_{V_e} [B]^T [D] \{\varepsilon_{th}\} dV_e = \text{Element thermal load vector}.$$

The element matrices and load vectors of all the elements in the domain are assembled together to get the global stiffness matrix  $[K]$  and the global load vector  $\{F\}$  such that:

$$[K] \{u_g\} = \{F\},$$

where,  $\{u_g\}$  is the global nodal displacement vector.

## 2.3 FE Formulation for 3D Transient Heat Transfer Analysis

The governing differential equation for transient 3D heat transfer in a solid is:

$$\rho C \frac{\partial T}{\partial t} + \{L\}^T \{q\} = \ddot{q}, \quad (2.13)$$

where,

$\rho$  = Density of the material,

$C$  = Specific heat of the material,

$T = T(x, y, z, t)$  = Temperature,

$t$  = Time,

$$\{L\} = \begin{Bmatrix} \frac{\partial}{\partial x} \\ \frac{\partial}{\partial y} \\ \frac{\partial}{\partial z} \end{Bmatrix} = \text{Vector operator},$$

$\{q\}$  = Heat flux vector,

$\ddot{q}$  = Heat generation rate per unit volume.

Fourier's heat conduction law yields:

$$\{q\} = -[D]\{L\}T, \quad (2.14)$$

where,

$$[D] = \begin{bmatrix} k_x & 0 & 0 \\ 0 & k_y & 0 \\ 0 & 0 & k_z \end{bmatrix} = \text{Conductivity matrix},$$

where,  $k_x$ ,  $k_y$  and  $k_z$  are thermal conductivities in  $x$ ,  $y$  and  $z$  directions respectively.

Combining Equations 2.13 and 2.14,

$$\rho C \frac{\partial T}{\partial t} = \{L\}^T ([D]\{L\}T) + \ddot{q}. \quad (2.15)$$

Three types of boundary conditions are considered (with reference to Figure 2.2):

1) Specified temperatures over surface  $S_1$ :

$$T = T^*, \quad (2.16)$$

where,  $T^*$  is the specified temperature.



2) Specified heat flux over surface  $S_2$ :

$$\{q\}^T \{n\} = -q^*, \quad (2.17)$$

where,  $\{n\}$  is the unit outward vector normal to the surface and  $q^*$  is the specified heat flux.

3) Specified convection over surface  $S_3$ :

$$\{q\}^T \{n\} = -h_f(T_B - T_S), \quad (2.18)$$

where,  $h_f$  is the convective film coefficient,  $T_B$  is the bulk temperature of the adjacent medium and  $T_S$  is the surface temperature.

Combining Equations 2.14 with Equations 2.17 and 2.18,

$$\{n\}^T [D] \{L\} T = q^*, \quad \text{on } S_2, \quad (2.19)$$

$$\{n\}^T [D] \{L\} T = h_f(T_B - T), \quad \text{on } S_3. \quad (2.20)$$

Pre-multiplying Equation 2.15 by a virtual change in temperature, integrating over the volume ( $V_e$ ) of the element e, and combining with Equations 2.19 and 2.20, with some manipulation yields the variational statement:

$$\int_{V_e} \left( \rho C \delta T \frac{\partial T}{\partial t} + \{L\}^T (\delta T) ([D] \{L\} T) \right) dV_e = \int_{S_2} \delta T q^* dS_2 + \int_{S_3} \delta T h_f (T_B - T) dS_3 + \int_{V_e} \delta T \ddot{q} dV_e, \quad (2.21)$$

where,

$$\delta T = \delta T(x, y, z, t) = \text{Virtual change in temperature.}$$

Now, the dependencies of  $T$  on space and time are separated as:

$$T = \{N\}^T \{T_e\}, \quad (2.22)$$

where,

$\{N\} = \{N(x, y, z)\}$  = Element shape function vector,

$\{T_e\} = \{T_e(t)\}$  = Element nodal temperature vector.

Thus,

$$\frac{\partial T}{\partial t} = \dot{T} = \{N\}^T \{\dot{T}_e\}, \quad (2.23)$$

$$\delta T = \{\delta T_e\}^T \{N\}, \quad (2.24)$$

$$\{L\}T = [B]\{T_e\}, \quad (2.25)$$

where,

$$[B] = \{L\}\{N\}^T.$$

Now, Equation 2.21 can be combined with Equations 2.22 - 2.25 to yield:

$$\begin{aligned} \sum_e \left( \int_{V_e} \rho C \{\delta T_e\}^T \{N\} \{N\}^T \{\dot{T}_e\} dV_e + \int_{V_e} \{\delta T_e\}^T [B]^T [D] [B] \{T_e\} dV_e \right) = \sum_e \left( \int_{S_2} \{\delta T_e\}^T \{N\} q^* dS_2 \right. \\ \left. + \int_{S_3} \{\delta T_e\}^T \{N\} h_f (T_B - \{N\}^T \{T_e\}) dS_3 + \int_{V_e} \{\delta T_e\}^T \{N\} \ddot{q} dV_e \right). \end{aligned} \quad (2.26)$$

$\rho$  is assumed to be constant over the volume of the element, while  $C$  and  $\ddot{q}$  may vary over the element. Now, since  $\{\delta T_e\}$  is arbitrary, Equation 2.26 reduces to:

$$\sum_e \left( [C_e] \{\dot{T}_e\} + ([K_e^d] + [K_e^c]) \{T_e\} \right) = \sum_e \left( \{Q_e^f\} + \{Q_e^c\} + \{Q_e^g\} \right), \quad (2.27)$$

where,  $[C_e] = \rho \int_{V_e} C \{N\} \{N\}^T dV_e$  = Element specific heat (thermal damping) matrix,

$$[K_e^d] = \int_{V_e} [B]^T [D] [B] dV_e = \text{Element diffusion conductivity matrix},$$

$$[K_e^c] = \int_{S_3} h_f \{N\} \{N\}^T dS_3 = \text{Element convection surface conductivity matrix},$$

$$\{Q_e^f\} = \int_{S_2} \{N\} q^* dS_2 = \text{Element heat flux vector},$$

$$\{Q_e^c\} = \int_{S_3} T_b h_f \{N\} dS_3 = \text{Element convection surface heat flow vector},$$

$$\{Q_e^g\} = \int_{V_e} \ddot{q} \{N\} dV_e = \text{Element heat generation load vector}.$$

The element matrices and load vectors are assembled together for all the elements in the domain to get the global thermal damping matrix ( $[C]$ ), the global conductivity matrix ( $[K]$ ) and the global load vector ( $\{Q\}$ ) such that:

$$[C]\{\dot{T}_g\} + [K]\{T_g\} = \{Q\},$$

where,  $\{T_g\}$  is the global nodal temperature vector.

## 2.4 Closure

The Finite Element formulations for three-dimensional static stress analysis and transient heat transfer analysis have been presented. In the present work, static stress analysis of the nozzle-vessel intersection has been performed for the normal operational load condition; and a sequential transient thermal-stress analysis has been performed for the faulted condition (LOCA).

## Chapter 3

# STRESS ANALYSIS OF UNCRACKED NOZZLE-VESSEL INTERSECTION

### 3.1 Introduction

The aim of this chapter is to identify the partial section of the structure in the vicinity of the nozzle-vessel junction, which is suitable and sufficient for the purpose of stress analysis, and also to validate the overall procedure adopted for the stress analysis. The normal operational load condition (simple internal pressure load) has been chosen for the purpose. Stress analysis of a partial section of the structure (without crack) has been performed and the methodology has been validated by comparison with the work of Moini and Mitchell [19].

### 3.2 Geometry

The basic geometry of the nozzle-vessel intersection considered in the present work, as given by the **Pressure Vessels Section** of LWRD, B.A.R.C., is described below:

Figure 3.1 shows the nozzle-vessel intersection, sectioned by the plane which contains the axes of both, the vessel and the nozzle. The main dimensions characterizing the intersection are also shown in the figure.

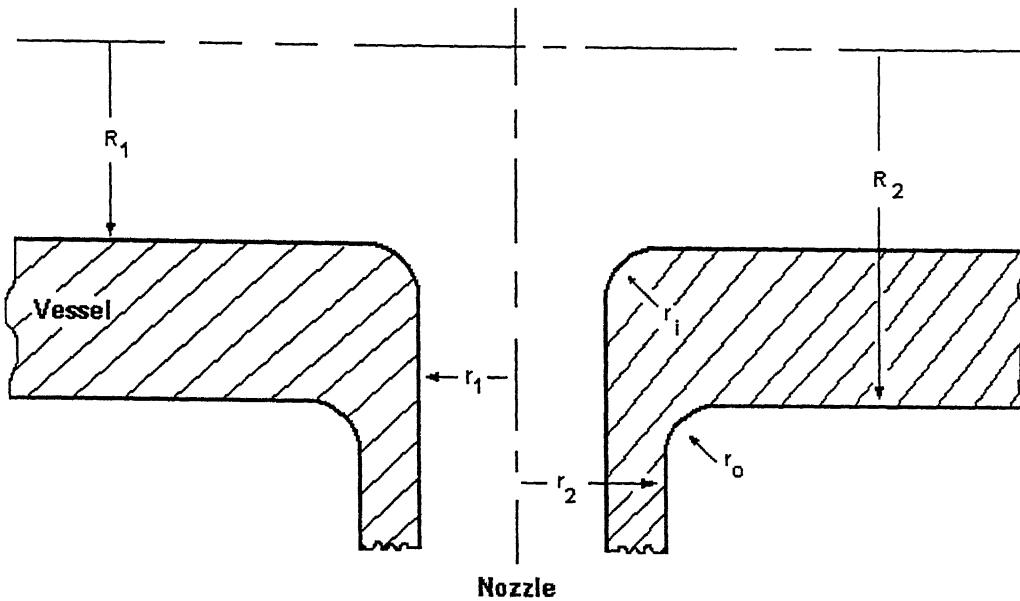


Figure 3.1 Geometry of the nozzle-vessel intersection.

These dimensions are given as:

- 1) Inner radius of the vessel,  $R_1 = 700$  mm.
- 2) Outer radius of the vessel,  $R_2 = 1000$  mm.
- 3) Inner radius of the nozzle,  $r_1 = 107$  mm.
- 4) Outer radius of the nozzle,  $r_2 = 165$  mm.
- 5) Radius of curvature of the inner fillet,  $r_i = 50$  mm.
- 6) Radius of curvature of the outer fillet,  $r_o = 100$  mm.

### 3.3 Material

Nuclear grade low alloy ferritic steels are commonly used for the fabrication of nuclear reactor pressure vessels. The material considered in the present work is the ASME SA 508-Class 3 pressure vessel steel. The chemical composition of the steel [20] is given in Table 3.1.

Element	Wt. %	Element	Wt. %
Carbon	0.18	Silicon	0.03
Manganese	1.48	Phosphorus	0.004
Sulphur	0.003	Nickel	0.91
Chromium	0.21	Molybdenum	0.54
Aluminium	0.003	Copper	0.045
Vanadium	0.003	Cobalt	0.004

**Table 3.1 Chemical composition of SA 508-Class 3 steel.**

The relevant mechanical and thermal properties of the material have been taken from Sattari-Far [21], where, the material properties for SA 533 B steel is given, which is similar to SA 508-Class 3 steel. The properties are listed in Table 3.2 for different temperatures.

Temp. (°C)	Thermal Conduc. (W/m°C)	Specific Heat (J/Kg°C)	Coeff. of thermal exp. (10 <sup>-6</sup> /°C)	Young's Mod. (GPa)	Yield Str. (MPa)
20	37.8	449	11.6	212	425
60	38.3	468	11.8	208	415
100	38.8	488	12.1	205	----
200	38.6	526	13.3	200	----
300	37.5	566	13.8	195	370

**Table 3.2 Material Properties for SA 508-Class 3 steel.**

### 3.4 Solid Modeling and FE Analysis

The general purpose Finite Element code, ANSYS 5.4, has been used to perform the stress analysis of the structure. At first, a nozzle-vessel junction with the given geometry has been modeled, without fillets, and stress analysis has been performed without the presence of crack, under a pressure loading and taking linear elastic material behaviour. The corresponding solid model generated in ANSYS is shown in Figure 3.2.

Since the structure is symmetrical about the plane containing the axes of both the cylinders (plane 1, as shown in Figure 3.2), and also about the plane containing the axis of the nozzle and perpendicular to the axis of the vessel (plane 3), it is sufficient to model a quarter section of the nozzle. Also, for simplicity, only a quarter section of the vessel has been modeled. This is valid under the assumption, that any radial plane of a cylinder far away from local geometrical discontinuities will have displacement only in the radial direction.

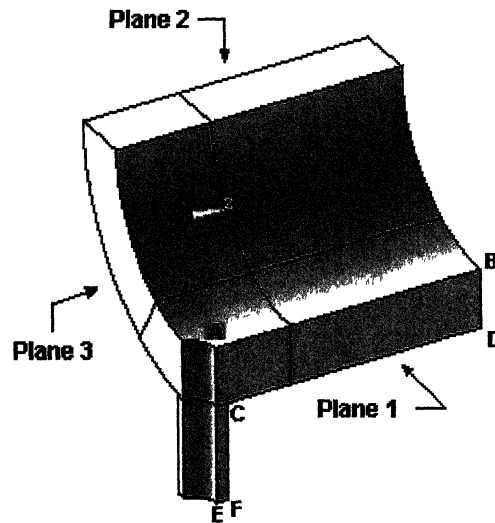


**Figure 3.2 Solid model of nozzle-vessel intersection.**

To decide upon the optimum lengths of the nozzle and the vessel that should be taken for analysis, a number of different models with different nozzle and vessel lengths are analyzed, and, hoop and longitudinal stresses are plotted along the lengths for both the cylinders. The criterion for the optimum lengths is that, the above stress plots should reach the corresponding values as obtained from the Lamé's thick cylinder formulae. This is to ensure that the longitudinal boundaries are sufficiently far away from the junction, so that, they are not affected by the local discontinuity stresses, and uniform longitudinal tractions can be applied on them as boundary conditions.

Based on the above, it has been found that 1.5 m vessel length (on one side of the junction) and 0.5 m nozzle length are sufficient to meet the above criterion. The corresponding FE model is shown in Figure 3.3.

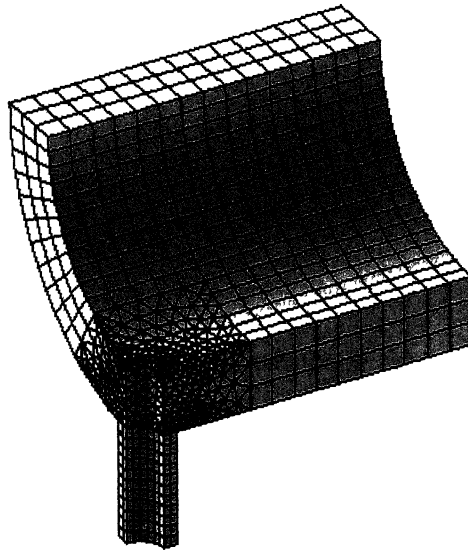


**Figure 3.3 FE Discretization of the model.**

The model has been discretized using a combination of 20-noded brick elements and 10-noded tetrahedral elements, with 13-noded pyramid transition elements in between. The model consists of 807 hexahedral elements and 2337 tetrahedral and transition elements, i.e., a total of 3144 elements, and 8251 nodes. The value of Young's modulus ( $E$ ) used is 210 GPa, and that of Poisson's ratio ( $\nu$ ) is 0.3.

### **3.4.1 Load and Boundary Conditions**

The load and boundary conditions applied to the discretized model (with reference to Figure 3.2) are as follows:



- a) With reference to Figure 3.2, Planes 1 and 3 are restricted to move in the respective normal directions, since both of them are planes of symmetry.
- b) Uniform internal pressure of magnitude 15 MPa is applied on the inner surfaces of both the cylinders.
- c) Plane 2 is restricted to move in the normal direction, since it is a radial plane to a cylinder loaded by internal pressure, and therefore cannot move tangentially.
- d) Longitudinal stresses are applied at the ends of both the cylinders, as calculated from the following relation:

$$\sigma = \frac{PR_i^2}{R_o^2 - R_i^2}, \quad (3.1)$$

where,  $R_i$  and  $R_o$  represent the inner and outer radii of the cylinders, and  $P$  is the internal pressure. This boundary condition is based on the assumption that the ends of both the cylinders are effectively capped by rigid closures.

### 3.5 Results and Discussion

The results of stress analysis are presented in the form of plots in Figures 3.4-3.7. In these figures, hoop and longitudinal stresses for the cylinders as calculated on the plane 1 are plotted along the lengths of the respective cylinders. Figure 3.4 shows the variation of stresses on plane 1 in the hoop and longitudinal directions to the vessel, along the edge which corresponds to the inner radius of the vessel (Path A-B). Figure 3.5 shows the variation of the stresses along the edge which corresponds to the outer radius of the vessel (Path C-D). Similarly, Figures 3.6 and 3.7 show the variation of the stresses on plane 1 in the hoop and longitudinal directions to the nozzle, along the edges corresponding to the inner (Path A-E) and outer (Path C-F) radii of the nozzle respectively.

As clearly seen from Figures 3.4-3.7, all the stresses become constant towards the end, as expected. The values to which these stresses approach are compared to the corresponding values calculated from the Lamé's thick cylinder formulae, and are found to match well within 2%. Thus, the validity of the boundary conditions is established.

To gain further confidence in the results of the stress analysis, the nozzle-vessel geometry analyzed by Moini and Mitchell [19], has been analyzed on the same lines as used in the analysis of the geometry of interest in the present work, and the results are compared with those of Moini and Mitchell [19]. The dimensions of geometry analyzed, load applied and properties used by Moini and Mitchell [19] are:  $R_1 = 5$  in,  $R_2 = 5.5$  in,  $r_1 = 2.5$  in,  $r_1 = 2.75$  in,  $r_i = r_o = 0.25$  in. Internal Pressure  $P = 100$  psi,  $E = 30 \times 10^6$  psi,  $\nu = 0.3$ .

The results of the present analysis are found to match satisfactorily well with the results of Moini and Mitchell [19], as shown in Figures 3.8-3.15.

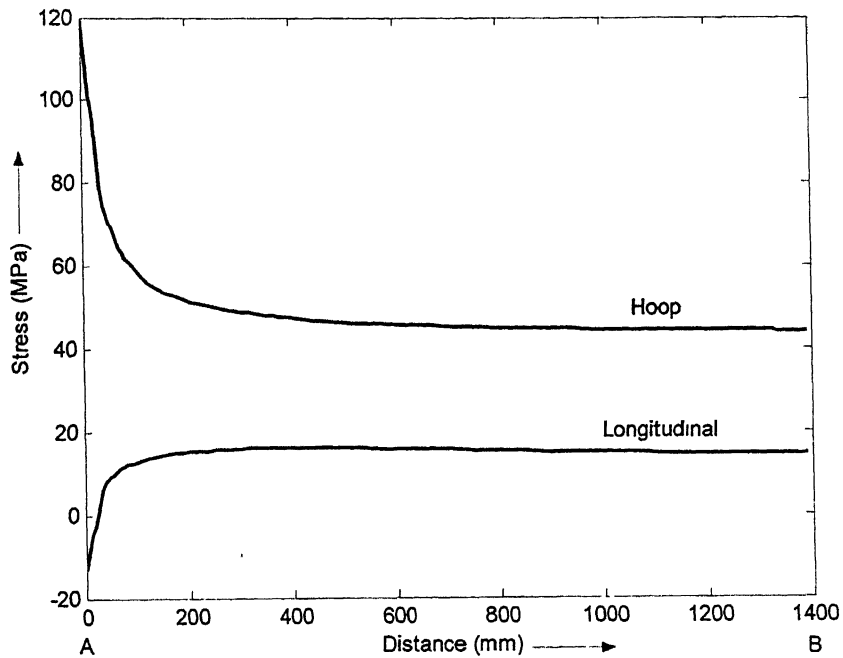


Figure 3.4 Stresses on the inside of the vessel (Path A-B).

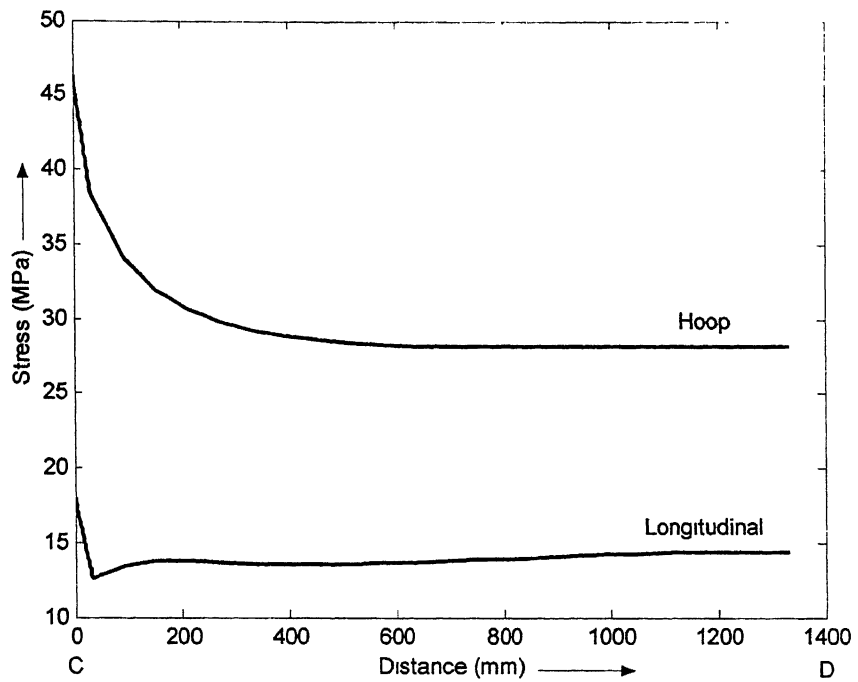


Figure 3.5 Stresses on the outside of the vessel (Path C-D).

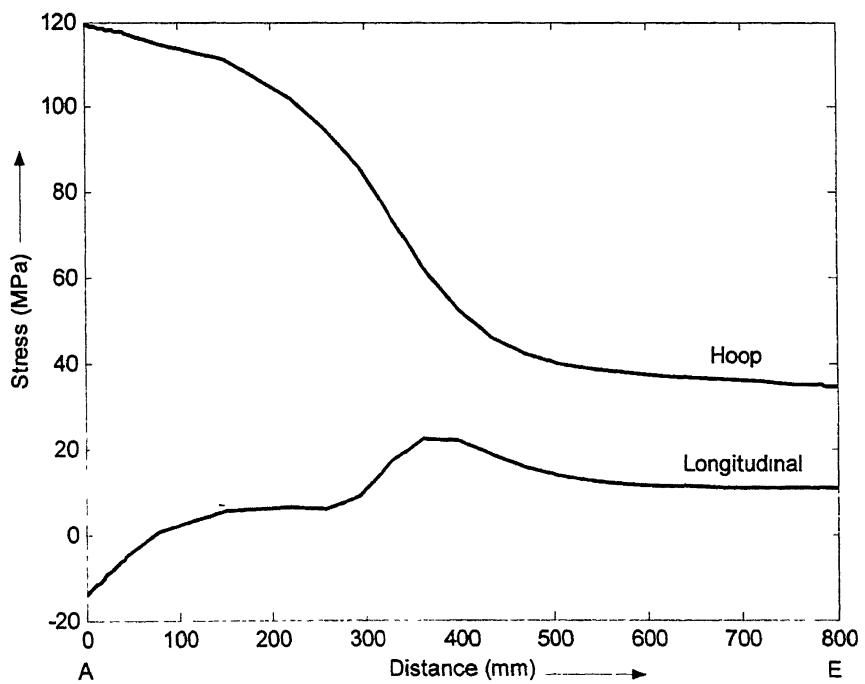


Figure 3.6 Stresses on the inside of the nozzle (Path A-E).

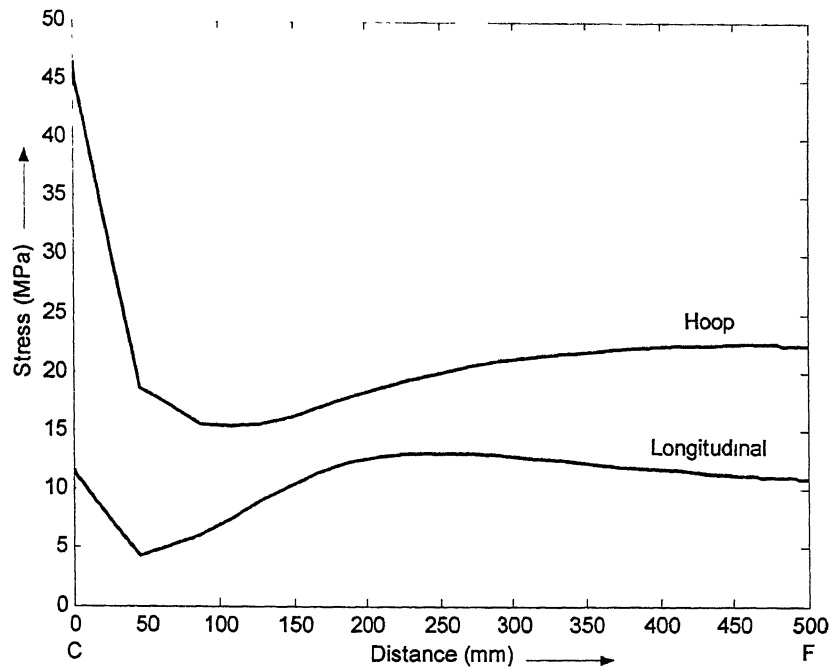


Figure 3.7 Stresses on the outside of the nozzle (Path C-F).

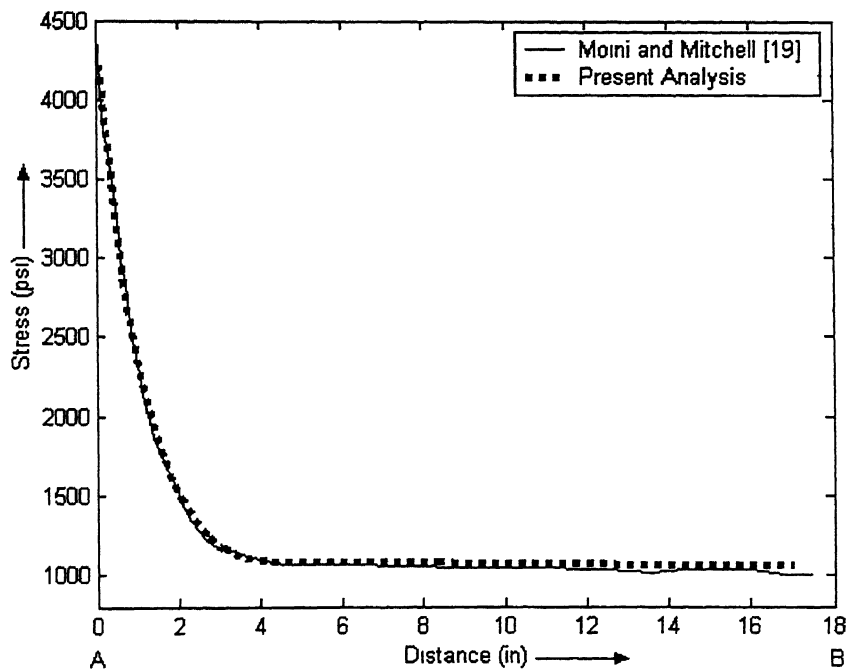


Figure 3.8 Hoop stress on the inside of the vessel (Path A-B).

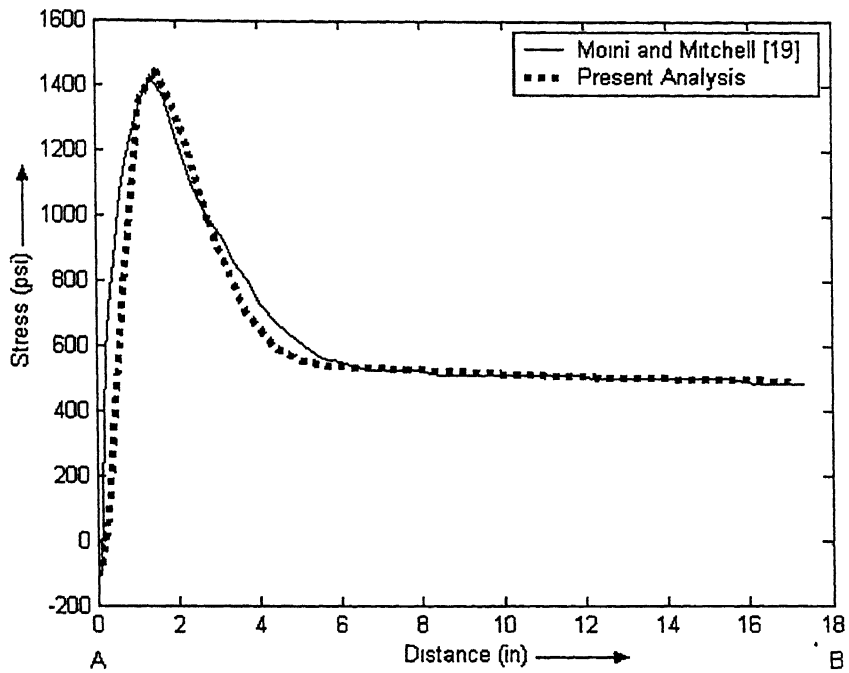


Figure 3.9 Longitudinal stress on the inside of the vessel (Path A-B).

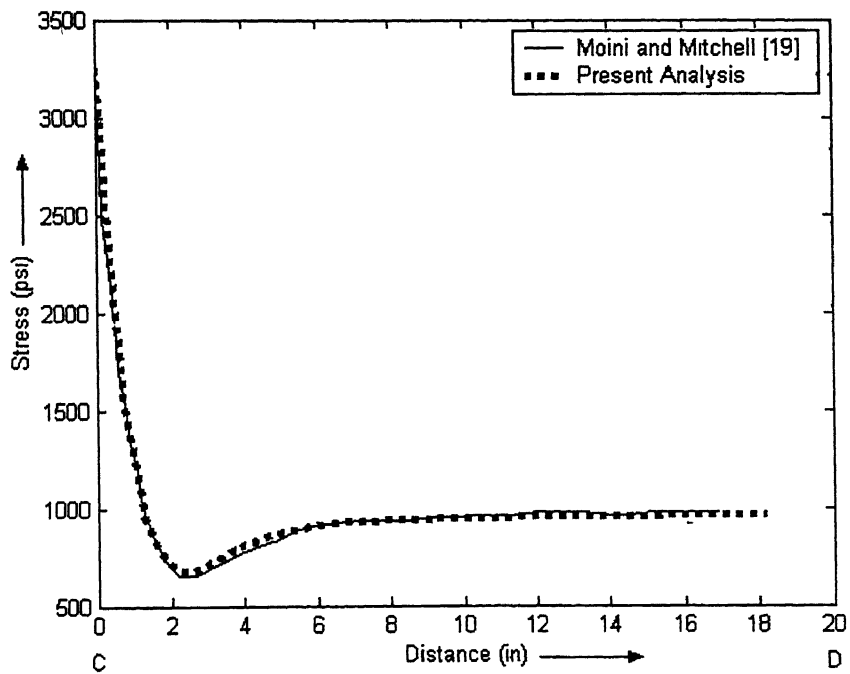


Figure 3.10 Hoop stress on the outside of the vessel (Path C-D).

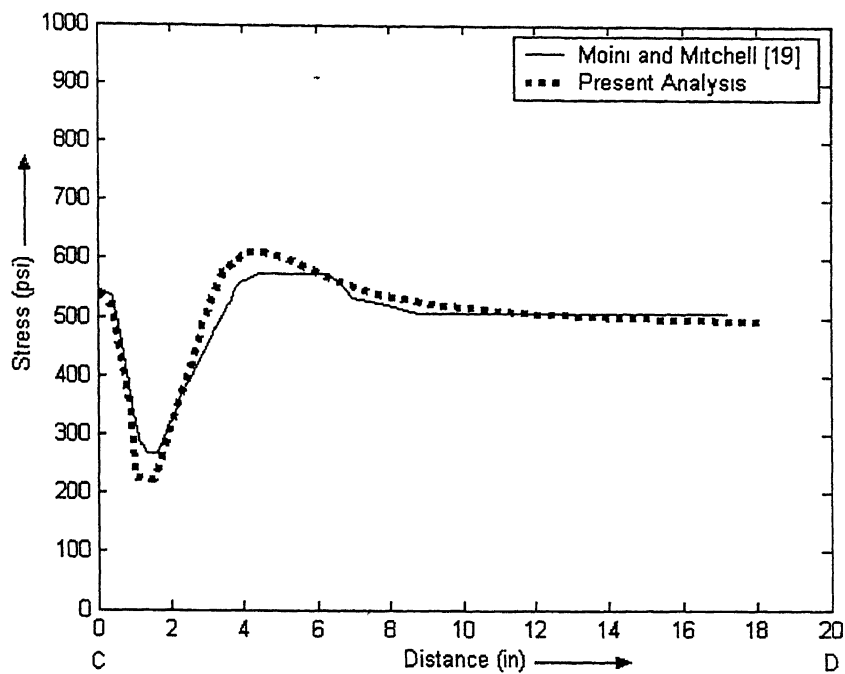


Figure 3.11 Longitudinal stress on the outside of the vessel (Path C-D).

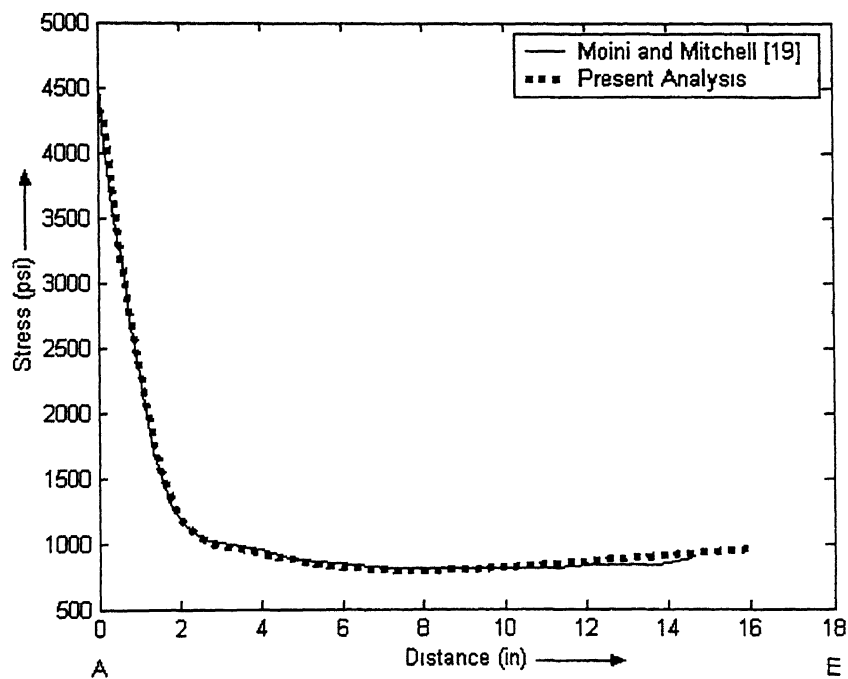


Figure 3.12 Hoop stress on the inside of the nozzle (Path A-E).

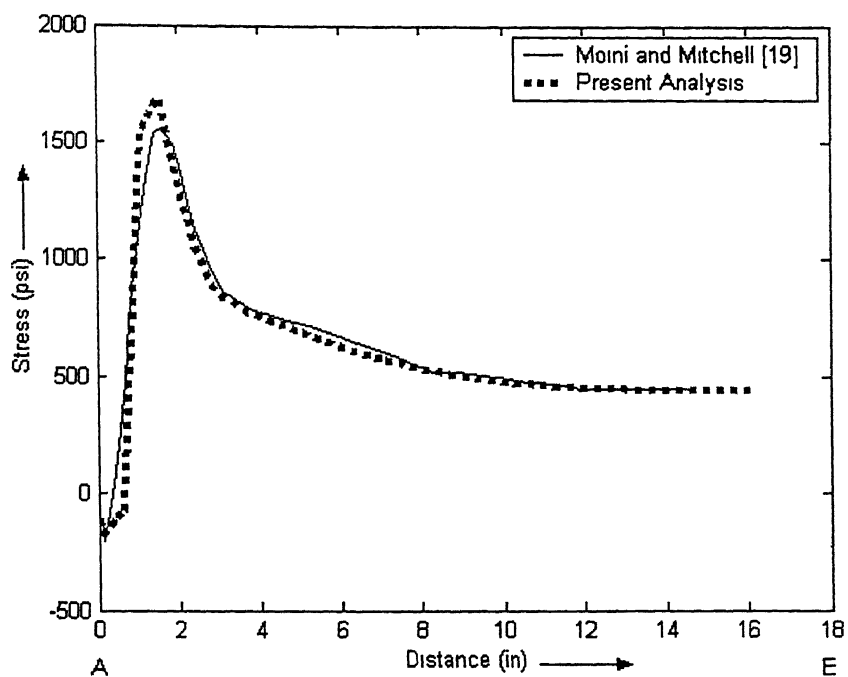


Figure 3.13 Longitudinal stress on the inside of the nozzle (Path A-E).

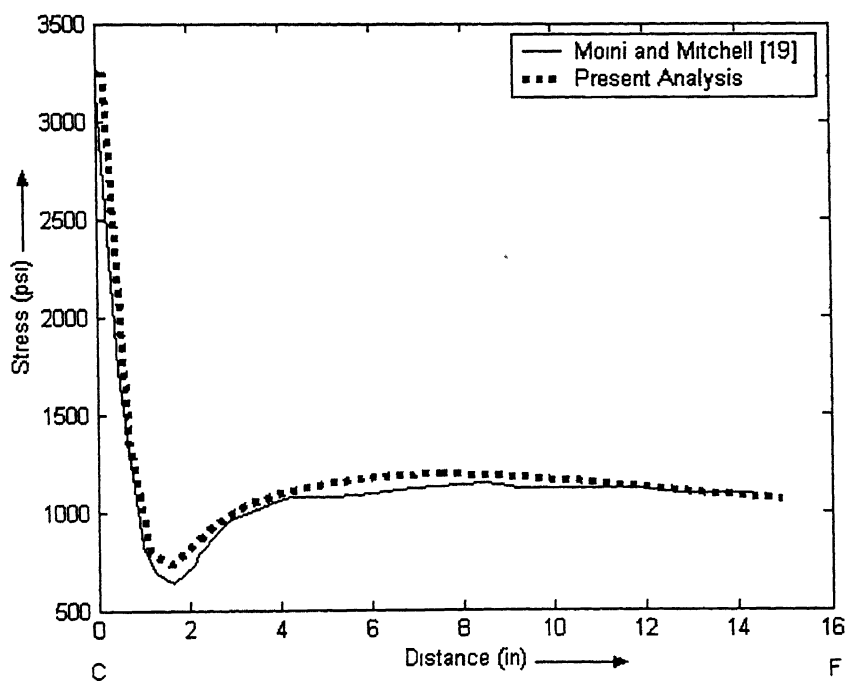


Figure 3.14 Hoop stress on the outside of the nozzle (Path C-F).

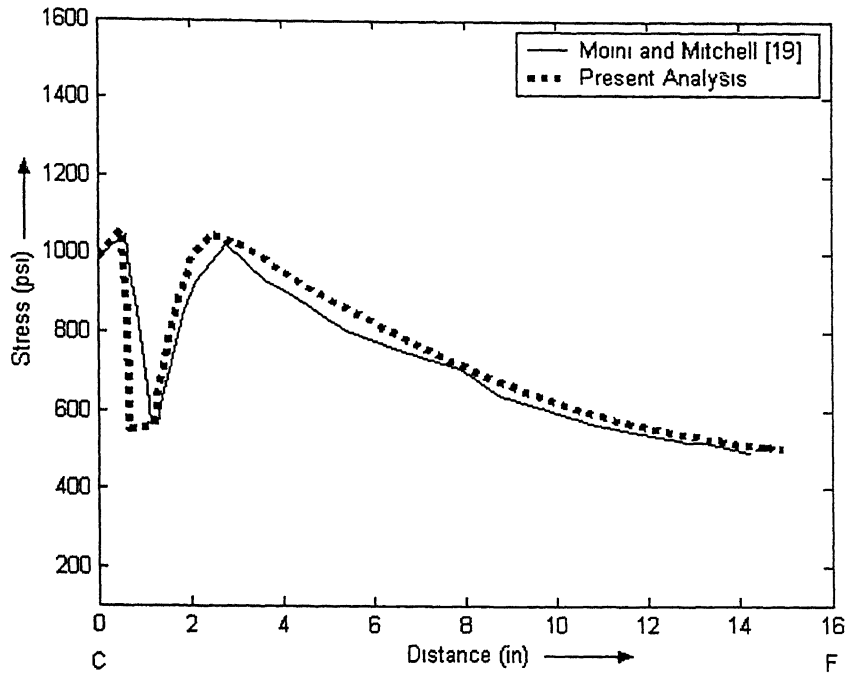


Figure 3.15 Longitudinal stress on the outside of the nozzle (Path C-F).

### 3.6 Closure

The results of stress analysis of the nozzle-vessel intersection without crack have been presented. By the comparison of the present analysis with the work of Moini and Mitchell [19], it is concluded that, the partial modeling of the nozzle-vessel geometry in a judicious manner gives reasonably satisfactory results while keeping the computational effort minimum.



## **Chapter 4**

# **EFFECT OF NORMAL OPERATIONAL LOAD ON NOZZLE-CORNER CRACKS**

### **4.1 Introduction**

As introduced in section 1.1, a high stress concentration exists at the crotch region of a nozzle-vessel intersection. Moreover, because of the welded joint at the intersection, there always exists a possibility of initial flaw. Due to the high stresses, an existing flaw may grow up in to a surface crack through fatigue. Such cracks are called nozzle-corner cracks. Though the actual shapes of such cracks are not simple, it has been observed that nozzle-corner cracks grown by fatigue are usually almost quarter-circular or quarter-elliptical in shape. Hence, for the purpose of numerical analysis, such cracks can be approximated by quarter-circular or quarter-elliptical profiles. In this chapter, the effect of the normal operational load (constant internal pressure) on nozzle-corner cracks has been studied.

### **4.2 Crack Configuration**

Since the present work is a safety assessment, the most crucial crack orientation has been studied. The face of the corner crack has been assumed to be located in the plane which contains the axes of both the cylinders (vessel and nozzle), so that, the hoop stresses of the vessel and the nozzle

cause the crack to be loaded in mode I (crack opening mode, i.e. load normal to the crack surface). Figure 4.1 defines the dimensional parameters used to characterize the crack.

With reference to the Figure, the centre,  $O$ , of the quarter ellipse, is characterized by  $r_1$ , the inner radius of the nozzle, and  $R_1$ , the inner radius of the vessel. The crack depth  $a$ , along the nozzle wall, characterizes the semi-major axis of the quarter-ellipse, and similarly, the crack width  $b$ , along the vessel wall, marks the semi-minor axis of the quarter-ellipse. The same definition holds good when the inner fillet is also modeled, in which case, point  $o$  does not physically exist.

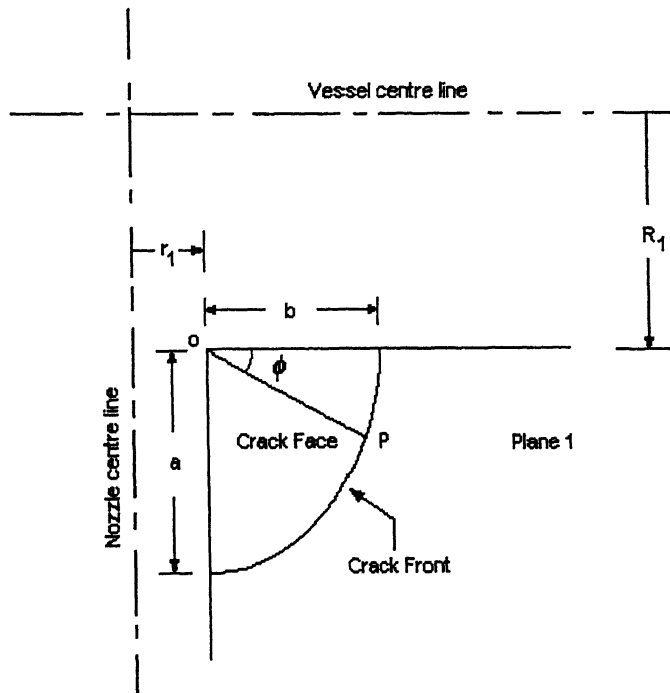


**Figure 4.1 Crack Configuration and dimensional parameters.**

It may be worth mentioning here, that the dimension of the corner crack in the nozzle direction is naturally more than that in the vessel direction, because in this case, the SIF along the crack front is more uniform, and the natural tendency of the crack is to grow in such a manner that the variation of SIF along the crack front is least.

The aspect ratio of the crack is defined as the ratio of the crack width ( $b$ ) to the crack depth ( $a$ ), so that, it is always less than unity.

The location of any point P, on the crack front is characterized by the angle  $\phi$  as shown in Figure 4.1.

### 4.3 FE Modeling and Analysis

Again, ANSYS 5.4 has been used for the modeling and analysis of the nozzle-vessel intersection with corner crack. Due to the presence of the crack at the above described location, the symmetry condition about the plane containing the axis of the nozzle and perpendicular to the axis of the vessel (Plane 3 in Figure 3.2), which prevails in the absence of the crack, is not prevalent now. Therefore, in this case, a semi-section of the nozzle has been modeled along with a quarter section of the vessel, rather than a quarter section of the nozzle, which is the case in the absence of the crack. A vessel length of 3 m and a nozzle length of 0.5 m have been taken in the model (Figure 4.2).

Since the crack is in the crotch region, it is realized that the inner fillet may have a significant effect on the crack. But the outer fillet is still far away from the crack and is unlikely to have any significant effect on the stress state near the crack. That is, the inner fillet falls within the region of interest, and hence, it has been included in the model.

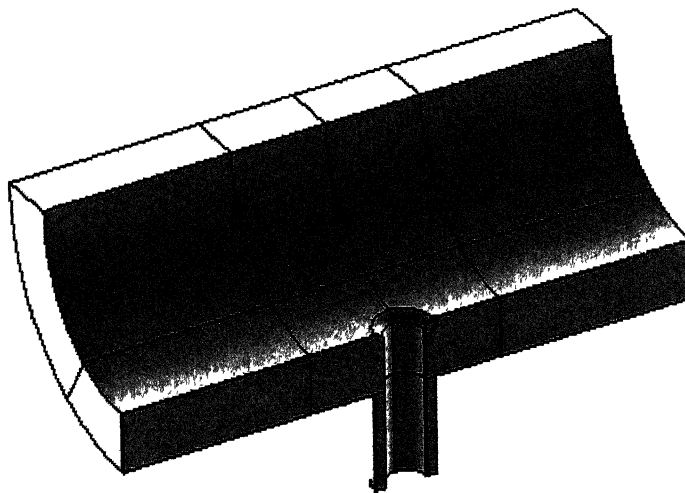


**Figure 4.2 Solid model of nozzle-vessel intersection with corner crack.**

The details of the modeling of the crack are shown in Figure 4.3. The dimensions of the crack are: Crack Depth = 80 mm, Aspect Ratio = 0.8. A small region above, and below the crack front (with a thickness of 5 mm in the direction normal to the crack front); have been modeled as separate regions, with the intention to mesh them with hexahedral elements (rather than tetrahedral elements). This is because, as it will be seen in Section 4.7, a structured mesh (not possible with tetrahedral elements) is required near the crack front, for the purpose of evaluation of SIF. Again, each of these small regions has been further divided in to five sub-regions by partitions orthogonal to the crack front. This is done to ensure the meshing of these volumes in such a way that the element edges in the plane of the crack face (the de-bonded surface above the crack front is referred to as crack face, as shown in Figure 4.3) are orthogonal to the crack front. This is required (as will be seen in Section 4.7) for a better accuracy in the evaluation of SIF.

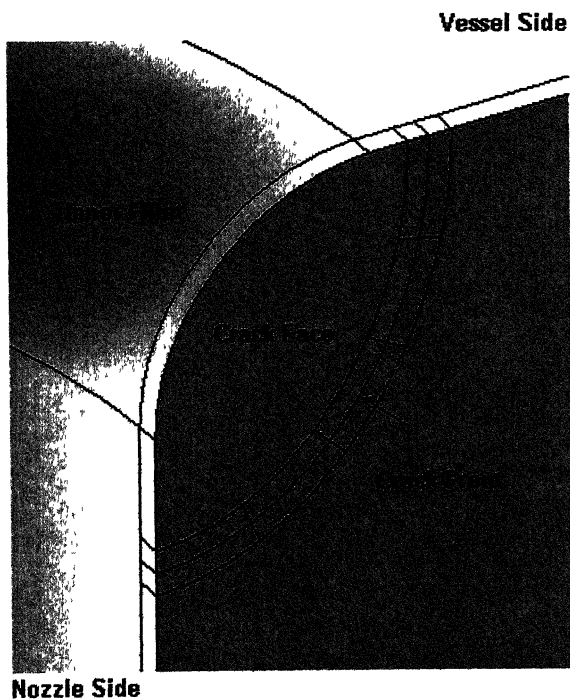


**Figure 4.3 Enlarged view of the near-crack region.**

The above model (Figure 4.2) is then meshed with a combination of 20-noded hexahedral elements and 10-noded tetrahedral elements. The region near the crack front has been meshed with 160 hexahedral elements, with 20 elements along the crack front, 2 elements above and 2 elements below the crack front, and 2 elements in the direction perpendicular to the crack face (as shown in Figure 4.4). The total number of elements in the discretized model is 15386, comprising of 2348 hexahedral elements and 13038 tetrahedral and transition elements. The total number of nodes is 32804, which amounts to a total of 98412 degrees of freedom.

There are two main reasons for this manifold increase in the number of elements required for the discretization, as compared to the case of stress analysis without crack. Firstly, a relatively finer mesh has been used in the crotch region, to effectively capture the high stress gradients existing near the crack. Secondly, the additional portion that has to be modeled because of the non-symmetry about Plane 3, due to the presence of the crack.

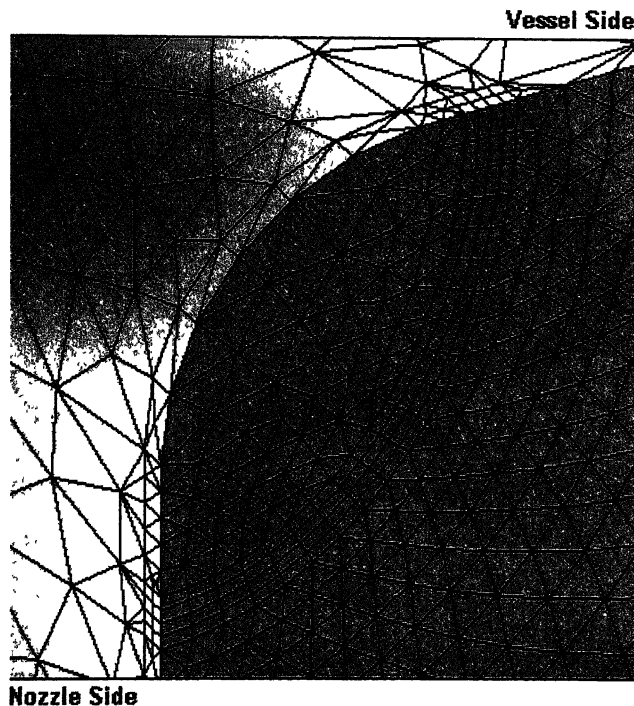


**Figure 4.4 FE discretization of the near-crack region.**

A fine mesh near the crack is essential, however, since the effect of a crack is local, it is possible that the symmetry condition about Plane 3 is actually not disturbed much, and the symmetry boundary condition is still applicable to the plane.

To test the validity of the above realization, stress analysis has been performed with the full model (Figure 4.2), and also with a half model (as shown in Figure 4.5), assuming symmetry about Plane 3, and the results are compared. The total number of elements in the half model is 9971, comprising of 1254 hexahedral elements and 8717 tetrahedral and transition elements, and the total number of nodes is 20484. The material properties used in the analyses are: Young's modulus,  $E = 210 \text{ GPa}$ , and Poisson's ratio,  $\nu = 0.3$ .

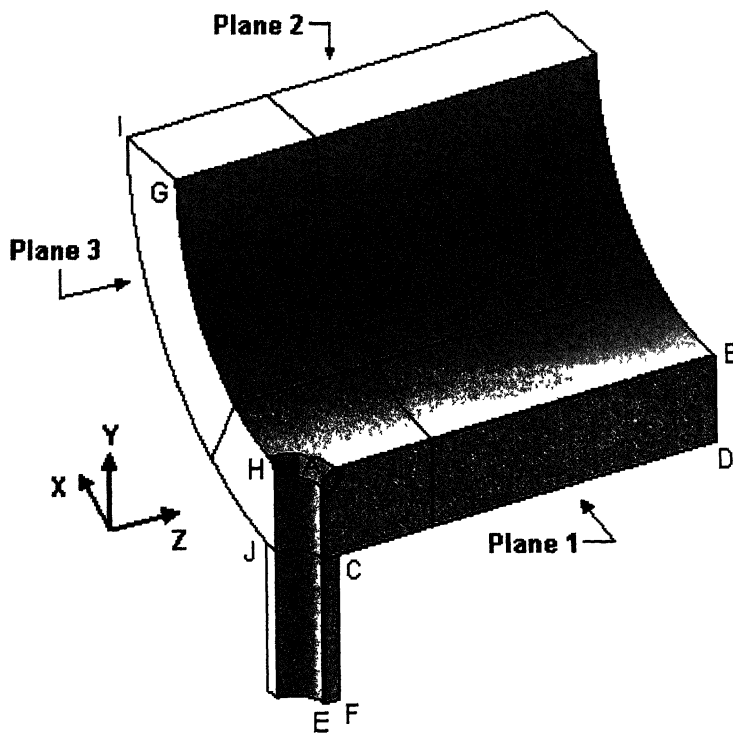


**Figure 4.5 Half model with definitions of paths and coordinate axes.**

### 4.3.1 Load and Boundary Conditions

The load and boundary conditions applied during the stress analyses, with reference to Figure 4.5, are as follows:

Full model:

- 1) Symmetry boundary condition is applied to the Plane 1, excluding the crack face.
- 2) Plane 2 is restricted to move in the normal direction.
- 3) Internal pressure of magnitude 15 MPa is applied on the inner surfaces of both nozzle and vessel, and also on the crack face.
- 4) One of the longitudinal ends of the vessel is fixed in the normal direction and longitudinal traction is applied on the other, as described in section 3.3.1.
- 5) Traction boundary condition is applied to the longitudinal end of the nozzle, as per section 3.3.1.

Half model:

- 1) Symmetry boundary condition is applied to the Plane 1, excluding the crack face.
- 2) Plane 2 is restricted to move in the normal direction.
- 3) Symmetry boundary condition is applied to the Plane 3.
- 4) Internal pressure of magnitude 15 MPa is applied on the inner surfaces of both nozzle and vessel, and also on the crack face.
- 5) Traction boundary conditions are applied to the longitudinal ends of the vessel and the nozzle, as per section 3.3.1.

### 4.3.2 Comparison of Results for Full and Half Models

To compare the results of stress analyses for full and half models, two paths have been chosen on Plane 3, corresponding to the inner and outer radii of the vessel, Path G-H and Path I-J (as shown in Figure 4.5), and various stresses are plotted along these paths, for both full and half models and

are compared in Figures 4.6-4.11. In Figure 4.12, the variation of the crack opening stress (stress in X-direction) along the crack front has been compared for full and half models.

As it is obvious from Figures 4.6-4.11, the state of stress on Plane 3 is more or less the same for full and half models. This indicates that Plane 3 does not really feel the presence of the crack much, and therefore it can still be considered as a plane of symmetry.

It is observed from Figure 4.12, that the crack opening stress, as estimated by the half model, is slightly on the higher side consistently, the maximum difference being less than 2%. This is expected, since, the assumption of symmetry about Plane 3 is equivalent to the presence of another corner crack located symmetrically on the other side of Plane 3.

It is concluded that, by the assumption of symmetry about Plane 3, a very little error creeps in to the solution, and that too, on the conservative side, and hence the half model can be used for stress analysis of the nozzle-vessel intersection with corner crack.

Finally, quarter-point elements (as discussed in Section 4.7) have been incorporated near the crack in the half model, to simulate the square root singularity that exists near a sharp crack (Section 4.5), and stress analysis has been performed. 20-noded brick elements with the quarter-point configuration of the mid-side nodes (adjacent to the nodes S), as shown in Figure 4.23(c), have been used as singular elements. The results of stress analysis of the half model after incorporating the singular elements are discussed in Section 4.4.

## **4.4 Stress Analysis Results and Discussion**

The results of the stress analysis after incorporation of singular elements are presented in the form of plots in Figures 4.13-4.18. These plots show the variation of stresses in different directions along the Paths A-B and A-E (defined in Figure 4.5). It is clearly seen that the stresses at the crack tip become very high as compared to the stresses in the surrounding. Both the paths fall along the element edges of the singular elements near the crack front, and hence, square root nature is expected in the singularity. Figures 4.19 and 4.20, which show closer views of the stresses near the crack tips, demonstrate the square root nature clearly. Square root singularity is well achieved within the first element (which is quarter-point element) beyond the crack front.



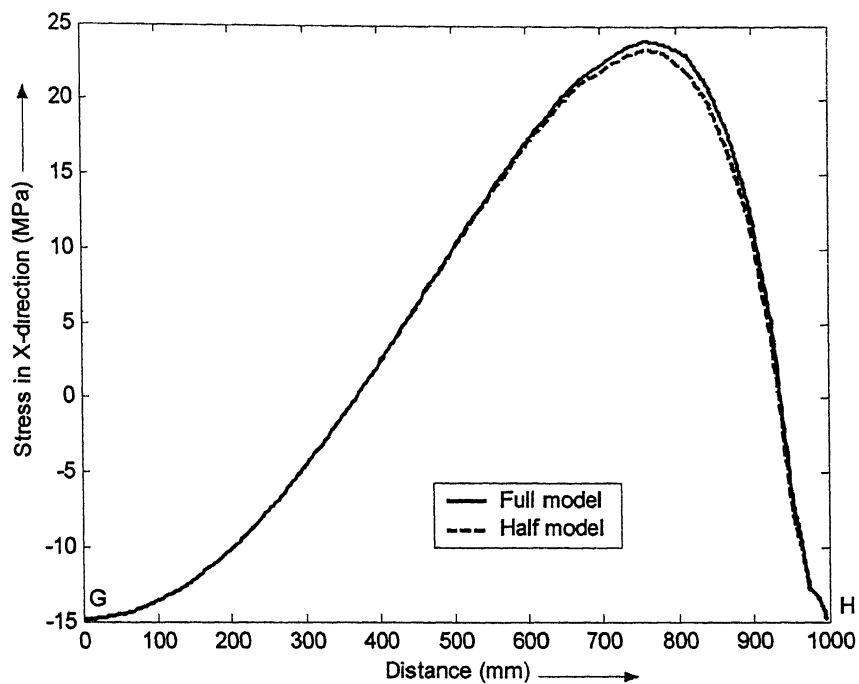


Figure 4.6 Stress in X-direction along path G-H.

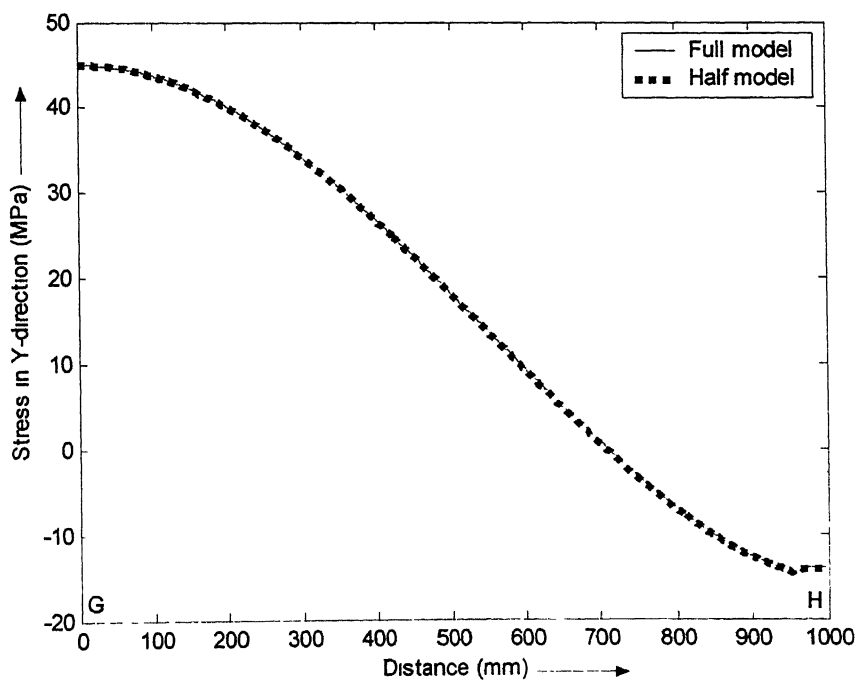
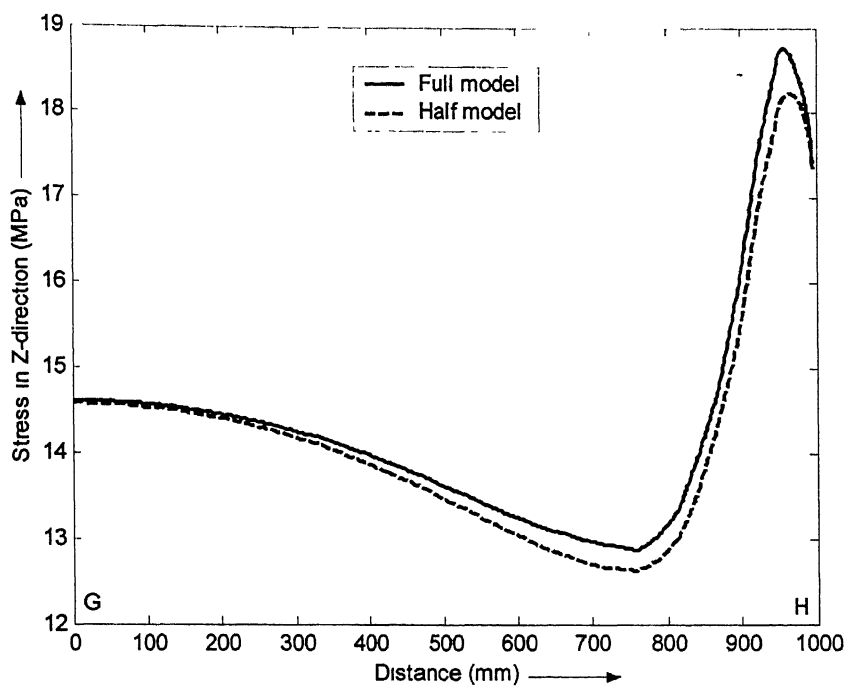
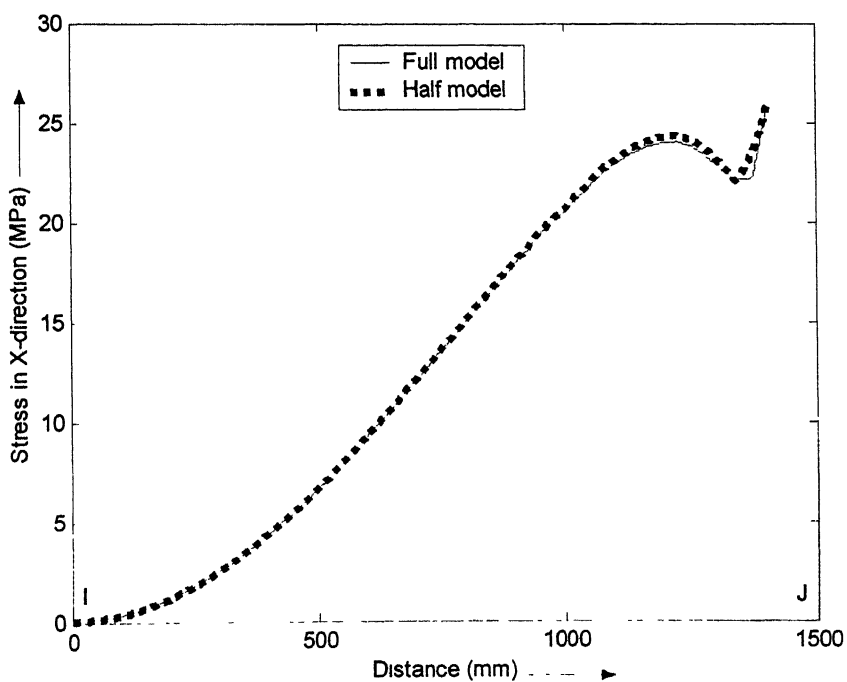


Figure 4.7 Stress in Y-direction along path G-H.



**Figure 4.8 Stress in Z-direction along path G-H.**



**Figure 4.9 Stress in X-direction along path I-J.**

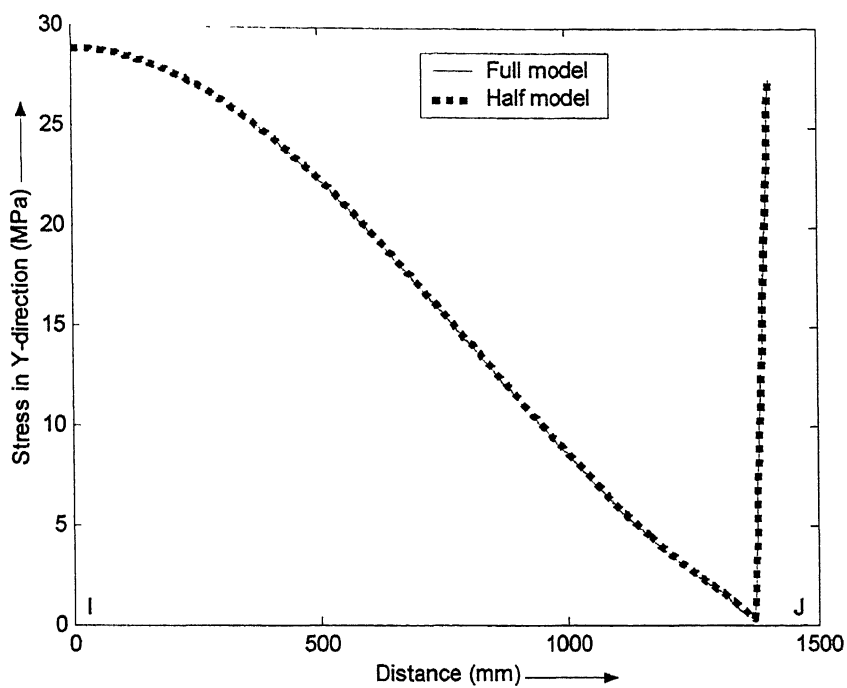


**Figure 4.10 Stress in Y-direction along path I-J.**

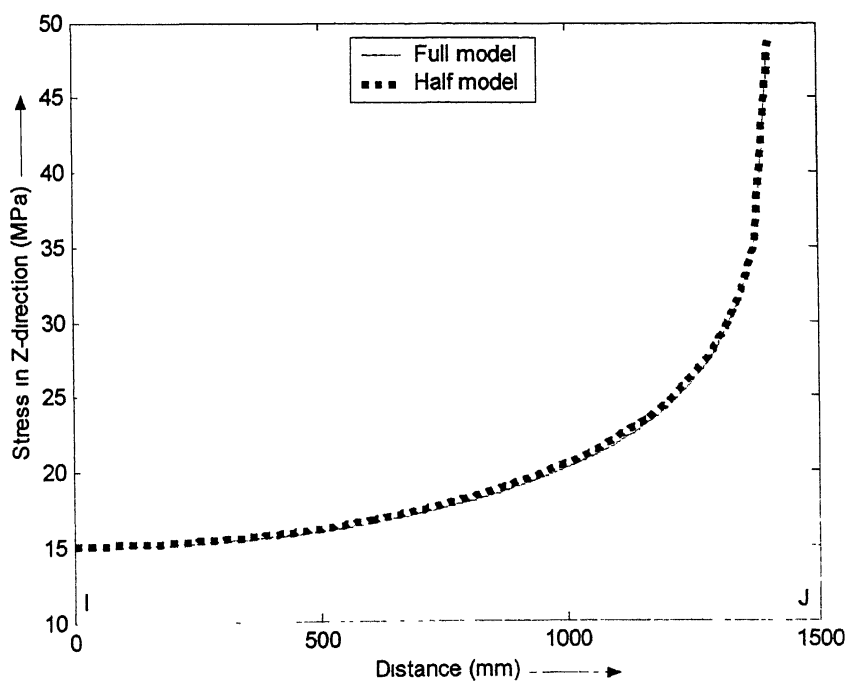


**Figure 4.11 Stress in Z-direction along path I-J.**

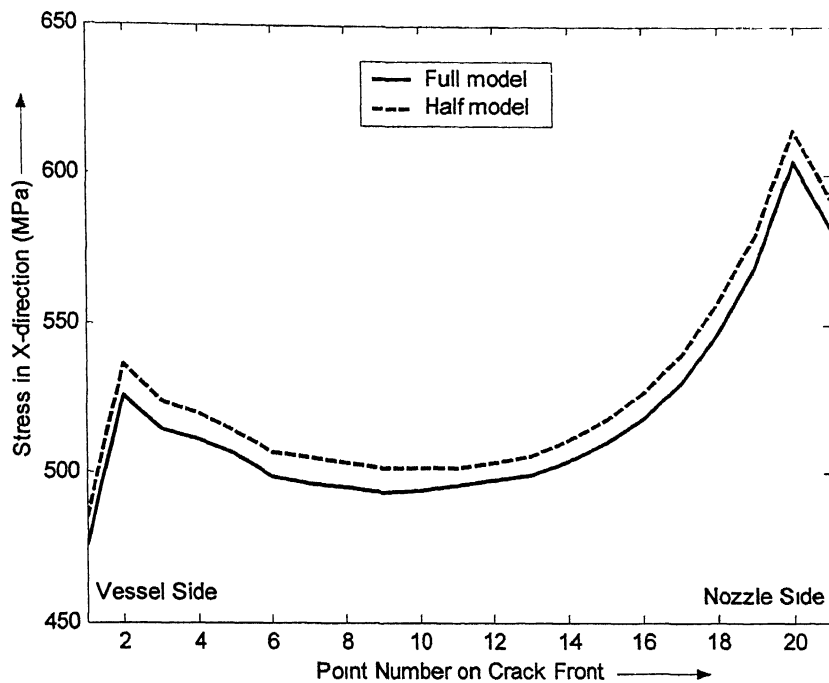


Figure 4.12 Stress in X-direction along the crack front.

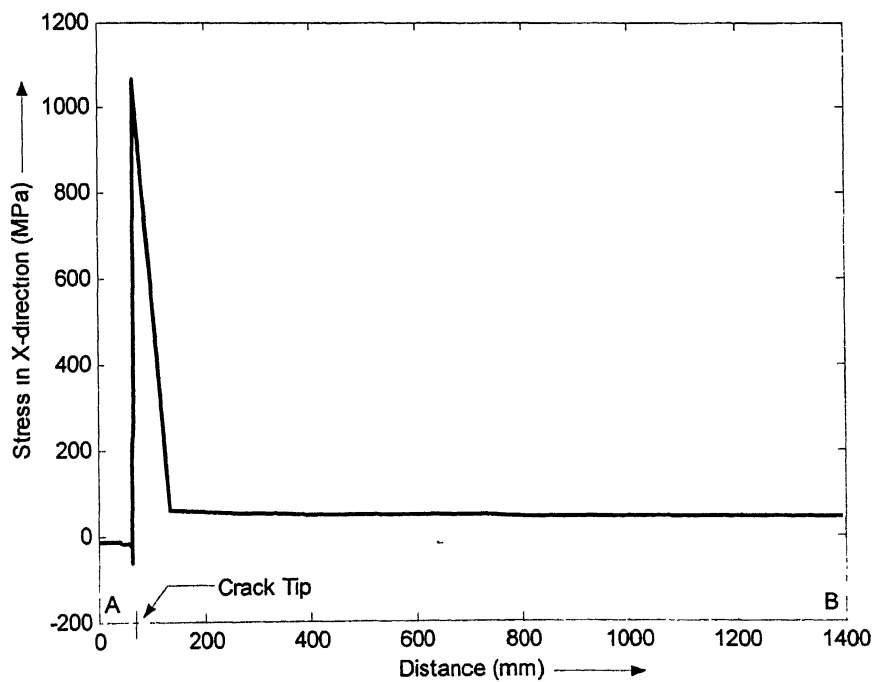
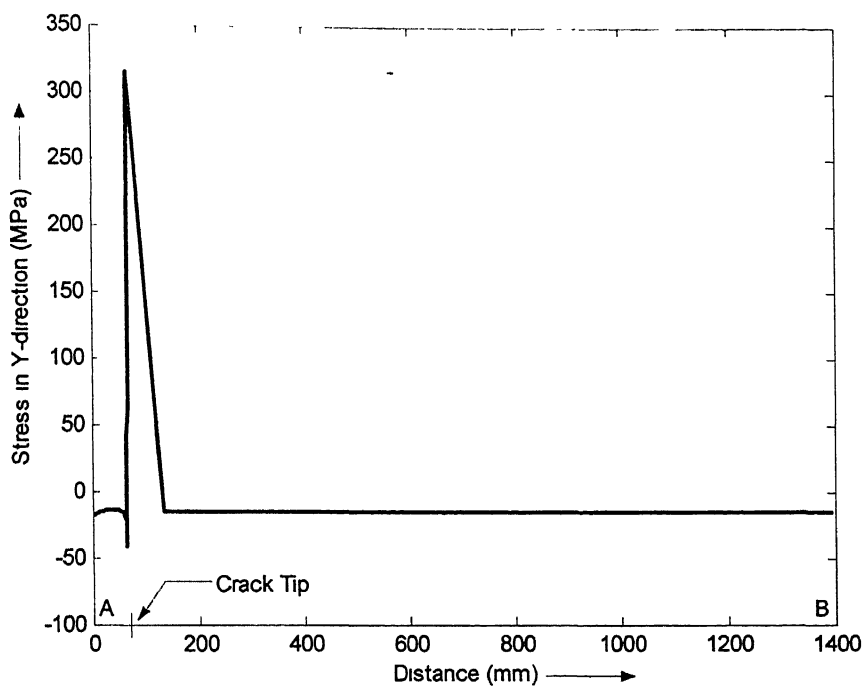
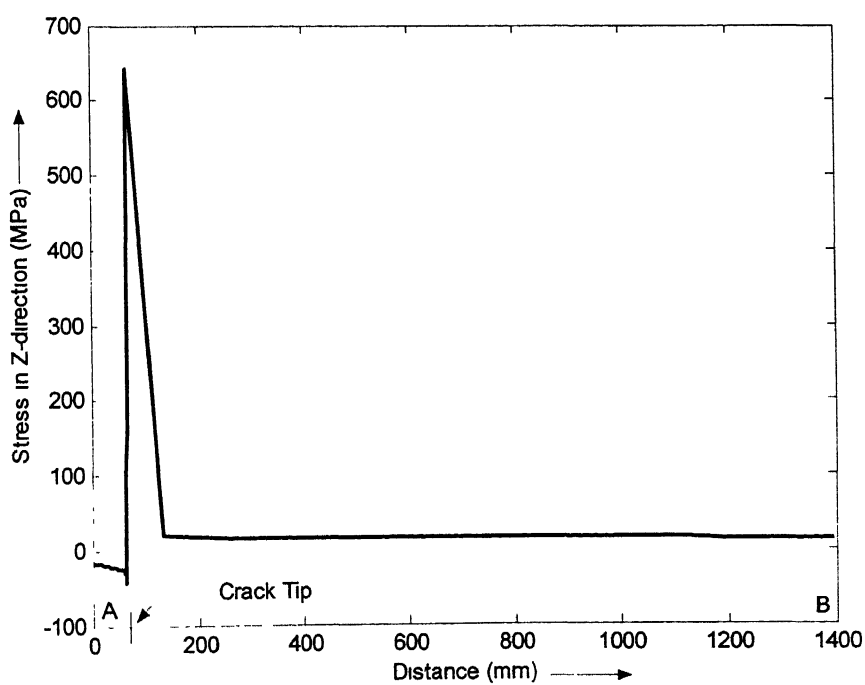


Figure 4.13 Stress in X-direction along Path A-B.



**Figure 4.14 Stress in Y-direction along Path A-B.**



**Figure 4.15 Stress in Z-direction along Path A-B.**

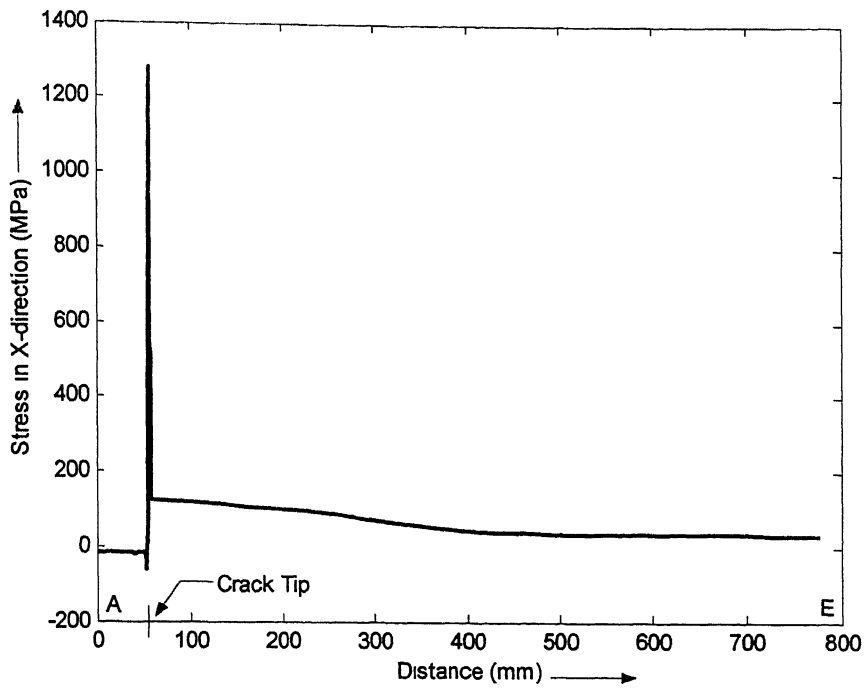


**Figure 4.16 Stress in X-direction along Path A-E.**

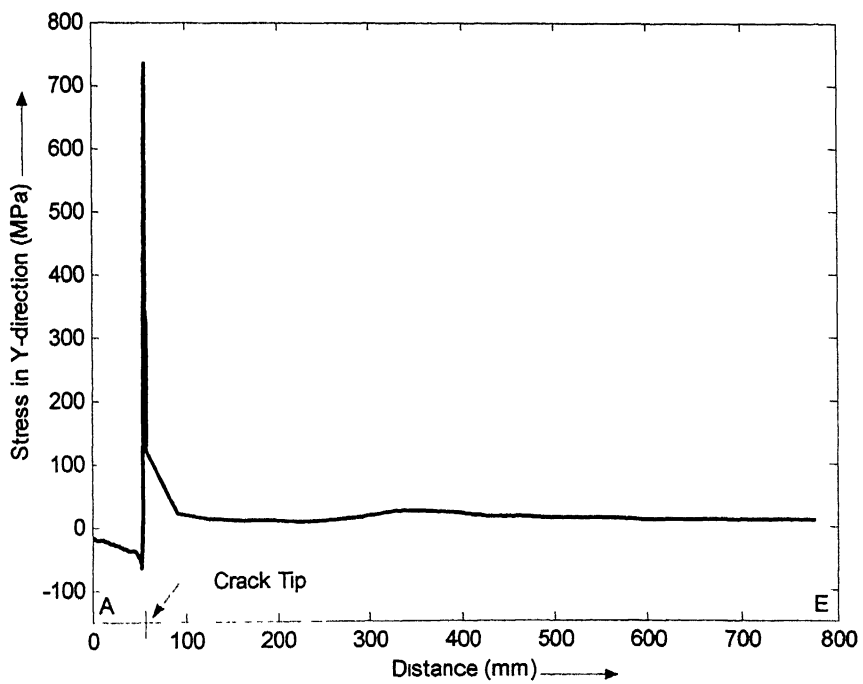


**Figure 4.17 Stress in Y-direction along Path A-E.**

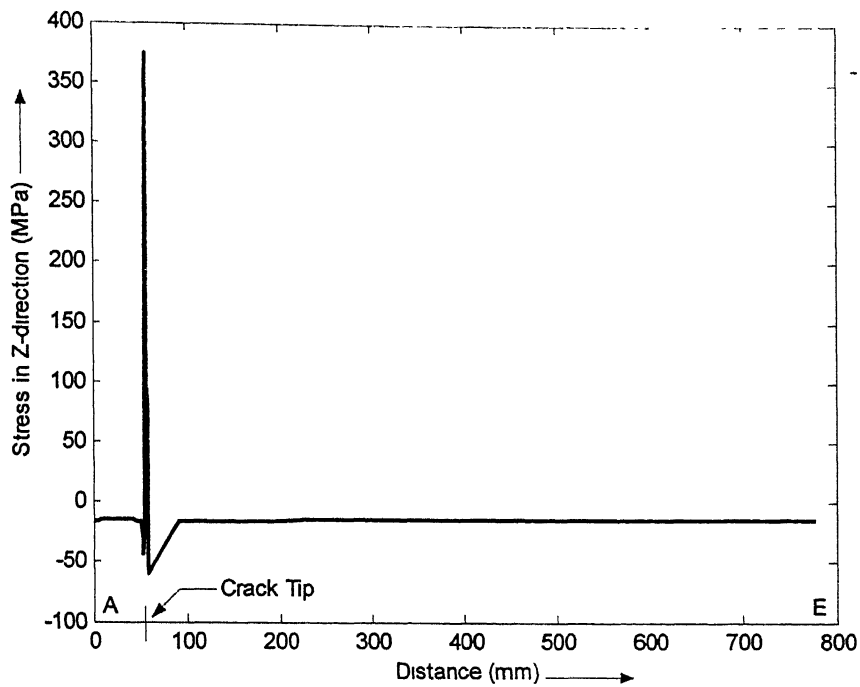


Figure 4.18 Stress in Z-direction along Path A-E.

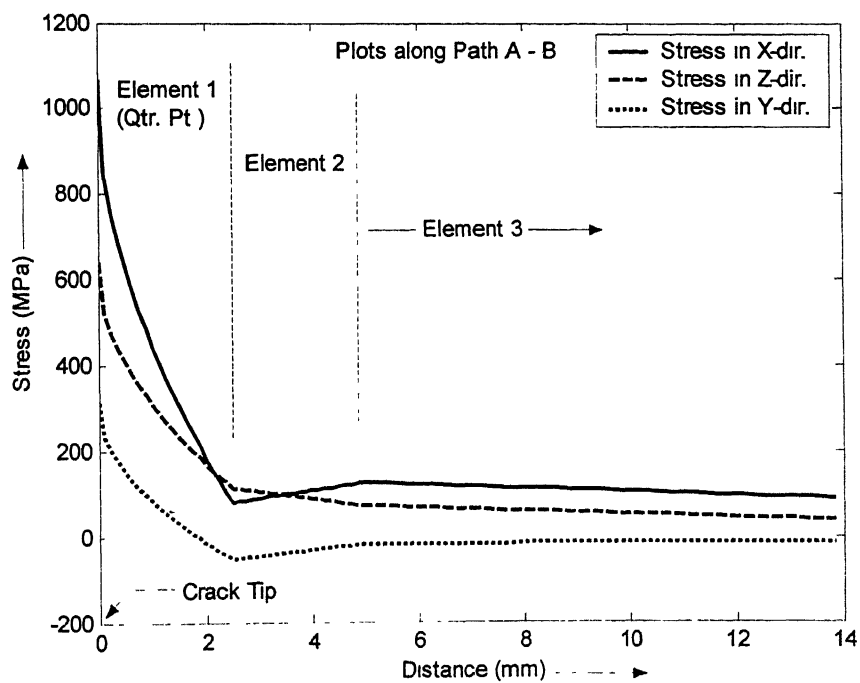


Figure 4.19 Square root nature of singularity near the crack tip along Path A-B.

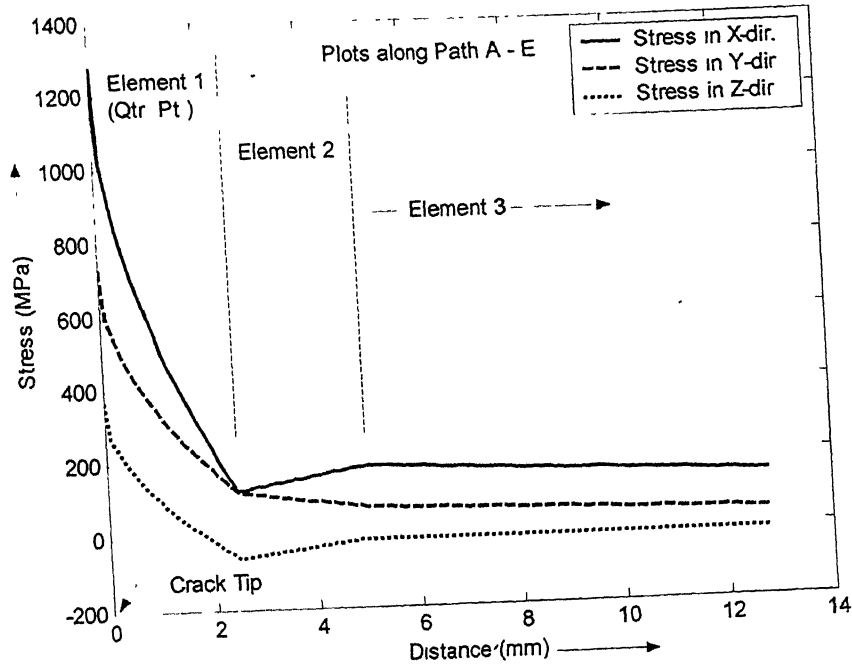


Figure 4.20 Square root nature of singularity near the crack tip along Path A-E.

## 4.5 Stress Intensity Factor

It can be shown [22, 23] that the stress field at any arbitrary point, Q, in the vicinity of the crack tip, T (Figure 4.21), for isotropic, linear elastic material, for the case of mode I loading, in an infinite flat plate with a through-thickness crack of length  $2a$ , is given by:

$$\sigma_{11} = \frac{\sigma(\pi a)^{1/2}}{(2\pi r)^{1/2}} \cos \frac{\theta}{2} \left[ 1 - \sin \frac{\theta}{2} \sin \frac{3\theta}{2} \right], \quad (4.1a)$$

$$\sigma_{22} = \frac{\sigma(\pi a)^{1/2}}{(2\pi r)^{1/2}} \cos \frac{\theta}{2} \left[ 1 + \sin \frac{\theta}{2} \sin \frac{3\theta}{2} \right], \quad (4.1b)$$



$$\sigma_{12} = \frac{\sigma(\pi a)^{1/2}}{(2\pi r)^{1/2}} \sin \frac{\theta}{2} \cos \frac{\theta}{2} \cos \frac{3\theta}{2}, \quad (4.1c)$$

where,  $\sigma$  is the far field stress;  $r$  and  $\theta$  are the polar coordinates of the point Q, with the origin stationed at the crack tip T, and  $\theta$  being measured anticlockwise from the extended crack line.

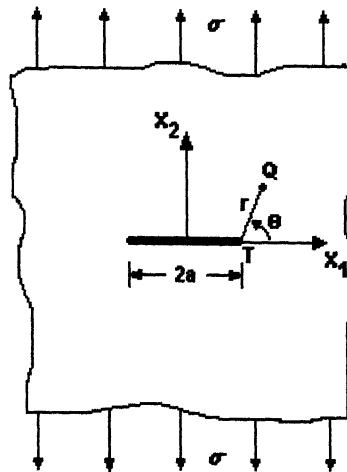


Figure 4.21 Through-thickness Crack in an infinite flat plate.

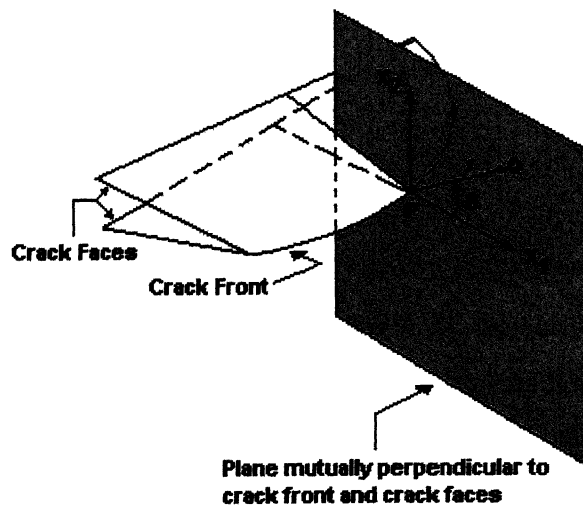


Figure 4.22 Stress field around an embedded elliptical flaw.

The coordinate axes,  $X_1$  and  $X_2$ , being along, and perpendicular to the extended crack line, respectively. Here,  $\sigma_{ij}$  denotes the component of stress that acts in the direction of the  $j^{th}$  coordinate axis on a plane whose normal is along the  $i^{th}$  coordinate axis.

For a thin plate (plane stress case), the other stress components are negligible. In case of a thick plate (plane strain case),  $\sigma_{33} = \nu(\sigma_{11} + \sigma_{22})$ , where,  $\nu$  is the Poisson's ratio of the material; and the remaining two stress components are negligible.

It can be seen from Equations 4.1, that the distance ( $r$ ) between the crack tip and the point occurs in the denominator under a square root sign, in all the stress components. If  $r$  becomes very small, the stress components rise very sharply and tend to become infinite as  $r \rightarrow 0$ . This means that the stresses become singular at the crack tip, and the particular kind of singularity encountered here is known as square root singularity because of the  $1/\sqrt{r}$  nature of the stress field.

Also, it can be observed from Equations 4.1, that the quantities  $\sigma$  and  $a$  always coexist as  $\sigma\sqrt{\pi a}$  in all the equations of the stress field. Apart from these quantities, the other variables ( $r$  and  $\theta$ ) occurring in the field equations are merely geometrical variables defining the location of a point in the vicinity of the crack tip. This indicates that the product  $\sigma\sqrt{\pi a}$  completely characterizes the state of stress existing in the vicinity of the crack. Hence, it is advantageous to recognize the product as a single parameter which can characterize the state of the crack completely.

The idea was first proposed by Irwin in 1957, who defined the product as a new parameter, stress intensity factor, which is formally defined as:

$$K_I = (2\pi r)^{1/2} \sigma_{22}(r, \theta = 0), \text{ as } r \rightarrow 0, \quad (4.2)$$

where, the subscript  $I$  denotes mode I loading. It can be verified that by substituting Equation 4.1b in the formal definition (Equation 4.2), one can obtain  $K_I = \sigma\sqrt{\pi a}$ .

The field equations can now be conveniently re-written in terms of the stress intensity factor  $K_I$ . The corresponding displacement field in the vicinity of the crack tip, in terms of  $K_I$ , is given by:

$$u_1 = \frac{1+\nu}{4E} \left( \frac{2r}{\pi} \right)^{\frac{1}{2}} K_I \left( (2\kappa-1) \cos \frac{\theta}{2} - \cos \frac{3\theta}{2} \right), \quad (4.3a)$$

$$u_2 = \frac{1+\nu}{4E} \left( \frac{2r}{\pi} \right)^{\frac{1}{2}} K_I \left( (2\kappa+1) \sin \frac{\theta}{2} - \sin \frac{3\theta}{2} \right), \quad (4.3b)$$

$$u_3 = 0, \quad (4.3c)$$

where,  $E$  is the Young's modulus of the material; and  $\kappa = 3 - 4\nu$  for plane strain, and  $(3 - \nu)/(1 + \nu)$  for plane stress. Here,  $u_i$  denotes the displacement along the  $i^{th}$  coordinate axis.

## 4.6 SIF for Three-Dimensional Crack Problems

Real life crack problems are usually three dimensional, and involve part-through cracks, rather than through-thickness cracks. Part-through cracks (embedded or surface cracks) usually have curved crack fronts, which are modeled as elliptical, semi-elliptical or quarter-elliptical in the literature of fracture mechanics.

Kassir and Sih [24] have demonstrated that, for the case of an embedded elliptical flaw, the singular stresses in the vicinity of any arbitrary point on the flaw border, in a plane mutually perpendicular to the flaw border and the crack faces, take the same functional form as the Irwin field equations for the two-dimensional problem.

Figure 4.22 describes the above statement pictorially. Consider a cracked surface bounded by an elliptical crack front as shown in Figure 4.22. To understand the state of stresses around the crack profile, consider any point P (crack tip) on the crack front. Assume a plane cutting the crack faces such that, it is normal to the crack front at point P, and also perpendicular to the crack faces. Then, according to the work of Kassir and Sih [24], the stress field around the point P in the above plane is of the same form as that of the two dimensional problem of through-thickness crack in an infinite flat plate, and the stress and displacement components at a point Q (Figure 4.22) on the plane, in the vicinity of the point P are given by Equations 4.1 and 4.3 respectively, with the

definitions of the coordinate axes and the polar coordinates of point Q, as shown in Figure 4.22. This defines the SIF at point P. Thus, for a three-dimensional crack, there exists a continuous distribution of SIF over the crack front, rather than a single value.

## 4.7 Numerical Evaluation of SIF

The procedure for numerical evaluation of SIF has been described in detail by Hellen and Dowling [3]. The method makes use of the basic displacement field relations given by Equations 4.3. To evaluate the SIF at a given crack tip, the values of displacement (from the results of stress analysis) at nodes around the crack tip node are conveniently used in these equations, although first it is necessary to transform the displacement components from the global to the local directions as per Figure 4.22.

Since the displacement field equations are valid in a plane mutually perpendicular to the crack front and the crack faces, it is necessary to have nodes in such planes corresponding to all the crack tip nodes. This is possible only if structured mesh is used near the crack front. With a structured mesh using quadratic brick elements, nodes exist along the  $\theta = \pi/2$  line, and also along the  $\theta = \pi$  line (if it is ensured that the meshing is such that the element edges in the plane of the crack face are orthogonal to the crack front). But it has been observed that the results of  $\theta = \pi$  line are more accurate than those of  $\theta = \pi/2$  line [3].

Denoting the component of displacement in the direction normal to the crack face by  $v$ , one can obtain, from Equation 4.3b:

$$v = \frac{(1+\nu)(1+\kappa)}{2E} \left( \frac{2r}{\pi} \right)^{\frac{1}{2}} K_I, \quad \text{for } \theta = \pi \text{ line}, \quad (4.4a)$$

$$v = \frac{(1+\nu)(\kappa)}{2E} \left( \frac{r}{\pi} \right)^{\frac{1}{2}} K_I, \quad \text{for } \theta = \pi/2 \text{ line}. \quad (4.4b)$$

Since two nodes lie along either line in the crack tip elements, two independent results for  $K_I$  are obtained using either of the Equations 4.4. However, Equations 4.3 do not include the homogeneous strain terms which occur in reality, such as a large hoop stress or thermal strains. Since the finite element model includes such effect as a linear function of  $r$ , a linear correction is required, to give Equation 4.4 as:

$$v = C \left[ K_I(r)^{1/2} + Lr \right], \quad (4.5)$$

where,  $C$  and  $L$  are constants to be eliminated. Using the subscript  $m$  for values at the mid side node and  $v$  for values at the corner node, and noting that  $r_v = 4r_m$  (for quarter-point crack tip element),

$$v_m = C \left[ K_{Im}(r_m)^{1/2} + Lr_m \right], \quad (4.6a)$$

and 
$$v_v = C \left[ K_{Iv}(r_v)^{1/2} + Lr_v \right]. \quad (4.6b)$$

However, Equation 4.3b may still be used if an equivalent value  $K_I^*$  is used such that:

$$v = CK_I^*(r)^{1/2}. \quad (4.7)$$

By inspection of Equations 4.6 and 4.7, use of such a  $K_I^*$  requires the following conditions to be true:

$$K_I^*(r_m)^{1/2} = K_{Im}(r_m)^{1/2} + Lr_m, \quad (4.8a)$$

and 
$$K_I^*(r_v)^{1/2} = K_{Iv}(r_v)^{1/2} + Lr_v. \quad (4.8b)$$

By suitable manipulation of Equations 4.8, and using  $r_v = 4r_m$ , one obtains:

$$K_I^* = K_{Iv} + 2(K_{Im} - K_{Iv}). \quad (4.9)$$

Equation 4.9 can be used to evaluate the SIF values at the crack tip nodes using the displacement field obtained from stress analysis. Improved results are obtained [3] by the use of Equation 4.9.

Also, it is important to simulate the square root singularity existing at the crack front, during the stress analysis, to get reasonable results. One of the simplest and most popular methods of simulating singularity is the use of quarter-point elements near the crack. An element of this kind [25], shown in Figure 4.23(a), introduced almost simultaneously by Henshell [26] and Barsoum [27] for 2D problems, develops by a simple shift of the mid-side nodes (adjacent to the corner node at which singularity is desired, indicated by 'S' in the Figure) in quadratic, isoparametric quadrilateral elements, to the quarter point locations.

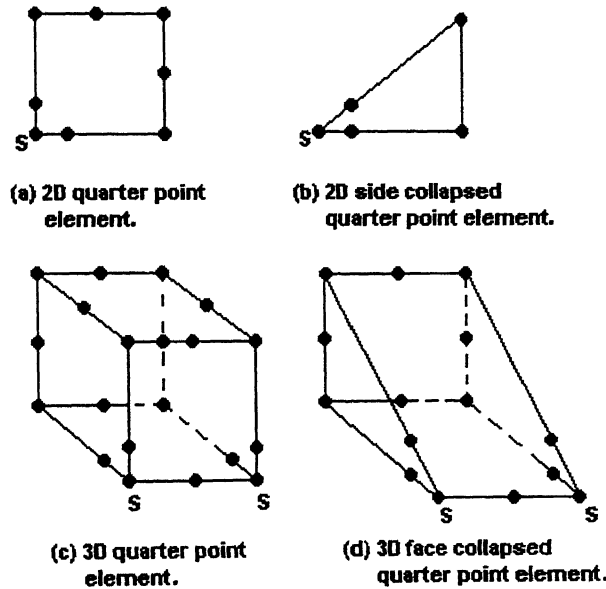


Figure 4.23 Quarter point Elements for simulation of singularity.

Singularity develops at the node S because, in the particular quarter-point configuration of the mid-side nodes, the determinant of the Jacobian becomes zero at the node S. It can be shown that along the element edges, the derivatives  $\partial u/\partial x$  (or strains), and hence stresses, vary as  $1/\sqrt{r}$ , where  $r$  is the distance from the corner node S, at which the singularity develops.

A better element for the purpose, as shown in Figure 4.23(b), is the side collapsed quarter-point element [24] proposed by Hibbitt [28], in which, square root singularity is achieved in any radial direction emanating from the corner node S.

Although singularity is not well modeled on lines other than element edges in the quadrilateral quarter-point element, as it is done in case of the side collapsed element, yet, reasonably good results are achievable [25] with such elements.

All the above ideas can be extended to 3D [29], and quarter-point elements can be developed from second order 3D elements, as shown in Figures 4.23(c) and (d), for simulation of singularity in 3D crack problems.

The above described technique has been used to evaluate the SIF values for nozzle-corner cracks in the present work. SIF values have been evaluated along the crack profiles for two different crack configurations:

- 1) Crack-I : Crack Depth = 80 mm, Aspect Ratio = 0.8; representing medium to large cracks.
- 2) Crack-II : Crack Depth = 35 mm, Aspect Ratio = 1.0; representing shallow cracks confined within the fillet region.

Stress analysis has been performed for both the crack configurations using quarter-point elements near the crack front, with the same load and boundary conditions as described in Section 4.3.1. SIF values for Crack-I have been evaluated along the profile, for  $\theta = \pi$  line.

For Crack-II, it has not been possible to mesh the region near the crack with element edges in the crack plane orthogonal to the crack front throughout the profile, because of the intersection of the crack front with rounded edges. Therefore, for Crack-II, SIF values have been evaluated for  $\theta = \pi/2$  line.

The plane stress relations have been used at the end points of the profile (which lie at free surfaces), and plane strain relations have been used at all inner points, for both the cracks.

## 4.8 SIF Results and Discussion

The variation of SIF along the crack profile for Cracks-I and II, as evaluated by the method described in Section 4.7, have been shown in Figures 4.24 and 4.25 respectively. In these figures, the SIF values at the crack tip nodes have been plotted against the angular position (angle  $\phi$  as shown in Figure 4.1) of the nodes. The angle  $0^\circ$  corresponds to the vessel-side end point of the crack front, while the angle  $90^\circ$  corresponds to the nozzle-side end point of the crack front.

It is seen that, for Crack-I, the SIF has higher values near the free surfaces (except in very thin regions near the surfaces), and tend to decrease towards the inner side, with a (local) minimum value at around  $\phi = 45^\circ$ . The average SIF over the profile is about  $848 \text{ MPa}\sqrt{\text{mm}}$ , with a percentage variation of SIF of about 21 % over the profile (defined as the percent ratio of the difference between the maximum and minimum SIF values over the profile excluding the end points, to the average SIF). The higher values of SIF near the end points may be expected, because these regions exist near the inner radii of the cylinders, where the hoop stress has relatively higher values. It should also be noted that the SIF is higher near the nozzle side as compared to that near the vessel side. This indicates that such a crack will become critical first on the nozzle end and later on the vessel end (for pressure loading only), and hence there is a chance for leak-before-break.

It can be seen that the SIF falls off sharply in very thin layers near the free surfaces. This is not surprising, since very near to the free surfaces, plane stress condition exists. This tendency has also been verified from the work of Mohamed and Schroeder [9], wherein, it is clearly mentioned that the SIF actually drops near the free surfaces.

In the case of Crack-II, which is completely contained within the fillet region, it is seen that the pattern of variation of SIF along the profile is entirely different. The SIF values are higher inside and drop very sharply near the free surfaces. It has been verified from the work of Heliot et al. [30], that the shape of the SIF curve for shallow cracks confined within the fillet region is actually similar to the one shown in Figure 4.25. However, the SIF is still higher on the nozzle side than on the vessel side. The average SIF over the profile is about  $482 \text{ MPa}\sqrt{\text{mm}}$ , with SIF variation of about 25 % over the profile (excluding the end points).



## 4.9 Validation of SIF Results

To test the validity of the SIF results obtained in the present work, and to get an estimate of the order of accuracy of the results, two test problems (one 2D and the other 3D), whose handbook solutions are available, have been solved.

Also, the SIF results of the nozzle-corner crack problem as obtained from the present work are compared with the results obtained from an approximate empirical formula available in the literature.

### 4.9.1 2D Test Problem

A single-edge-notch-bend (SENB) specimen, as shown in Figure 4.26, has been analyzed using the 8-noded quadrilateral elements, with quarter-point crack tip elements. The plane strain condition has been assumed. With reference to Figure 4.26, the dimensions of the specimen analyzed are:

Span,  $S = 1\text{ m}$ , Width,  $W = 0.25\text{ m}$ , Thickness,  $B = 1\text{ m}$  (plane strain), Crack length,  $a/W = 0.5$ .

The load applied,  $P = 100\text{ N}$ . Only half the model is analyzed, exploiting the symmetry of the problem. SIF is evaluated using the method described in Section 4.7. The value of SIF obtained is  $2193.6\text{ Pa}\sqrt{\text{m}}$ .

The SIF is also calculated from the Handbook Solution for SENB specimen [22], which is as follows:

$$K_I = \frac{PSf(a/W)}{BW^{3/2}}, \quad \text{where, } f(0.5) = 2.663. \quad (4.10)$$

The value of SIF obtained from this relation is  $2130.4\text{ Pa}\sqrt{\text{m}}$ . The error in the present result comes out to be  $+2.97\%$  (conservative).

### 4.9.2 3D Test Problem

This problem is taken from Murakami's Stress Intensity Factors Handbook [31]. The problem is that of a quarter-elliptical corner crack emanating from a central hole in a finite flat plate subjected to uniform tension, as shown in Figure 4.27. The crack is located in the diametral plane of the hole, parallel to the loaded face of the plate. The dimensions and load used in the analysis are:

Height of the plate,  $2H = 2400\text{ mm}$ , Width of the plate,  $2W = 1400\text{ mm}$ , Thickness,  $t = 100\text{ mm}$ , Radius of the hole,  $R = 100\text{ mm}$ , Crack Depth,  $a = 25\text{ mm}$ , Crack Width,  $b = 50\text{ mm}$ .

The load applied is a uniform mode I stress,  $\sigma = 15\text{ MPa}$  as shown in the Figure.

Only one-fourth of the geometry has been modeled (assuming quarter-symmetry) and analyzed, using 20-noded brick elements and incorporating quarter-point crack tip elements. SIF has been evaluated along the crack profile using the plane strain relations throughout. SIF is also calculated from the Handbook Solution [31], and the variation of both the SIF values along the crack profile have been compared in Figure 4.28.

The Handbook Solution is reported to match with FEM results within  $\pm 5\%$ . It shows a maximum difference of about  $\pm 7\%$  from the present FEM results, except for the first point. The difference in average SIFs is only 0.4%. From this comparison, it seems that the present FEM results are within  $\pm 2\%$  of the standard FEM results for the problem considered.

### 4.9.3 Comparison with Approximate Empirical Formula

The present results for a quarter-circular nozzle-corner crack are compared with the results obtained from the approximate empirical formula proposed by Mohamed and Schroeder [9]. The formula relates the SIF at a point on the crack front to the hoop stress existing at that point in the absence of the crack, employing the solution of an elliptical crack embedded in an infinite solid exposed to uniform tension, with some modifications. This is based on the assumption that the uncracked stress distribution reflects the influence of all the geometrical variables affecting the Stress Intensity Factor.

The SIF at any point P, at an angular position  $\phi$ , on the front of a nozzle-corner crack with depth =  $a_0$  and width =  $b_0$ , is given [9] as:

$$K_I(\phi) = M_f \frac{\sigma_a \sqrt{\pi a}}{E(k)} \left( \sin^2 \phi + \frac{b_0^2}{a_0^2} \cos^2 \phi \right)^{1/4}, \quad (4.11)$$

where,  $a$  is the crack length at  $\phi = 45^\circ$ ,  $M_f$  is the magnification factor for the front free surfaces which is given as a function of  $\phi$  in the form of a curve for different values of aspect ratio,  $\sigma_a$  is the hoop stress at point P in the absence of the crack, and,  $E(k)$  is the complete elliptical integral of the second kind:

$$E(k) = \int_0^{\pi/2} \left[ \sin^2 \phi + \frac{b_0^2}{a_0^2} \cos^2 \phi \right]^{1/2} d\phi. \quad (4.12)$$

From Equations 4.11 and 4.12, the SIF for a quarter-circular crack is given by:

$$K_I(\phi) = M_f \frac{\sigma_a \sqrt{\pi a}}{\pi/2}. \quad (4.13)$$

Figure 4.29 shows the variation of SIF along the crack front of an 80 mm deep quarter-circular nozzle-corner crack as obtained from the present work, and also from the empirical formula (Equation 4.13). In the present SIF results, plane stress relations have been used at the end points of the crack front, and plane strain relations have been used at all interior points.

The above comparison reveals that the results of the present work are matching, with a maximum difference of about 20 %, with the results of the empirical formula. The difference between the average SIFs is about 5 %.

It is reported by Mohamed and Schroeder [9], that their results match with the results of FEM with a maximum deviation of the order of 16 %. In lieu of the above, it seems that the present results match within 4 % with the standard FEM results for nozzle-corner cracks.

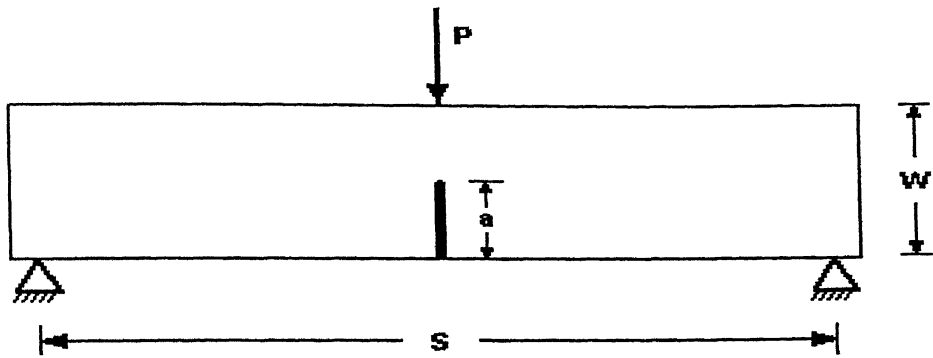


Figure 4.26 SENB specimen (2D test problem).

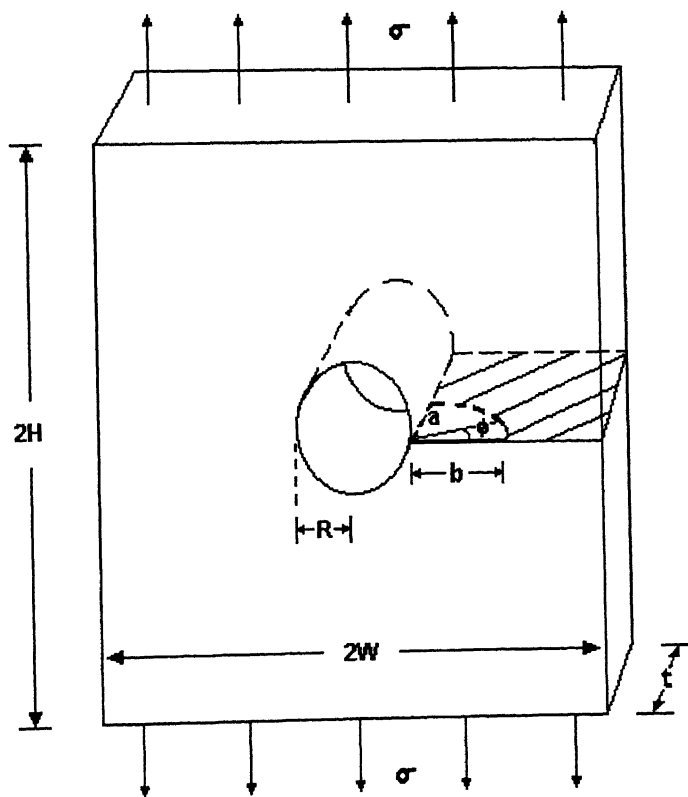


Figure 4.27 Geometry of the 3D test problem.

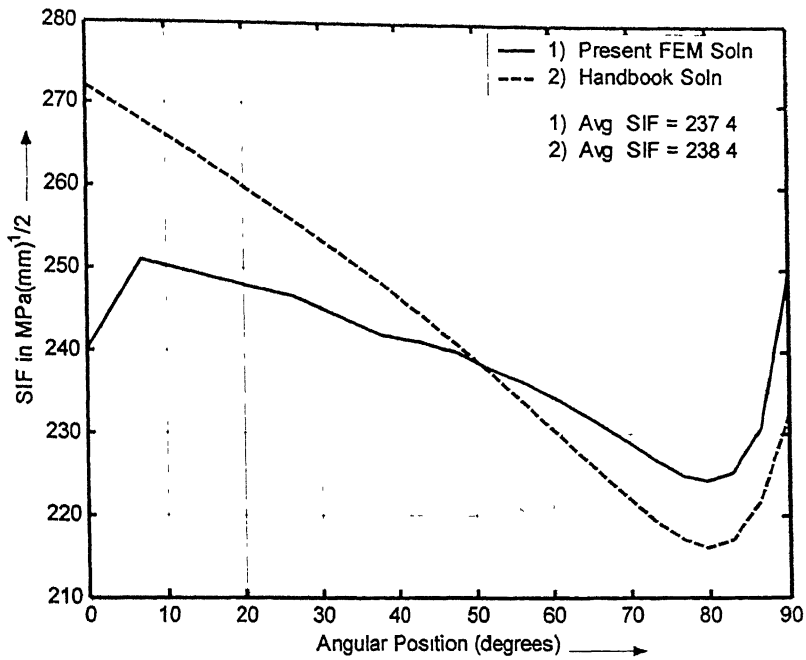


Figure 4.28 Comparison of SIF for 3D test problem.

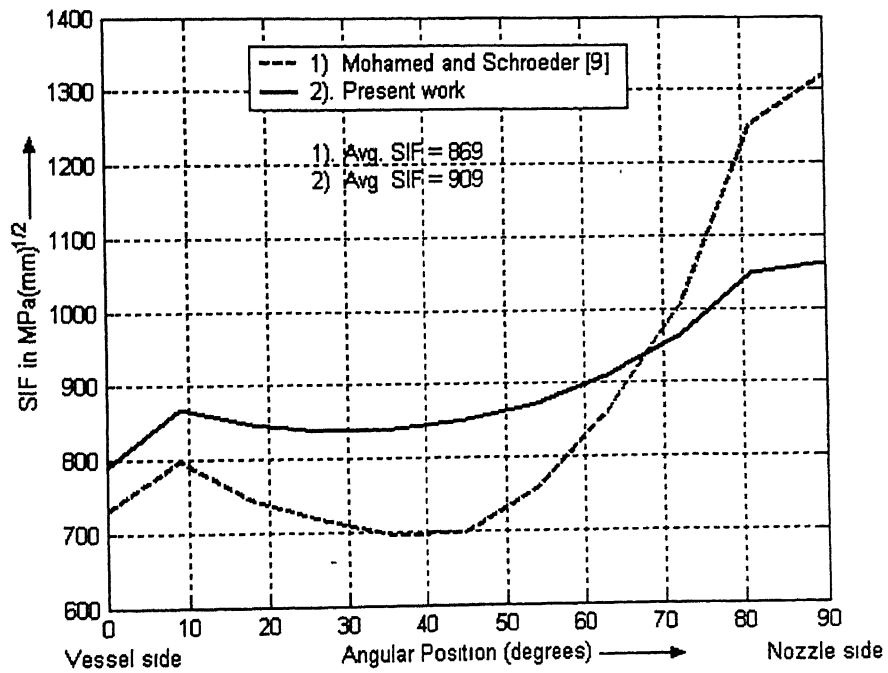


Figure 4.29 Comparison of SIF for 80 mm deep qtr-circular nozzle-corner crack with the results obtained from empirical formula [9].

## 4.10 Parametric Study

To understand the effect of different geometrical and crack parameters on the SIF of nozzle-corner cracks, parametric study has been performed by varying the parameters in the neighbourhood of their given values. Figures 4.30-4.33 show the variation of SIF along the profile of nozzle-corner cracks, for different values of crack and geometrical parameters. Since the analysis is linear with respect to the load (internal pressure), the load has not been taken as a parameter in the parametric study. All the results presented here correspond to an internal pressure of 15 MPa.

### 4.10.1 Normalization of the Parameters

The different geometrical parameters involved in the problem are:  $R_1$  (inner radius of the vessel),  $R_2$  (outer radius of the vessel),  $r_1$  (inner radius of the nozzle),  $r_2$  (outer radius of the nozzle), and  $r$  (inner fillet radius).

For the purpose of parametric study, these parameters have been taken as:  $D$  (mean diameter of the vessel),  $T$  (thickness of the vessel),  $d$  (mean diameter of the nozzle),  $t$  (thickness of the nozzle), and to reduce the number of independent variables, the inner fillet radius ( $r$ ) has been taken equal to the same fraction of the thickness of the vessel wall, as it is in the given geometry. This is in accordance with the thumb rule of design of pressure vessels [32] to take the inner fillet radius as some fraction of the thickness of the vessel wall.

Now, these four geometrical parameters have been combined into three dimensionless groups in the following manner, there by reducing the number of independent geometrical variables to three:

$$\frac{d}{D}, \frac{t}{T}, \frac{D}{T}$$

The above choice of dimensionless groups has been guided by the work of Mohamed and Schroeder [9], wherein, approximate empirical formula for SIF of nozzle-corner cracks has been

given in terms of the groups  $\frac{d}{D}$  and  $\frac{t}{T}$ . The group  $\frac{D}{T}$  has been added to the set for the sake of completeness, since, four independent variables can at most be reduced to three independent dimensionless groups.

The crack parameters are: crack depth ( $a$ ) and aspect ratio ( $b/a$ ). The crack depth is normalized with respect to the thickness of the vessel wall as:  $\frac{a}{T}$ .

The SIF has been normalized with respect to the internal pressure ( $P$ ), and the average crack length,  $\bar{a} \left( = \frac{a+b}{2} \right)$ , as:  $\frac{K_I}{P\sqrt{\pi\bar{a}}}$ .

#### 4.10.2 Discussion

In Figures 4.34–4.40, variation of SIF has been plotted with one parameter at a time, keeping all others constant. Figure 4.34 shows the effect of crack aspect ratio on the variation of SIF over the crack profile. Three important conclusions can be clearly drawn from the Figure. Firstly, the average SIF considerably reduces, as the crack becomes more and more elliptical, i.e. as the aspect ratio is reduced from unity. Secondly, the percentage variation of SIF from the mean value reduces considerably as the aspect ratio decreases. That is, the variation of SIF becomes more and more uniform. Thirdly, the point of minimum SIF shifts towards the nozzle side as the aspect ratio decreases.

Figure 4.35 shows the variation of normalized SIF over crack profiles for different aspect ratios. It is seen that the normalized SIF plots for different aspect ratios are closer to each other as compared to the SIF plots for different aspect ratios (Figure 4.34). Interestingly and fortunately, it so happens that the normalized average SIF remains almost constant with respect to aspect ratio, as shown in Figure 4.36. This means that the variation of normalized average SIF with respect to any other parameter will not depend on the value of aspect ratio.

Normalized average SIF has been plotted against the normalized crack depth in Figure 4.37 for a given Geometry. The decreasing nature of the curve has been verified from the literature [9].

Figure 4.38 shows the variation of normalized average SIF with respect to  $d/D$ . The increasing trend of the curve is expected, since, a larger  $d/D$  ratio signifies a more severe discontinuity in the vessel.

Variation of normalized average SIF has been plotted against the ratio  $t/T$  in Figure 4.39. Figure 4.40 shows the variation of normalized average SIF with respect to the ratio  $D/T$ . The increase in normalized average SIF with increase in  $D/T$  is expected, due to the fact that the hoop stresses in the vessel increase with the increase in  $D/T$  (this can be verified from Lamé's thick cylinder formula). The almost linear nature of the curve may also be attributed to the almost linear dependency of the hoop stresses on the ratio  $D/T$  (this can also be shown using the Lamé's thick cylinder formula).

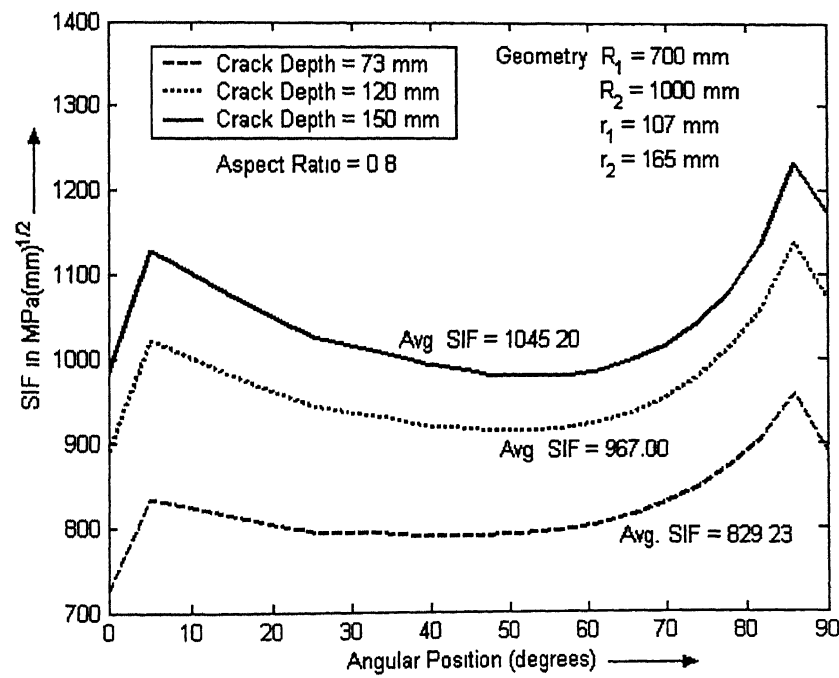
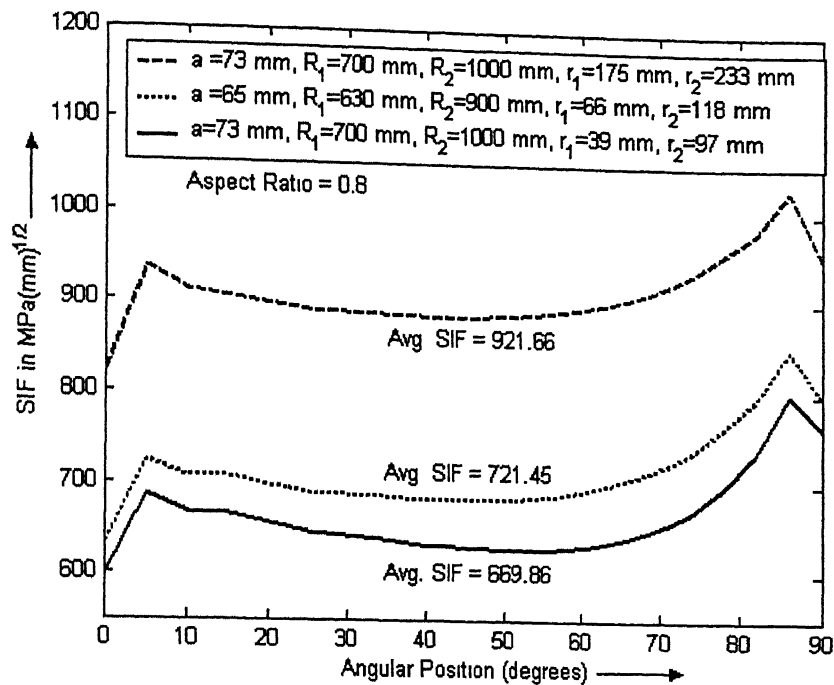
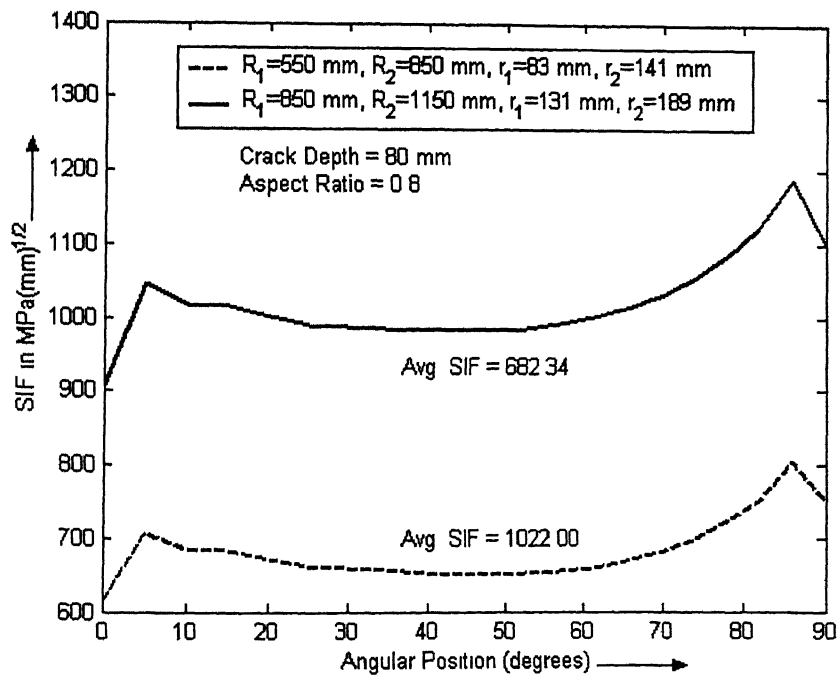


Figure 4.30 Variation of SIF along the profiles of cracks with different depths for the given Geometry.





**Figure 4.31 Variation of SIF along the profiles of cracks with different depths for three different Geometries.**



**Figure 4.32 Variation of SIF along the profile of an 80 mm deep crack for two different Geometries.**

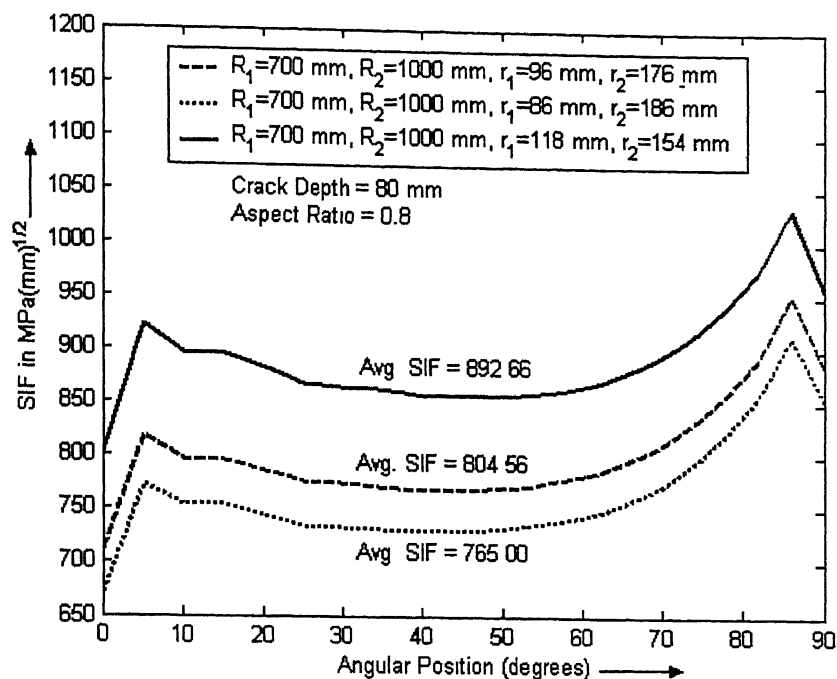


Figure 4.33 Variation of SIF along the profile of an 80 mm deep crack for three different Geometries.

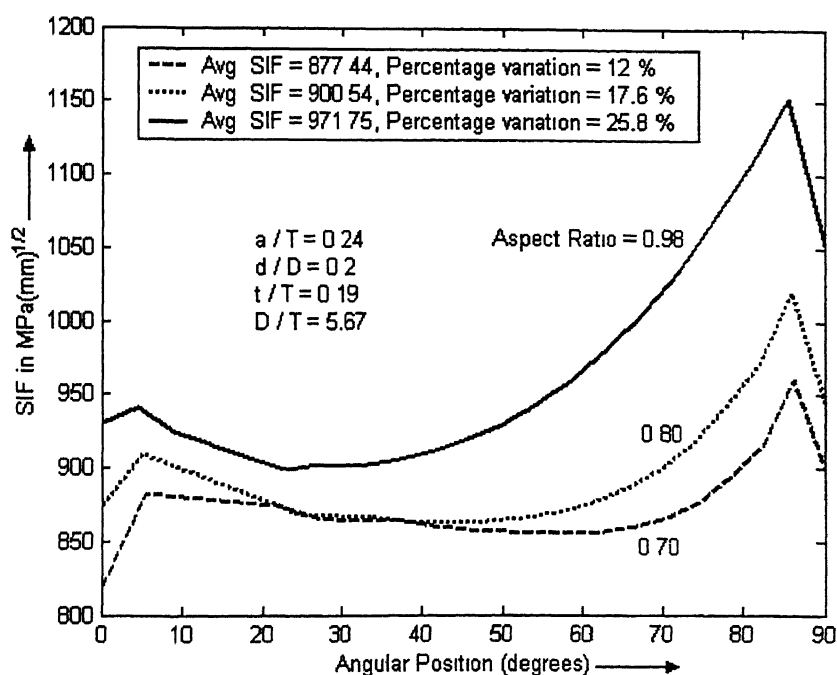


Figure 4.34 Variation of SIF along the profiles of cracks with a given depth for three different aspect ratios.

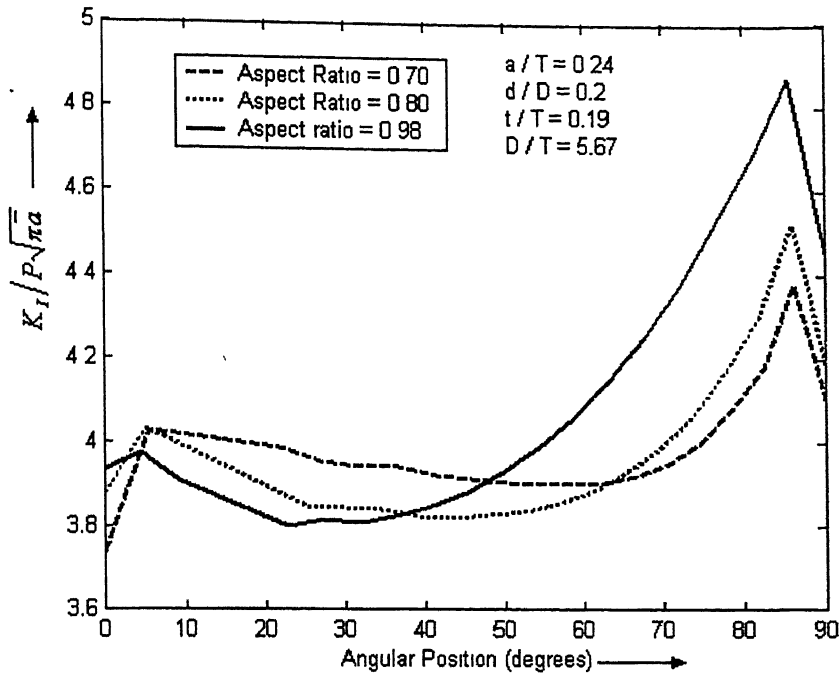


Figure 4.35 Variation of normalized SIF along the profiles of cracks with a given depth for three different aspect ratios.

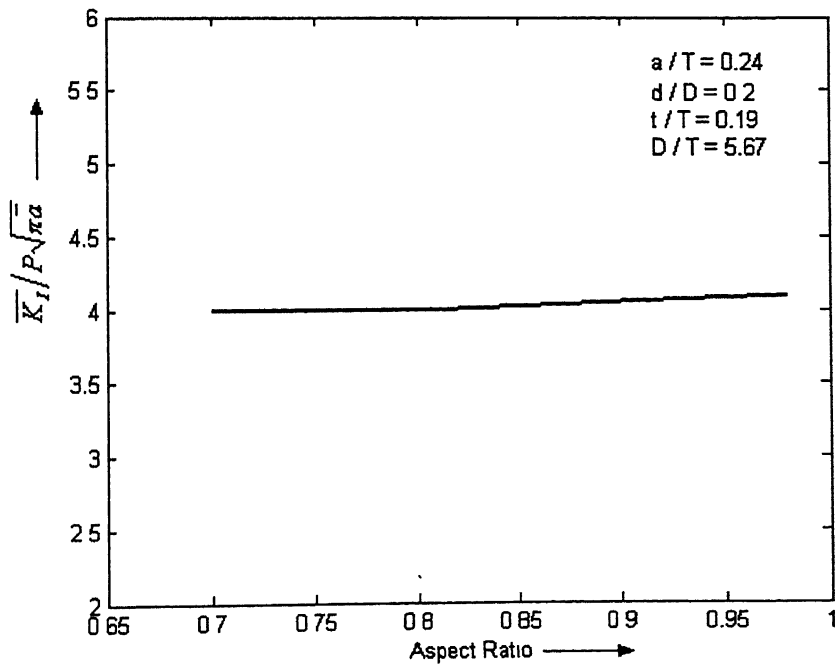


Figure 4.36 Variation of normalized average SIF with respect to crack aspect ratio for a given Geometry and crack depth.

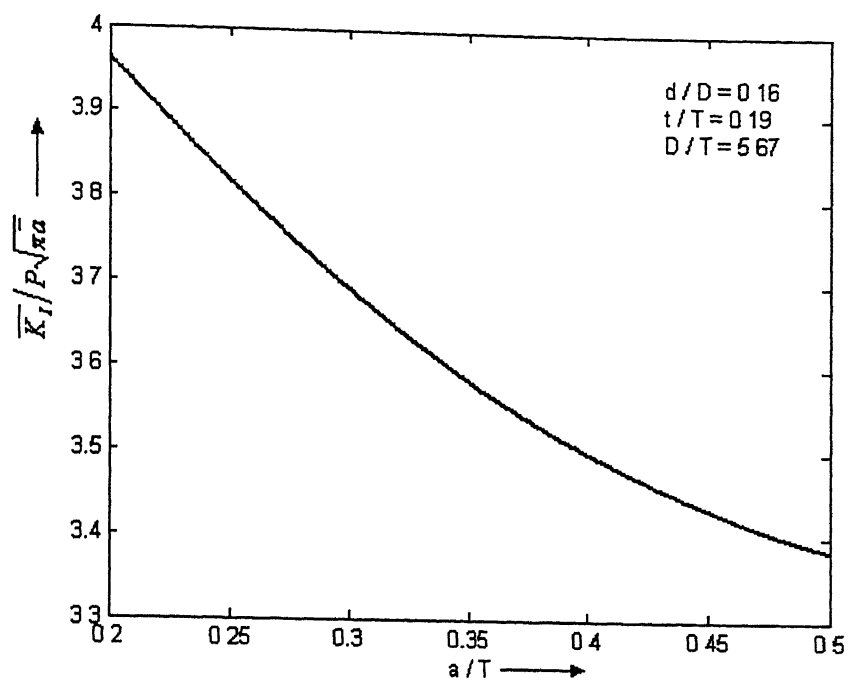


Figure 4.37 Variation of normalized average SIF with respect to normalized crack depth for a given Geometry.

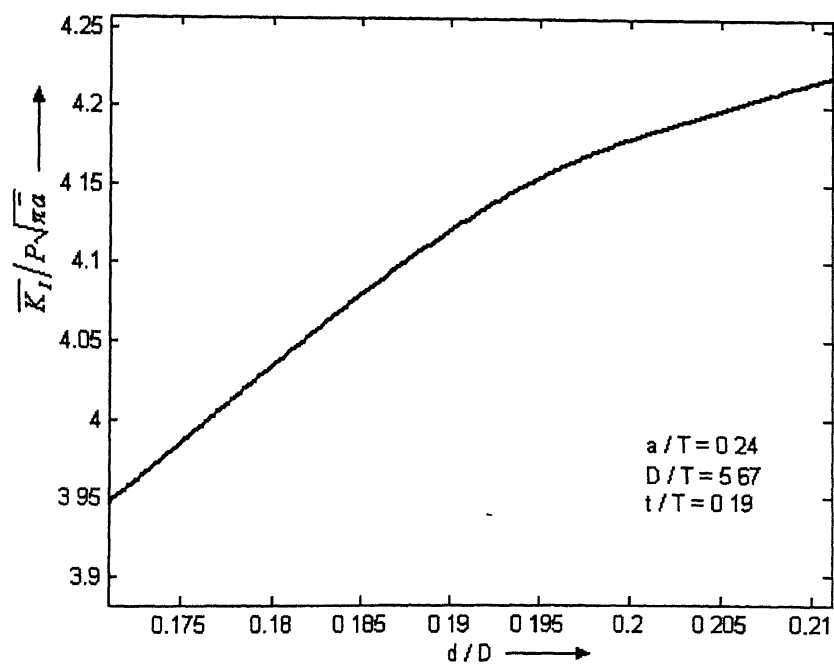


Figure 4.38 Variation of normalized average SIF with respect to  $d/D$ .

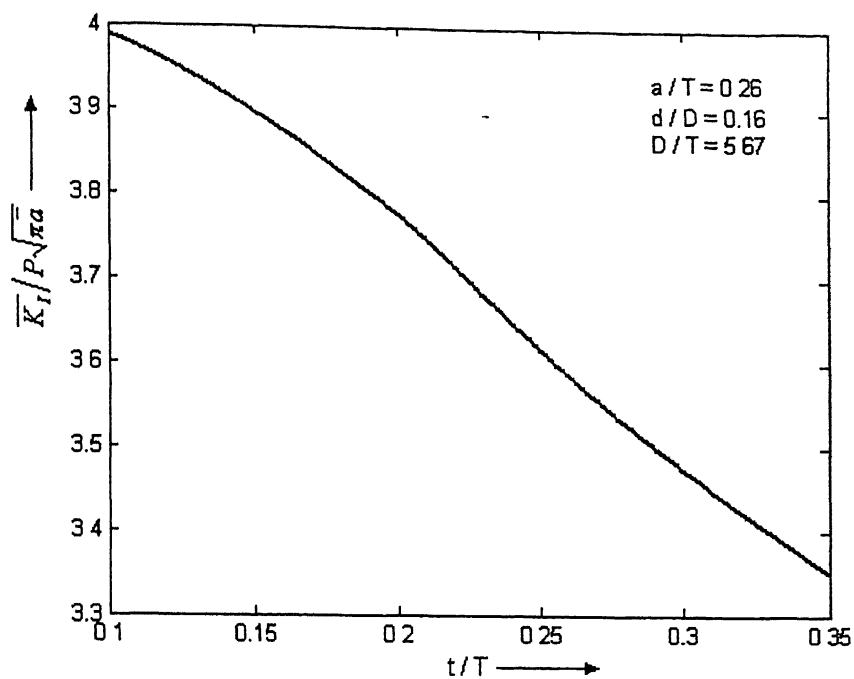


Figure 4.39 Variation of normalized average SIF with respect to  $t/T$ .

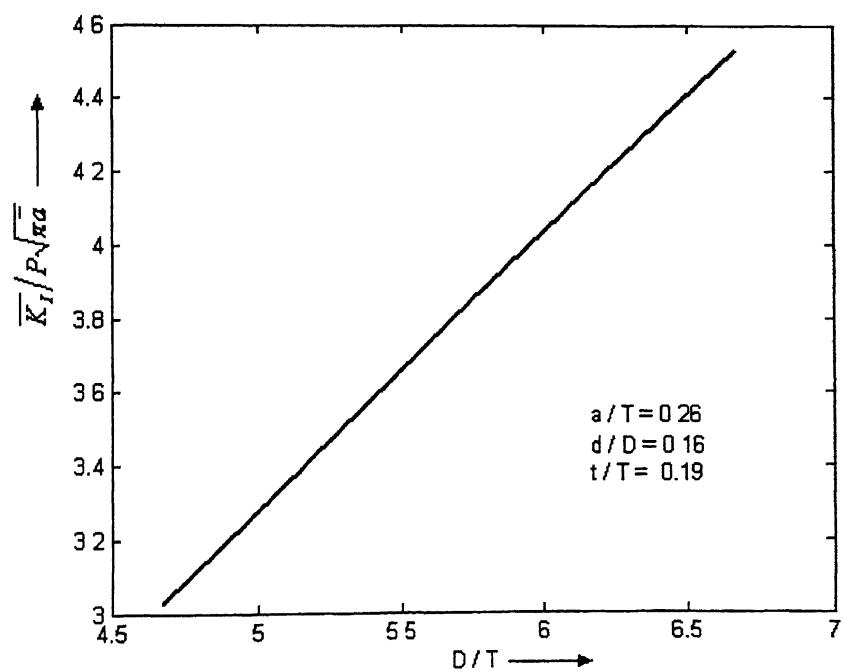


Figure 4.40 Variation of normalized average SIF with respect to  $D/T$ .

## **4.11 Closure**

Stress analysis of the nozzle-vessel intersection with corner crack has been performed using singular elements near the crack. Stress Intensity Factors have been evaluated along the crack profile and the methodology adopted has been verified. Finally, parametric study has been performed to understand the effect of different parameters on the SIF.

The SIF of nozzle-corner cracks has been found to bear simple relationships with most of the parameters individually, indicating the possibility of development of more accurate empirical relations for its calculation, as compared to those already available in the literature.

## **Chapter 5**

# **EFFECT OF LOCA ON NOZZLE-CORNER CRACKS**

### **5.1 Introduction**

As already introduced in section 1.1, LOCA refers to a loss of coolant accident in a nuclear reactor plant. Fracture failure of reactor pressure vessel may occur during a LOCA if the prevailing circumstances are adverse. Three conditions are necessary for such an incident to occur:

- 1) A large upward shift in the nil ductility transition (NDT) temperature due to a combination of nuclear irradiation during service and the presence of high copper and nickel content in the vessel welds.
- 2) The existence of an initial flaw on the inner surface of the vessel.
- 3) A severe over-cooling transient caused by the splashing of cold water on the inner surface of the vessel by the emergency core cooling system during a LOCA.

The over-cooling transient involves a sharp change in the temperature of the inner surface of the vessel. Simultaneously, the internal pressure would be expected to fall from the operating pressure to the atmospheric pressure. This typical thermal load is termed as “Thermal Shock” in the nuclear industry. If the pressure remains high during the transient, or falls off slowly, the event is termed as “Pressurized Thermal Shock” (PTS).

Sudden cooling of the inner surface of the vessel causes sudden contraction of the inner layers, but the outer layers contract slowly. This produces high tensile stresses in the hoop direction on the inner side of the vessel (and nozzle). Hence, a flaw existing at the inner side of the vessel (or nozzle-vessel corner) with an orientation which causes hoop stress to load it in mode I, can be severely affected.

Albeit, LOCAs have occurred during reactor operation, for instance, the Three Mile Island II, because all three of the conditions mentioned above were not simultaneously satisfied, no catastrophic fractures of nuclear plant pressure vessels have been experienced.

Nonetheless, the problem is clearly significant and must be given special attention.

## 5.2 Problem Definition

The present intention is to study the effect of a given PTS transient on a quarter-elliptical corner crack existing at the crotch region of the given nozzle-vessel intersection. Since the temperature of the inner surface of the vessel and the nozzle will vary with time during the transient, the temperature distribution in the wall of the nozzle-vessel intersection will be a function of time. Moreover, internal pressure is also time-varying. This causes time-varying thermal and mechanical stresses and, in turn, time-varying stress intensity factors.

It is intended to study the variation with time, of SIF along the crack front during the given PTS transient, and compare the SIF values with the material fracture toughness for crack initiation to estimate whether the crack becomes critical or not. Also, it is intended to identify the most critical time, and location on the crack front.

The geometry of the nozzle-vessel intersection considered here is the same as specified in section 3.1. The crack considered is characterized by:

$$\text{Crack Depth, } a/T = 0.5$$

$$\text{Aspect Ratio, } b/a = 0.8$$

The PTS transient is given as a thermal and mechanical load history on the inner surface of the vessel and the nozzle, as tabulated in Table 5.1 and also shown graphically in Figure 5.1.



Time (s)	Temperature ( $^{\circ}\text{C}$ )	Pressure (bar)
0	310	170
50	230	150
1500	60	6
8000	60	6

**Table 5.1 Given PTS transient.**

The table (and the figure) specifies the value of temperature at the inner surface of the vessel and the nozzle, and the magnitude of the internal pressure at different time points. The intermediate values will be obtained by linear interpolation. The transient is of duration of 1500 s (25 minutes) only, but the load history is given up to 8000 s (about 2 Hrs. and 15 minutes). This is done to reach as close to the steady state as possible, after the PTS.

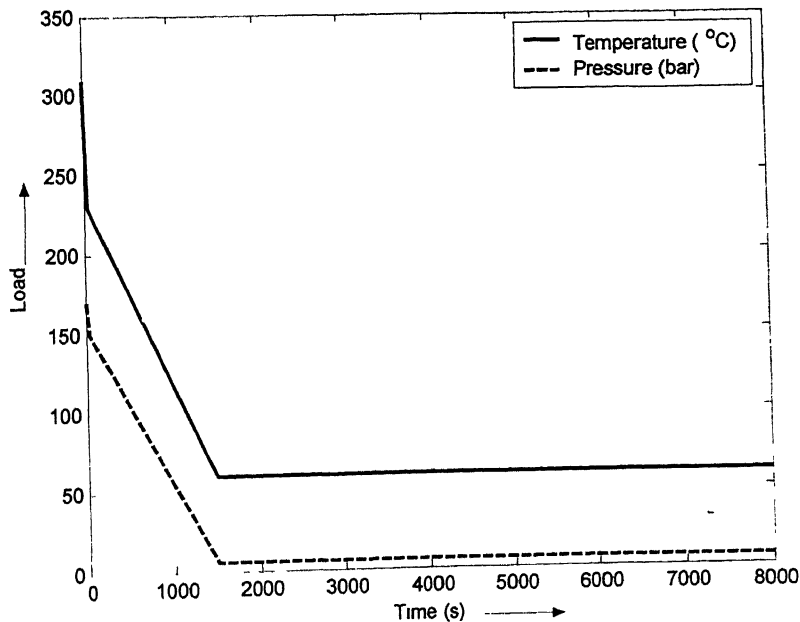


**Figure 5.1 Given PTS transient.**

### 5.3 FE Modeling and Analysis

ANSYS 5.4 has been used to perform the transient thermal-stress analysis of the nozzle-vessel intersection with corner crack. The geometry has been modeled along with crack and is meshed with 18729 elements comprising of 1254 hexahedral elements, and 17475 tetrahedral and transition elements. The total number of nodes in the mesh is 32318. Two layers of hexahedral elements have been used on either side of the crack front with 20 elements along the crack front.

First, a static heat transfer analysis is done to obtain the temperature distribution existing at time,  $t = 0$ , which represents the normal operating condition of the vessel. Then, a transient heat transfer analysis has been performed over the entire time domain of 8000 s, to obtain the temperature distribution at a number of time points.

The given transient temperatures are specified on the inner surface of the vessel and the nozzle. Convective boundary condition is specified on the outer surface of both the cylinders. The convective film heat transfer coefficient at the outer surface of a cylinder has been taken from the Heat and Mass Transfer Data Book by Kothandaraman and Subramanyan [33] and is given as:

$$h = 1.31(\Delta T^{0.333}) \text{ (in } W/m^2 K \text{)}, \quad (5.1)$$

for a turbulent boundary layer, where,  $\Delta T$  is the difference between the temperature of the surface and the bulk temperature. Turbulent boundary layer is chosen because for a laminar boundary layer, the heat transfer coefficient also depends upon the dimensions of the cylinder, whereas it is intended to use some uniform reference value for both the cylinders. Equation 5.1 is valid for a vertical cylinder and there is a different relation prescribed for a horizontal cylinder, but the difference is not much. Also,  $h$  is not a very strong function of  $\Delta T$ . In lieu of the above,  $h$  is calculated from Equation 5.1 for an assumed average value of  $\Delta T$  equal to  $150^\circ C$  (an atmospheric temperature of  $25^\circ C$  is assumed). This value ( $\approx 7 W/m^2 K$ ), is used as the average heat transfer coefficient for the outer surfaces of the vessel and the nozzle. All the other surfaces of the structure are assumed to be insulated.

A total of 15 time points are chosen among those at which temperature distributions have been determined. The immediate layer of elements on either side of the crack front is made

singular by shifting the mid nodes adjacent to the crack tip nodes, to quarter point locations. Stress analysis has then been performed at each of the 15 time points chosen.

The internal pressure calculated by linear interpolation at the respective time is applied on the inner surfaces of both the cylinders and also on the crack face. The displacement and traction boundary conditions used are similar to those described in section 3.3.1.

The material properties used in the analyses are taken from Table 3.2 at  $100^{\circ}\text{C}$  assuming that it represents an average temperature during the transient. The other properties used in the analyses are: Poisson's ratio,  $\nu = 0.3$ , and density,  $\rho = 7833 \text{ Kg/m}^3$ .

Finally, SIF values have been evaluated (using the plane strain relations throughout the crack profile) along the crack front, for each of the 15 time points for which stress analyses have been performed.

## 5.4 Results and Discussion

The variation of temperature along the crack front has been plotted for different time points in Figures 5.2-5.4. As seen in Figure 5.2, the temperature along the crack front is almost constant at time  $t = 0 \text{ s}$ . With the outbreak of the transient, the temperatures at the end points (angular positions of  $0^{\circ}$  and  $90^{\circ}$ ) of the crack front (which correspond to the intersection of the crack front with the inner surfaces of the vessel and the nozzle respectively), drop sharply, as seen in the plots for time  $t = 23 \text{ s}$  and  $t = 50 \text{ s}$  in Figure 5.2, whereas, the response of the points away from the end points is slower. Except for a few initial seconds, the temperatures at the end points are lower and increase towards the middle. At all times, the maximum temperature along the crack front occurs at around  $50^{\circ}$ .

The variation of SIF along the crack front has been plotted for different time points in Figures 5.5-5.7, along with the material fracture toughness for crack initiation (Critical Stress Intensity Factor,  $K_{Ic}$ ). The Critical Stress Intensity Factor for crack initiation for the material of the structure has been taken from ASME, Section XI, Appendix A [18], which gives a lower bound test data for  $K_{Ic}$  as a function of temperature, as:

$$K_{Ic} = 33.2 + 2.81 \exp\{0.02(T - RT_{NDT} + 100)\} \quad (\text{in } ksi\sqrt{in}), \quad (5.2)$$

subject to a maximum of  $200 ksi\sqrt{in}$ , where,  $T$  is the temperature (in  $^{\circ}F$ ), and  $RT_{NDT}$  is the reference NDT temperature (in  $^{\circ}F$ ).

In the present analysis,  $RT_{NDT}$  has been taken equal to  $0^{\circ}C$ . Equation 5.2 attains the maximum value of  $200 ksi\sqrt{in}$  at about  $55^{\circ}C$  for this value of  $RT_{NDT}$ , whereas the minimum temperature in the present analysis is  $60^{\circ}C$ . Hence, the value of  $K_{Ic}$  has been taken equal to  $200 ksi\sqrt{in}$  ( $\approx 220 MPa\sqrt{m} \approx 6950 MPa\sqrt{mm}$ ) throughout the present analysis.

Figure 5.5 shows that the SIF along the crack front is increasing with time, as expected. Initially, the SIF is higher towards the nozzle side (angular position =  $90^{\circ}$ ), but as the PTS outbreaks, the SIF towards the vessel side (angular position =  $0^{\circ}$ ) starts rising at a rate faster than that of the nozzle side. The SIF towards the middle of the crack front take still longer time to build up. The vessel side SIF soon becomes equal to the nozzle side SIF (at around  $t = 50$  s) and surpasses it. It may be observed from Figure 5.6, that the point of minimum SIF is continuously shifting towards the nozzle side, as the time passes.

The SIF keeps on increasing and finally reaches the peak at time,  $t = 1500$  s (25 minutes), when it can be seen in Figure 5.7, that a small portion of the crack front (between angular positions of  $0^{\circ}$  and  $6^{\circ}$ ) near the vessel side has become critical (SIF value has exceeded  $K_{Ic}$ ). After  $t = 1500$  s, the SIF begins to fall off throughout the crack front.

Figures 5.8-5.10 show the variation of vessel side SIF, nozzle side SIF, and the average SIF over the crack front, with time, respectively. It may be observed from these Figures that the initial rate of rise of SIF is very high in all the three cases, but fall off continuously. The rate falls off more rapidly for the nozzle side SIF than for the vessel side SIF. After reaching the peak values, the SIF decay at an average rate much lower than the average rate of increase. The steady state is not reached even after 8000 s.

It is apparent from Figure 5.8, that the crack front (towards the vessel side) is critical for a period of about 420 s (7 minutes), from time,  $t = 1340$  s to  $t = 1760$  s. The crack may or may not fail during this period, depending upon the degree of conservatism involved in the value of  $K_{Ic}$ , and various other factors.

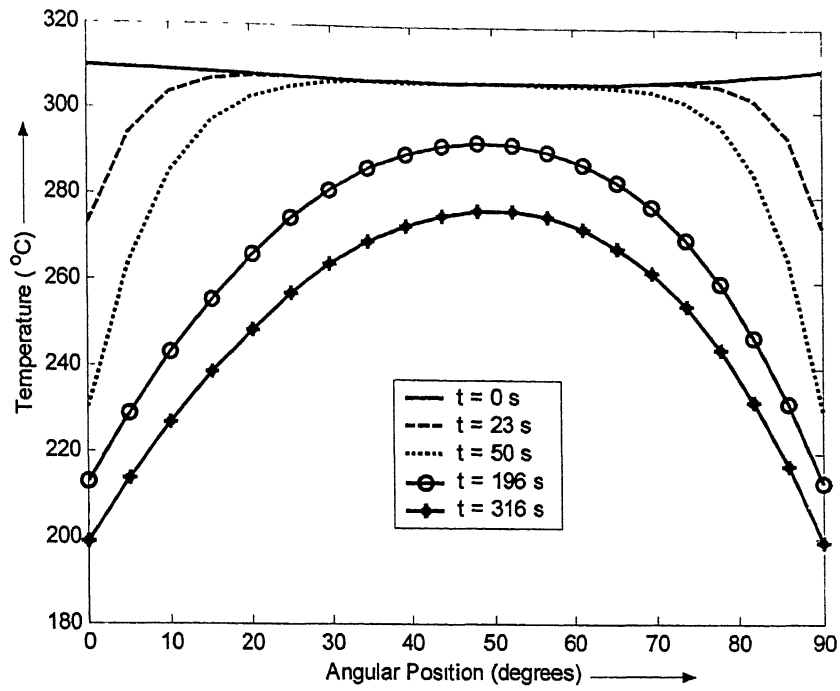


Figure 5.2 Variation of temperature along the crack front (Time points 1-5).

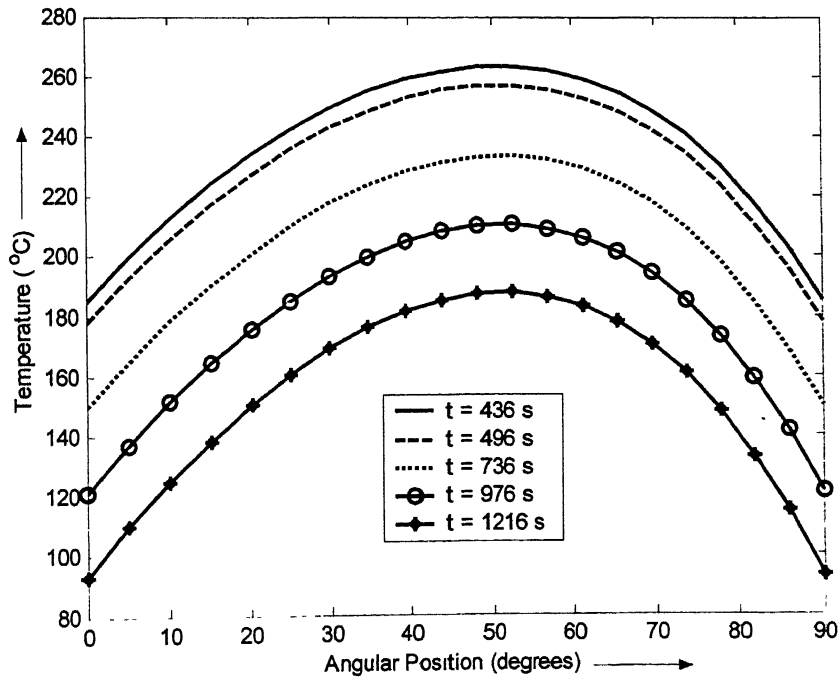


Figure 5.3 Variation of temperature along the crack front (Time points 6-10).

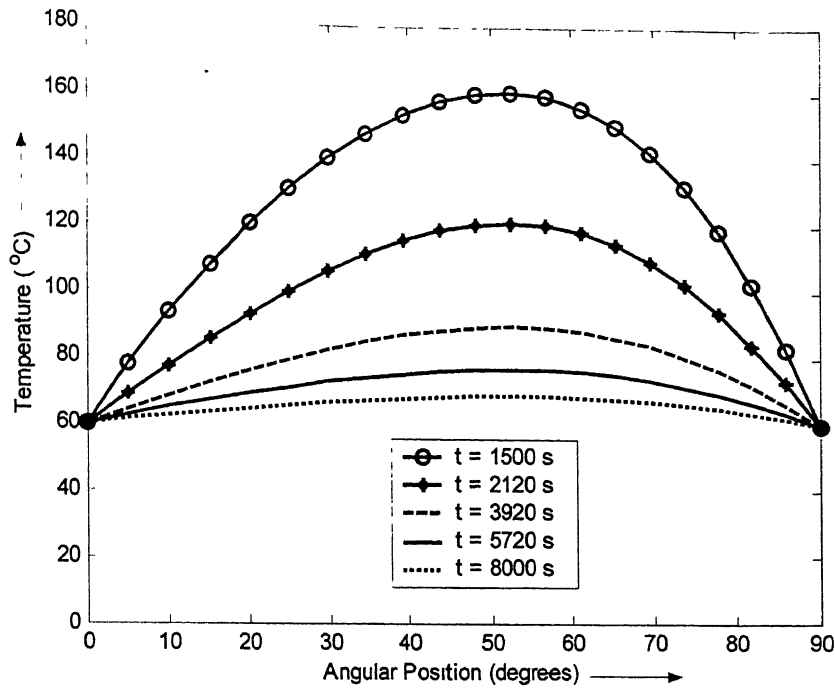


Figure 5.4 Variation of temperature along the crack front (Time points 11-15).

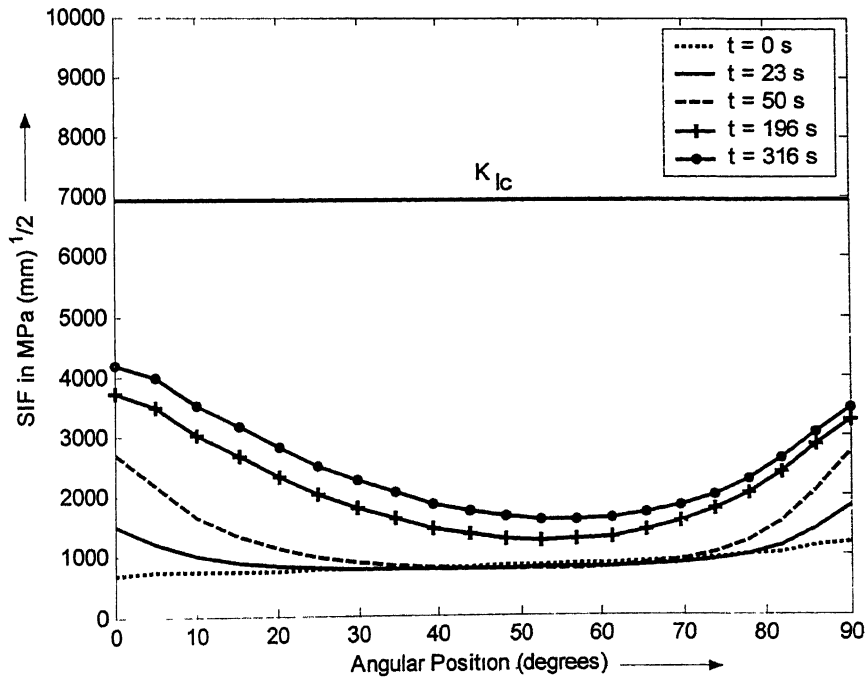


Figure 5.5 Variation of SIF along the crack front (Time points 1-5).

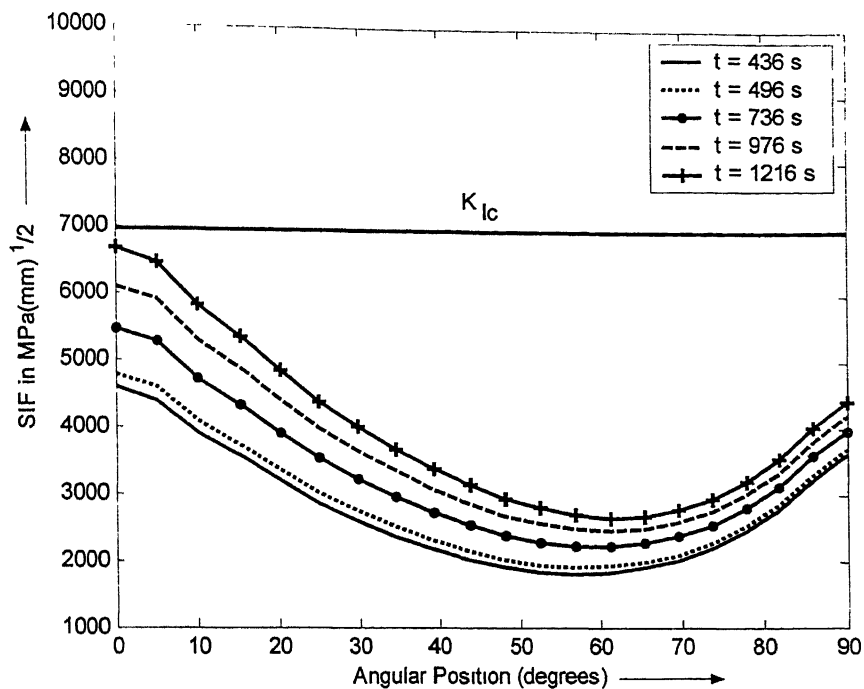


Figure 5.6 Variation of SIF along the crack front (Time points 6-10).

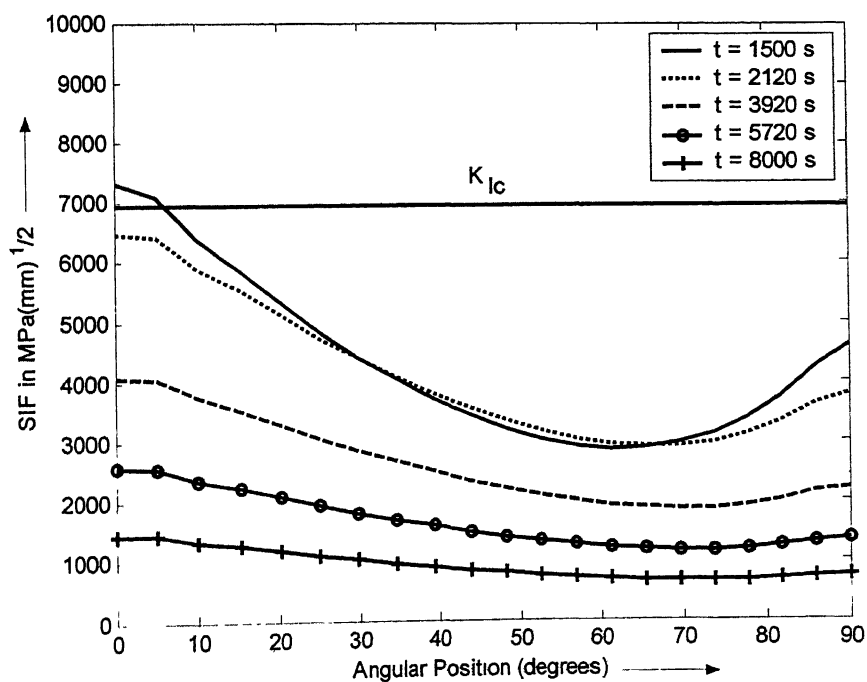


Figure 5.7 Variation of SIF along the crack front (Time points 11-15).

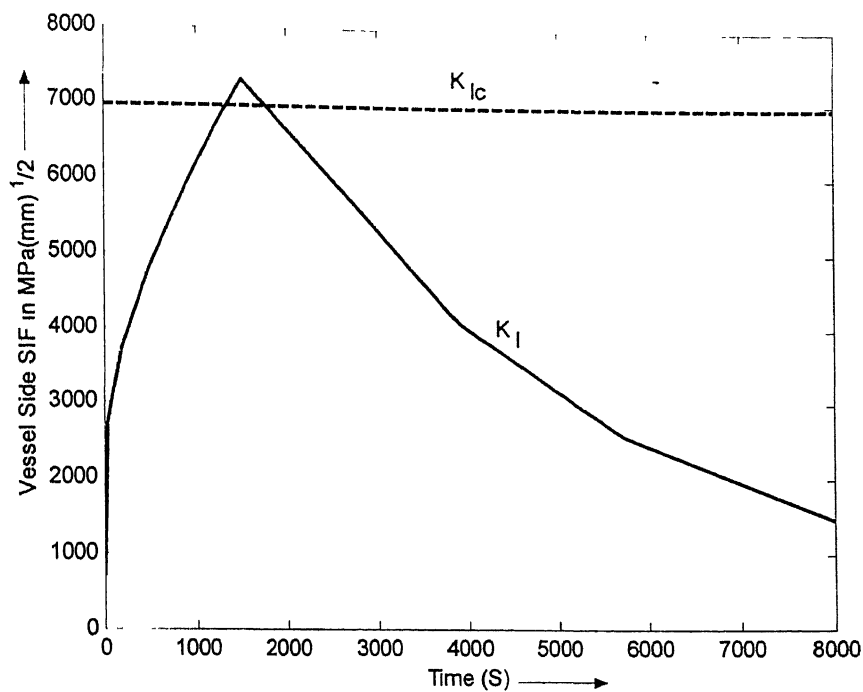


Figure 5.7 Variation of vessel side SIF with time.

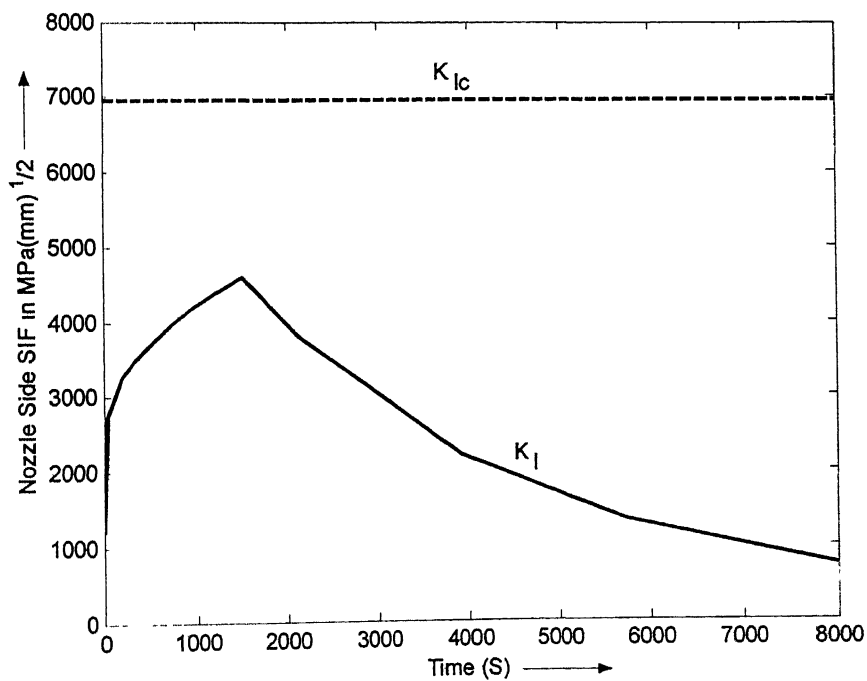


Figure 5.8 Variation of nozzle side SIF with time.



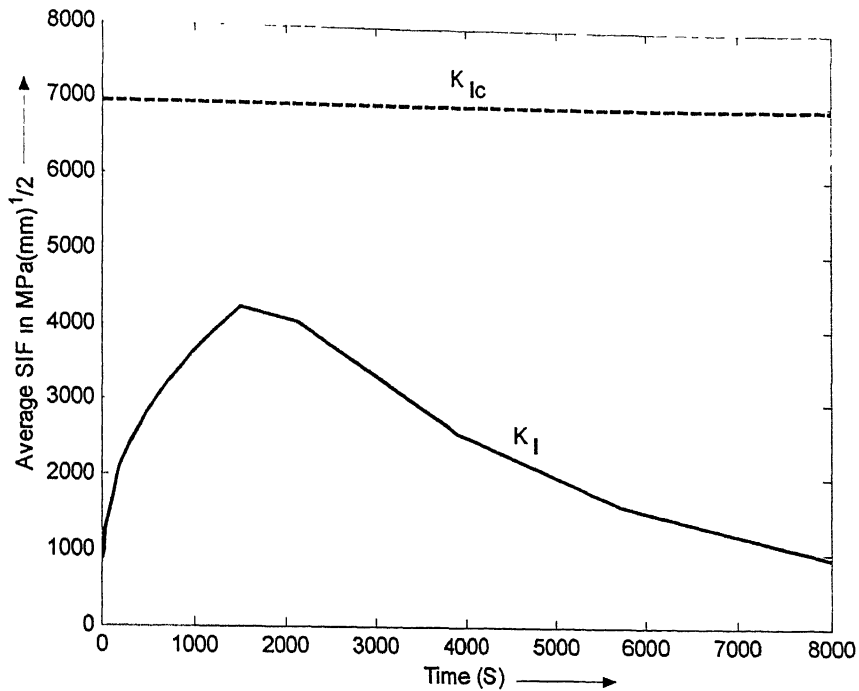


Figure 5.9 Variation of average SIF with time.

## 5.5 Closure

Thermal-stress analysis of the nozzle-vessel intersection with a corner crack has been performed to study the effect of a LOCA on nozzle-corner cracks. A PTS appears to be much more crucial than a normal pressure loading. The considered crack configuration seems to be unsafe, with a small portion of the crack becoming critical for a small duration of time during the PTS considered. The vessel side of the crack front has been identified to be the most critical location during a PTS, unlike a normal pressure loading, during which, the nozzle side has a higher value of SIF. This suggests that apparently there is no possibility of Leak-before-break during a PTS (as far as nozzle-corner cracks are concerned). However, the possibility of crack arrest needs to be assessed.

## Chapter 6

# ESTIMATION OF STABLE CRACK GROWTH

### 6.1 Introduction

In the previous chapters, it has been attempted to estimate whether a crack is critical or not under a given set of loading conditions. When a crack becomes critical, the component becomes susceptible to catastrophic failure, but the crack growth takes place in a stable manner much before the crack becomes critical. Thus, to ensure a safe operation, it is important to estimate the amount of stable crack growth during a given load cycle, so that the safe life of the component may be accurately predicted, by estimating the number of load cycles required to grow the crack to a critical size.

This chapter is an attempt towards the estimation of stable crack growth in a nozzle-corner crack using the cohesive zone technique. It is a numerical technique in which, the surface along which the growth of crack is expected, is modeled as a cohesive zone with a different material constitutive relation which is capable of simulating the softening, and ultimately failure, of the material. The formulation of the cohesive zone model is such that it can be conveniently implemented in a general purpose FE code through a user subroutine. The use of a cohesive zone model is inviting because the solution may be treated as a non-linear boundary value problem with a time dependent boundary without recourse to a crack growth criterion.

The formulation of a 3D cohesive zone model, given by Foulk et al. [34] has been presented. The method is applied to a Double Cantilever Beam (DCB) specimen and a nozzle-corner crack and the results of crack growth analyses have been presented.

## 6.2 Constitution of the Cohesive Zone

Cohesive zone models are employed to predict new surface areas evolving in a body,  $\beta$  as shown in Figure 6.1. By using constitutive models that are non-convex, it is possible to predict the creation of new surface area along any predetermined plane during the evolution of the problem.

The constitution of a cohesive zone that is neither history dependent nor rate dependent is assumed to be of the following form [35]:

$$T_p = \alpha_p \left( \frac{27}{4} \right) \sigma_{max} \left( \frac{[u_p]}{\delta_p} \right) (1 - 2\lambda + \lambda^2), \quad (6.1)$$

$$T_n = \left( \frac{27}{4} \right) \sigma_{max} \left( \frac{[u_n]}{\delta_n} \right) (1 - 2\lambda + \lambda^2), \quad (6.2)$$

$$T_s = \alpha_s \left( \frac{27}{4} \right) \sigma_{max} \left( \frac{[u_s]}{\delta_s} \right) (1 - 2\lambda + \lambda^2), \quad (6.3)$$

where, the traction components,  $T_n, T_p$  and  $T_s$  are coupled to both normal and tangential crack opening displacements,  $[u_n]$ ,  $[u_p]$  and  $[u_s]$  respectively. Also,  $\sigma_{max}$  is a material property of the cohesive zone that is a measure of bond strength, and  $\lambda$  is the normalized quantity coupling normal and tangential behavior:

$$\sqrt{\left( \frac{[u_n]}{\delta_n} \right)^2 + \left( \frac{[u_p]}{\delta_p} \right)^2 + \left( \frac{[u_s]}{\delta_s} \right)^2}, \quad (6.4)$$

where,  $\delta_n$ ,  $\delta_p$  and  $\delta_s$  are material properties that are length scales associated with debonding, and  $\alpha_p$  and  $\alpha_s$  are material properties relating shear to normal strength. It is furthermore assumed that the cohesive zone is fully debonded when  $\lambda \geq 1$ , so that in this case  $T_p = T_n = T_s = 0$ . It is to be noted that the displacement field is transformed to the local coordinate system shown in Fig 6.2.

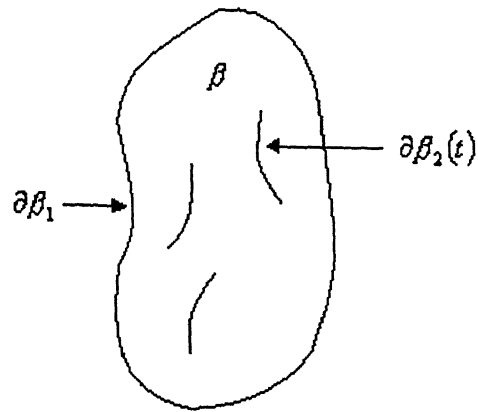


**Figure 6.1** Solid body with fixed and moving boundaries (cracks).

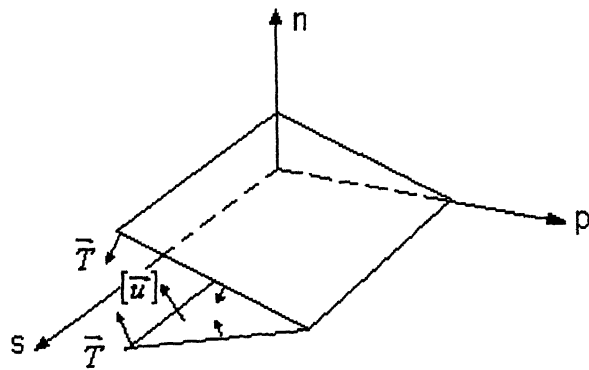


**Figure 6.2** Local coordinate system defined for each element.

$T_n$  is depicted graphically in Fig 6.3 for the case of normal separation. In this case the maximum,  $\sigma_{\max}$ , is reached when  $\lambda = 1/3$ . If the cohesive zone is loaded beyond  $\lambda = 1/3$  and unloaded, the Tvergaard model will yield an increasing traction for a decreasing displacement. Because this is not physically realistic, the amended model as described by Tvergaard [35] is used. If  $\lambda > 1/3$  and  $\dot{\lambda} < 0$ , the following traction relationships are assumed to hold good:

$$T_p = \alpha_p \left( \frac{27}{4} \right) \sigma_{\max} \left( \frac{[u_p]}{\delta_p} \right) (1 - 2\lambda + \lambda^2) \quad (6.5)$$

$$T_n = \left( \frac{27}{4} \right) \sigma_{\max} \left( \frac{[u_n]}{\delta_n} \right) (1 - 2\lambda + \lambda^2) \quad (6.6)$$

$$T_s = \alpha_s \left( \frac{27}{4} \right) \sigma_{\max} \left( \frac{[u_s]}{\delta_s} \right) (1 - 2\lambda + \lambda^2) \quad (6.7)$$

where  $\lambda_{\max}$  is the maximum value of  $\lambda$  before unloading. These relations remain valid until  $\lambda > \lambda_{\max}$  (reloading).

## 6.3 Finite element Formulation

The finite element formulation utilized herein is semidiscretized in that the displacement is modeled using shape functions that do not vary with time, whereas the time dependence in the problem is accounted for by using a finite difference (forward Euler scheme) approximation in time. Nonlinearity can be accounted for by a variety of iterative techniques. Herein, it is assumed that the Newton-Raphson method is used.

### 6.3.1 Variational form of the boundary value problem

The principle of virtual work applied to the body  $\beta$  for a variation  $\delta u$ , in displacement, yields:

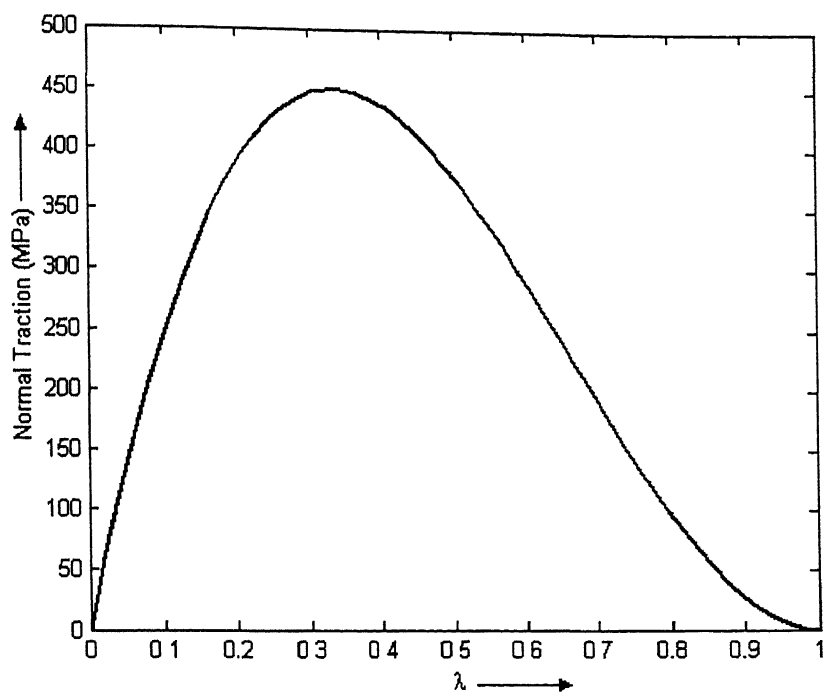


Figure 6.3 Traction-displacement relation for a pure normal separation.

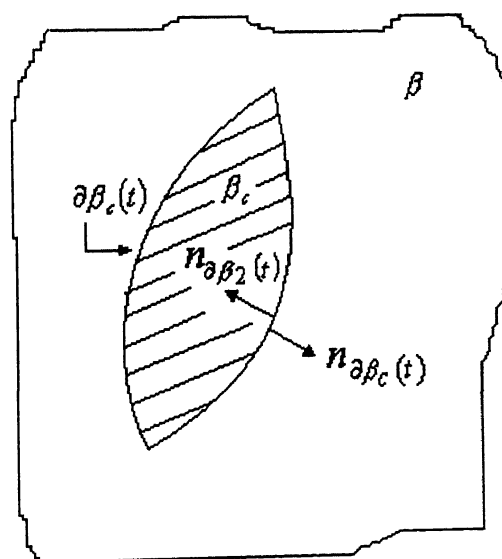


Figure 6.4 Separation of Cohesive zone from the bulk material.

$$\int_{\beta} \sigma_{,i} \delta u_i dV = 0. \quad (6.8)$$

Applying the divergence theorem to the above equation results in:

$$\int_{\beta} \sigma_{,ij} (t + \Delta t) \delta \varepsilon_{ij} (t + \Delta t) dV = \int_{\partial\beta_1} T_i (t + \Delta t) \delta u_i (t + \Delta t) dS + \int_{\partial\beta_2(t)} T_i (t + \Delta t) \delta u_i (t + \Delta t) dS, \quad (6.9)$$

where,  $t + \Delta t$  is the time of interest. Now defining the following terms:

$$\Delta T \equiv T_i (t + \Delta t) - T_i (t), \quad (6.10)$$

$$\Delta u_i \equiv u_i (t + \Delta t) - u_i (t), \quad (6.11)$$

$$\Delta \sigma_{ij} \equiv \sigma_{ij} (t + \Delta t) - \sigma_{ij} (t), \quad (6.12)$$

$$\Delta \varepsilon_{ij} \equiv \varepsilon_{ij} (t + \Delta t) - \varepsilon_{ij} (t). \quad (6.13)$$

Substituting Equations 6.10-6.13 into Equation 6.9 results in the following:

$$- \int_{\partial\beta_2(t)} \Delta T_i \delta \Delta u_i dS + \int_{\beta} \Delta \sigma_{ij} \delta \Delta \varepsilon_{ij} dV = \int_{\partial\beta_1} T_i (t + \Delta t) \delta \Delta u_i dS + \int_{\partial\beta_2(t)} T_i (t) \delta (\Delta u_i) dS - \int_{\beta} \sigma_{ij} (t) \delta \Delta \varepsilon_{ij} dV. \quad (6.14)$$

Equation 6.14 represents the virtual work for a general body with initial and time dependant boundaries. Rather than applying this formulation directly to a finite element, a separation is considered (as shown in Figure 6.4) between the body  $\beta$  and the boundary  $\partial\beta_2(t)$ , and the cohesive zone,  $\beta_c$ , with boundary  $\partial\beta_c(t)$ . This separation yields:

$$\partial\beta_c(t) = \partial\beta_2(t), \quad (6.15)$$

$$n_{\beta_c(t)} = -n_{\beta_2(t)}, \quad (6.16)$$

$$T_i (n_{\beta_c(t)}) = -T_i (n_{\beta_2(t)}). \quad (6.17)$$

Thus, writing the incrementalized principle of virtual work for a cohesive zone results in:

$$\int_{\partial\beta_c(t)} \Delta T_i \delta \Delta u_i dS + \int_{\beta_c} \Delta \sigma_y \delta \Delta \varepsilon_y dV = - \int_{\partial\beta_c(t)} T_i(t) \delta \Delta u_i dS - \int_{\beta_c} \sigma_y(t) \delta \Delta \varepsilon_y dV. \quad (6.18)$$

Assuming that the cohesive zone has no volume in the initial undeformed state and is completely described by boundary tractions, Equation 6.18 reduces to

$$\int_{\partial\beta_c(t)} \Delta T_i \delta \Delta u_i dS = - \int_{\partial\beta_c(t)} T_i(t) \delta \Delta u_i dS. \quad (6.19)$$

The traction-displacement relation may be written in the following incremental form:

$$\Delta T_i = k_y \Delta [u_j] + \Delta T_i^R, \quad (6.20)$$

where the  $\Delta s$  represent changes in the associated quantities during the time step  $\Delta t$ . The last term in the above equation is zero and the terms  $k_y$  can be obtained by differentiating Equations 6.1-6.3 with respect to the displacement jump.

Substituting Equation 6.20 into Equation 6.19 results in the following variational form:

$$\int_{\partial\beta_c(t)} k_y \Delta [u_j] \delta \Delta u_i dS + \int_{\partial\beta_c(t)} \Delta T_i^R \delta \Delta u_i dS = - \int_{\partial\beta_c(t)} T_i(t) \delta \Delta u_i dS, \quad (6.21)$$

where,

$$k_p = \alpha_p \left( \frac{27}{4} \right) \frac{\sigma_{max}}{\delta_p} \left[ (1 - 2\lambda + \lambda^2) + \frac{1}{\lambda} \left( \frac{[u_p]}{\delta_p} \right)^2 (-2 + 2\lambda) \right], \quad (6.22)$$

$$k_n = \left( \frac{27}{4} \right) \frac{\sigma_{max}}{\delta_n} \left[ (1 - 2\lambda + \lambda^2) + \frac{1}{\lambda} \left( \frac{[u_n]}{\delta_n} \right)^2 (-2 + 2\lambda) \right], \quad (6.23)$$

$$k_s = \alpha_s \left( \frac{27}{4} \right) \frac{\sigma_{max}}{\delta_s} \left[ (1 - 2\lambda + \lambda^2) + \frac{1}{\lambda} \left( \frac{[u_s]}{\delta_s} \right)^2 (-2 + 2\lambda) \right]. \quad (6.24)$$



In order to simplify the integration, the surface area of the cohesive zone may be written in terms of an upper and lower surface:

$$\partial\beta_c(t) = \partial\beta_c^u(t) + \partial\beta_c^l(t). \quad (6.25)$$

Rewriting the principle of virtual work for the cohesive zone thus results in

$$\begin{aligned} \int_{\partial\beta_c^u(t)} k_y \Delta[u,] \delta \Delta u, dS + \int_{\partial\beta_c^u(t)} \Delta T_i^R \delta \Delta u, dS + \int_{\partial\beta_c^l(t)} k_y \Delta[u,] \delta \Delta u, dS + \int_{\partial\beta_c^l(t)} \Delta T_i^R \delta \Delta u, dS \\ = - \int_{\partial\beta_c^u(t)} T_i(t) \delta \Delta u, dS - \int_{\partial\beta_c^l(t)} T_i(t) \delta \Delta u, dS. \end{aligned} \quad (6.26)$$

### 6.3.2 Finite element discretization

Equation 6.26 may be discretized in space by writing the displacement field on each surface as a function of the nodal displacements on that surface. The crack opening displacement,  $[u,]$  must be written with respect to each surface. This is derived from the definition of the traction-displacement relationship (in Mode I,  $[u,]$  for the lower surface will be negative). The nodal displacements on upper and lower surface are indicated as  $u_i^\alpha(u)$ , and  $u_i^\alpha(l)$ , respectively. Thus, for the upper surface, it is assumed that:

$$u_i = N^\alpha u_i^\alpha(u), \quad \Delta u_i = N^\alpha \Delta u_i^\alpha(u), \quad (6.27)$$

$$[u_i] = N^\alpha u_i^\alpha(u) - N^\alpha u_i^\alpha(l), \quad \Delta[u_i] = N^\alpha \Delta u_i^\alpha(u) - N^\alpha \Delta u_i^\alpha(l). \quad (6.28)$$

Similarly, for the lower surface, it is assumed that:

$$u_i = N^\alpha u_i^\alpha(l), \quad \Delta u_i = N^\alpha \Delta u_i^\alpha(l), \quad (6.29)$$

$$[u_i] = N^\alpha u_i^\alpha(l) - N^\alpha u_i^\alpha(u), \quad \Delta[u_i] = N^\alpha \Delta u_i^\alpha(l) - N^\alpha \Delta u_i^\alpha(u), \quad (6.30)$$

where,  $N^\alpha$  are the shape functions. Assuming a linear variation in the displacement field ( $\alpha = 4$ ) on the upper and lower surface, the interpolation functions for the mapped coordinate system are as given by Reddy [36]. A typical element is shown in Figure 6.5. Figure 6.6 illustrates the normal crack opening displacement as defined for the lower surface (with a linear variation in the displacement field). Substituting the interpolation functions into the principle of virtual work yields:

$$\begin{aligned}
& \int_{\mathfrak{b}_{\beta_c^u}(t)} k_y \left[ N^\beta \Delta u_j^\beta(u) - N^\beta \Delta u_j^\beta(l) \right] \delta N^\alpha \Delta u_i^\alpha(u) dS + \int_{\mathfrak{b}_{\beta_c^u}(t)} \Delta T_i^R \delta N^\alpha \Delta u_i^\alpha(u) dS \\
& + \int_{\mathfrak{b}_{\beta_c^l}(t)} k_y \left[ N^\beta \Delta u_j^\beta(l) - N^\beta \Delta u_j^\beta(u) \right] \delta N^\alpha \Delta u_i^\alpha(l) dS + \int_{\mathfrak{b}_{\beta_c^l}(t)} \Delta T_i^R \delta N^\alpha \Delta u_i^\alpha(l) dS \\
& = - \int_{\mathfrak{b}_{\beta_c^u}(t)} T_i(t) \delta N^\alpha \Delta u_i^\alpha(u) dS - \int_{\mathfrak{b}_{\beta_c^l}(t)} T_i(t) \delta N^\alpha \Delta u_i^\alpha(l) dS.
\end{aligned} \tag{6.31}$$

Because both the upper and lower surfaces are identical in the undeformed coordinate system the shape functions are equal. Equation 6.31 thus simplifies to the following:

$$\begin{aligned}
& \int_{\mathfrak{b}_{\beta_c^u}(t)} k_y N^\beta \left[ \Delta u_j^\beta(u) - \Delta u_j^\beta(l) \right] \delta N^\alpha \Delta u_i^\alpha(u) dS + \int_{\mathfrak{b}_{\beta_c^u}(t)} \Delta T_i^R \delta N^\alpha \Delta u_i^\alpha(u) dS \\
& + \int_{\mathfrak{b}_{\beta_c^l}(t)} k_y N^\beta \left[ \Delta u_j^\beta(l) - \Delta u_j^\beta(u) \right] \delta N^\alpha \Delta u_i^\alpha(l) dS + \int_{\mathfrak{b}_{\beta_c^l}(t)} \Delta T_i^R \delta N^\alpha \Delta u_i^\alpha(l) dS \\
& = - \int_{\mathfrak{b}_{\beta_c^u}(t)} T_i(t) \delta N^\alpha \Delta u_i^\alpha(u) dS - \int_{\mathfrak{b}_{\beta_c^l}(t)} T_i(t) \delta N^\alpha \Delta u_i^\alpha(l) dS.
\end{aligned} \tag{6.32}$$

Factoring out the virtual displacements,  $\delta \Delta u_i^\beta(u)$  and  $\delta \Delta u_i^\beta(l)$ , the principle of virtual work yields the following equilibrium equations for the upper and lower surfaces:

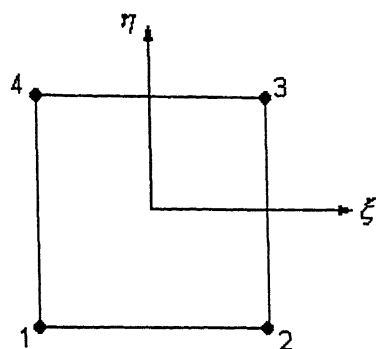


Figure 6.5 Parent element for interpolation and integration.

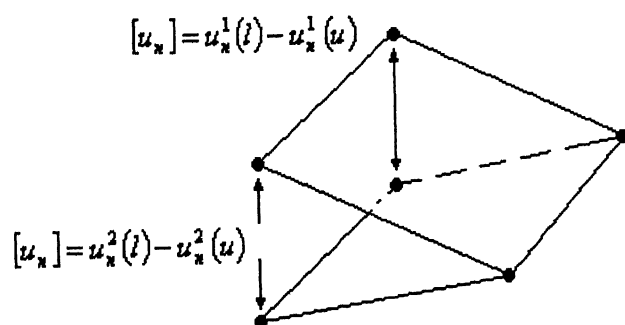


Figure 6.6 Crack opening displacement in Mode I.

$$\int_{\mathbb{B}_{\beta_c^u}(t)} k_y N^\alpha N^\beta [\Delta u_j^\beta(u) - \Delta u_j^\beta(l)] dS + \int_{\mathbb{B}_{\beta_c^u}(t)} \Delta T_i^R N^\alpha dS = - \int_{\mathbb{B}_{\beta_c^u}(t)} T_i(t) N^\alpha dS, \quad (6.33)$$

$$\int_{\mathbb{B}_{\beta_c^l}(t)} k_y N^\alpha N^\beta [\Delta u_j^\beta(l) - \Delta u_j^\beta(u)] dS + \int_{\mathbb{B}_{\beta_c^l}(t)} \Delta T_i^R N^\alpha dS = - \int_{\mathbb{B}_{\beta_c^l}(t)} T_i(t) N^\alpha dS. \quad (6.34)$$

The above may be written in matrix notation:

$$[K_y(u)] \left\{ \left\{ \Delta u_j^\beta(u) \right\} - \left\{ \Delta u_j^\beta(l) \right\} \right\} = \{ F_i(u) \}, \quad (6.35)$$

$$[K_y(l)] \left\{ \left\{ \Delta u_j^\beta(l) \right\} - \left\{ \Delta u_j^\beta(u) \right\} \right\} = \{ F_i(l) \}, \quad (6.36)$$

where,

$$K_y^{\alpha\beta}(l) = \int_{\mathbb{B}_{\beta_c^l}(t)} k_y N^\alpha N^\beta dS, \quad F_i^\alpha(l) = - \int_{\mathbb{B}_{\beta_c^l}(t)} T_i(t) N^\alpha dS, \quad (6.37)$$

$$K_y^{\alpha\beta}(u) = \int_{\mathbb{B}_{\beta_c^u}(t)} k_y N^\alpha N^\beta dS, \quad F_i^\alpha(u) = - \int_{\mathbb{B}_{\beta_c^u}(t)} T_i(t) N^\alpha dS. \quad (6.38)$$

Rearranging and combining Equations 6.35 and 6.36 yields:

$$\begin{bmatrix} [K_y(l)] & [-K_y(l)] \\ [-K_y(u)] & [K_y(u)] \end{bmatrix} \left\{ \begin{Bmatrix} \Delta u_j^\beta(l) \\ \Delta u_j^\beta(u) \end{Bmatrix} \right\} = \begin{Bmatrix} \{ F_i(l) \} \\ \{ F_i(u) \} \end{Bmatrix} \quad (6.39)$$

Eq. (49) represents the local element sub-matrices in the  $p$ ,  $n$ , and  $s$  directions. Expanding Equation 6.39 in the  $p$ ,  $n$ , and  $s$  directions one can obtain a general form:

$$\begin{bmatrix} [K_{lower}] & [-K_{lower}] \\ [-K_{upper}] & [K_{upper}] \end{bmatrix} \left\{ \begin{Bmatrix} \Delta u_{lower} \\ \Delta u_{upper} \end{Bmatrix} \right\} = \begin{Bmatrix} \{ F_{lower} \} \\ \{ F_{upper} \} \end{Bmatrix} \quad (6.40)$$

where,  $[K_{lower}]$  and  $[F_{lower}]$ , and  $[K_{upper}]$  and  $[F_{upper}]$  represent the assembled stiffness matrices and force vectors for the lower and upper surface, respectively. In addition,  $\{\Delta u_{lower}\}$ , and  $\{\Delta u_{upper}\}$  are the local displacement vectors.

### 6.3.3 Global assembly

One can expand Equation 6.40 in the  $p$ ,  $n$ , and  $s$  directions to form element submatrices. For simplification in assembly, one only has to form the stiffness matrix associated with the lower surface. For example, if  $\alpha = 4$

(Linear interpolation),  $[K_y(l)]$  would be a 4 x 4 matrix; and  $[K_{lower}]$ , a 12 x 12 matrix, would be assembled in the following manner:

$$\begin{bmatrix} K_p^{11} & 0 & 0 & K_p^{12} & 0 & 0 & K_p^{13} & 0 & 0 & K_p^{14} & 0 & 0 \\ 0 & K_n^{11} & 0 & 0 & K_n^{12} & 0 & 0 & K_n^{13} & 0 & 0 & K_n^{14} & 0 \\ 0 & 0 & K_s^{11} & 0 & 0 & K_s^{12} & 0 & 0 & K_s^{13} & 0 & 0 & K_s^{14} \\ K_p^{21} & 0 & 0 & K_p^{22} & 0 & 0 & K_p^{23} & 0 & 0 & K_p^{24} & 0 & 0 \\ 0 & K_n^{21} & 0 & 0 & K_n^{22} & 0 & 0 & K_n^{23} & 0 & 0 & K_n^{24} & 0 \\ 0 & 0 & K_s^{21} & 0 & 0 & K_s^{22} & 0 & 0 & K_s^{23} & 0 & 0 & K_s^{24} \\ K_p^{31} & 0 & 0 & K_p^{32} & 0 & 0 & K_p^{33} & 0 & 0 & K_p^{34} & 0 & 0 \\ 0 & K_n^{31} & 0 & 0 & K_n^{32} & 0 & 0 & K_n^{33} & 0 & 0 & K_n^{34} & 0 \\ 0 & 0 & K_s^{31} & 0 & 0 & K_s^{32} & 0 & 0 & K_s^{33} & 0 & 0 & K_s^{34} \\ K_p^{41} & 0 & 0 & K_p^{42} & 0 & 0 & K_p^{43} & 0 & 0 & K_p^{44} & 0 & 0 \\ 0 & K_n^{41} & 0 & 0 & K_n^{42} & 0 & 0 & K_n^{43} & 0 & 0 & K_n^{44} & 0 \\ 0 & 0 & K_s^{41} & 0 & 0 & K_s^{42} & 0 & 0 & K_s^{43} & 0 & 0 & K_s^{44} \end{bmatrix} \quad (6.41)$$

Knowing  $[K_{lower}]$  and assembling the force vector,  $[F_{lower}]$ , one can write local equilibrium in terms of the lower surface:

required. Thus the main program uses the subroutine to construct the stiffness matrices and load vectors of the cohesive elements in the model, and then assembles these matrices and load vectors, together with those of the bulk elements to construct the global equations. Incremental analysis with the Newton Raphson iterative scheme is used.

Eight noded isoparametric element has been used as the cohesive element. Since the upper and the lower surfaces of the element are co-planar in the initial configuration, and since the integration has to be performed only on the areas, four Gauss points are used. The stiffness and internal load of the element is assumed to be contributed only by the Gauss points. Hence, the criterion of failure of the element is that, when  $\lambda$  becomes unity at a particular Gauss point, the contributions of that Gauss point to the stiffness and load vector of the element vanish, and the element is assumed to have failed, when  $\lambda$  exceeds unity at all the four Gauss points.

#### 6.4.1 One Element Tension Test Problem

To test the subroutine, a simple tension test problem (as shown in Figure 6.7), with one bulk element (8-noded isoparametric) and one cohesive element, has been solved under displacement controlled loading. Displacement controlled loading is used because convergence problems arise with load controlled loading when the number of elements in the problem is less, due to the negative stiffness encountered during the softening of the cohesive elements.

The nuclear reactor pressure vessel steel SA 508 has been used as the material. Deformation plasticity model has been used for the bulk elements, with Young's Modulus equal to 210 GPa, yield strength 450 MPa, hardening exponent 10.6, and yield offset equal to 0.91 [37].

The parameters of the cohesive element have been chosen in the following manner:  $\sigma_{max}$  is chosen same as the yield strength of the bulk material (450 MPa). The value of  $\delta_n$  is chosen such that the initial stiffness of the cohesive element is comparable to that of the bulk material. This gives a value of 0.01 mm for  $\delta_n$ . Since the problem is purely of mode I, the shear terms have been ignored.

The boundary conditions used are as shown in Figure 6.7. Based on the above, the problem is solved, and the traction-displacement response of the cohesive element, as obtained from the

solution is plotted along with the material constitutive curve in Figure 6.8. As expected, the cohesive element obeys the constitutive model used.

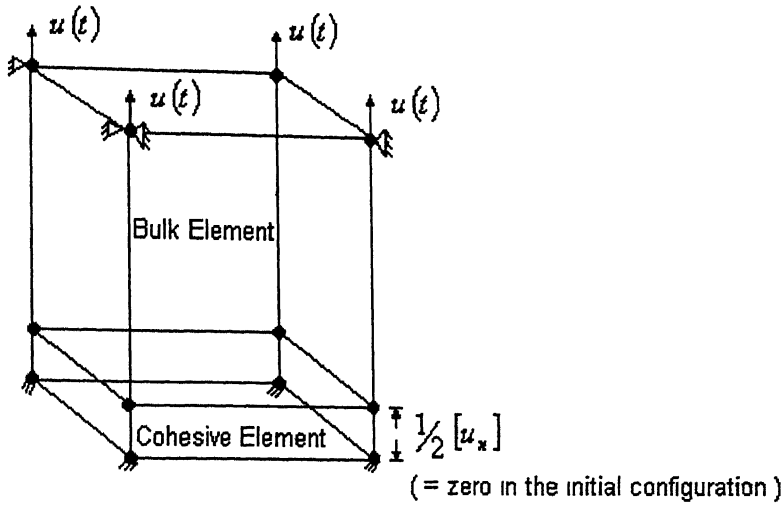


Figure 6.7 One-element Tension test problem.

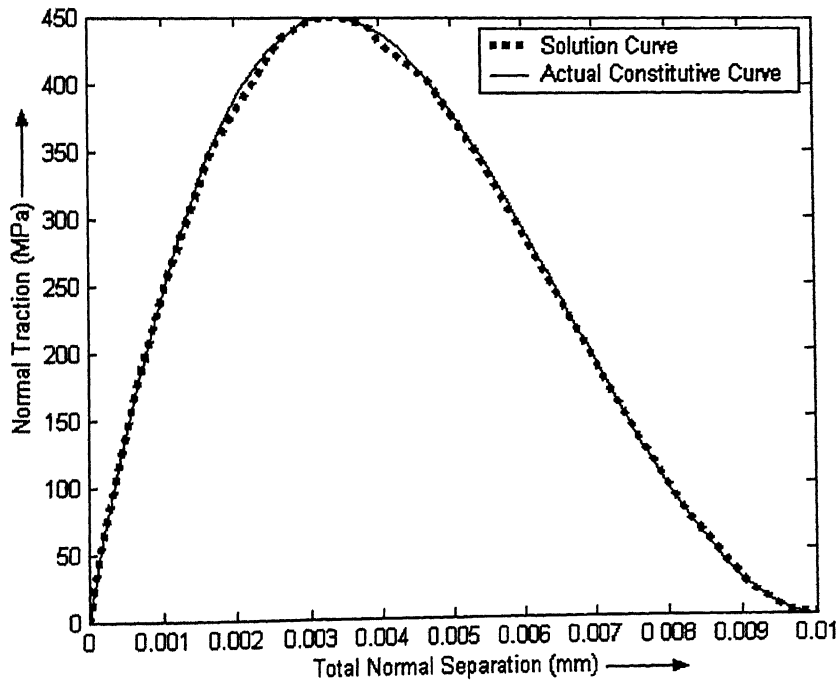


Figure 6.8 Response of the cohesive element under Tension test problem.

### 6.4.2 Crack Growth Analysis of a DCB Specimen

Figure 6.9 shows the Double Cantilever Beam (DCB) Specimen used for the analysis. The half thickness of the beam ( $h$ ), as shown in the Figure is taken as 10 mm. The total length of the Beam is taken as 200 mm, and the width of the beam is taken equal to 100 mm. The value of the initial crack length ( $a_i$ ) has been taken to be 5 mm. The material properties and the values of the parameters of the cohesive zone are taken same as described in section 6.4.1.

Only the symmetrical half of the specimen has been modeled (exploiting the symmetry about the crack plane), with a layer of 8-noded cohesive elements throughout the crack plane (except the initial de-bonded surface), as shown in Figure 6.9(b). The size of the cohesive elements in the direction of crack propagation is 1.67 mm. Thus, crack extension in increments of 1.67 mm is obtained. Also, 8-noded isoparametric elements have been used to discretize the bulk material. Again, a displacement controlled loading has been considered. The results of the analysis are presented in section 6.4.3.

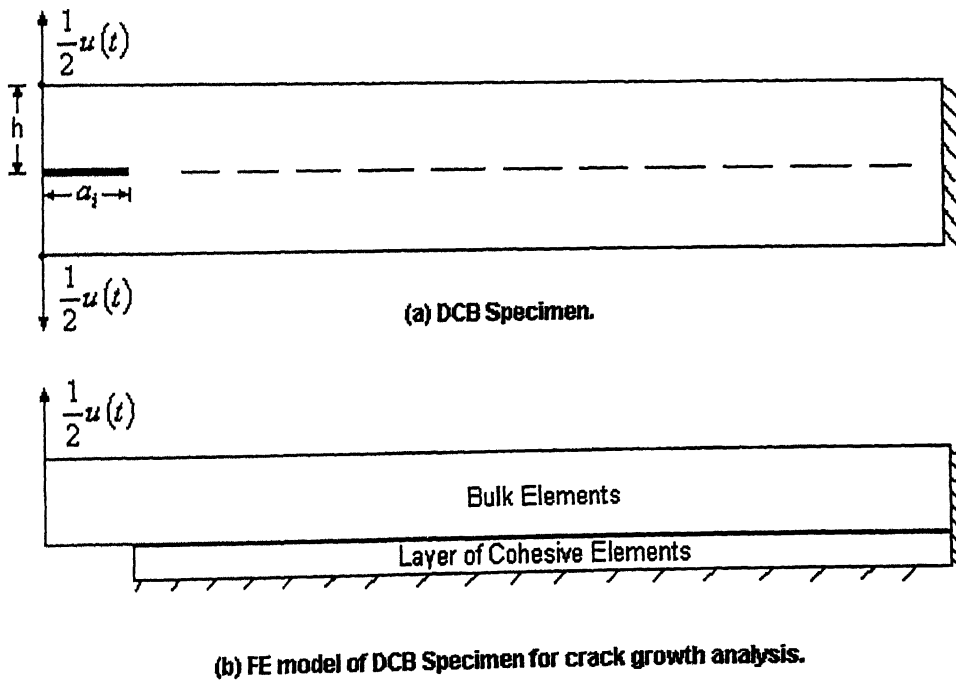


Figure 6.9 Crack growth analysis of a DCB Specimen.



### 6.4.3 Results and Discussion

Figure 6.10 shows the crack propagation with increasing load-line displacement. The crack starts growing when the load-line displacement reaches a value of about 0.5 mm and continues to grow up to a crack length of about 29 mm, after which, the rate of crack growth with respect to the load line displacement becomes very small. Figure 6.11 shows the load-displacement relationship at the load line. Before the crack starts growing, the load increases linearly with the displacement. As the crack starts propagating, the load decreases due to the increase in the compliance with increasing crack length.

Energy release rate ( $G_I$ ) has been calculated using the load-displacement curve and is plotted in Figure 6.12. The nature of the curve matches very well with that of the crack-growth resistance curves available in the literature [22, 37].

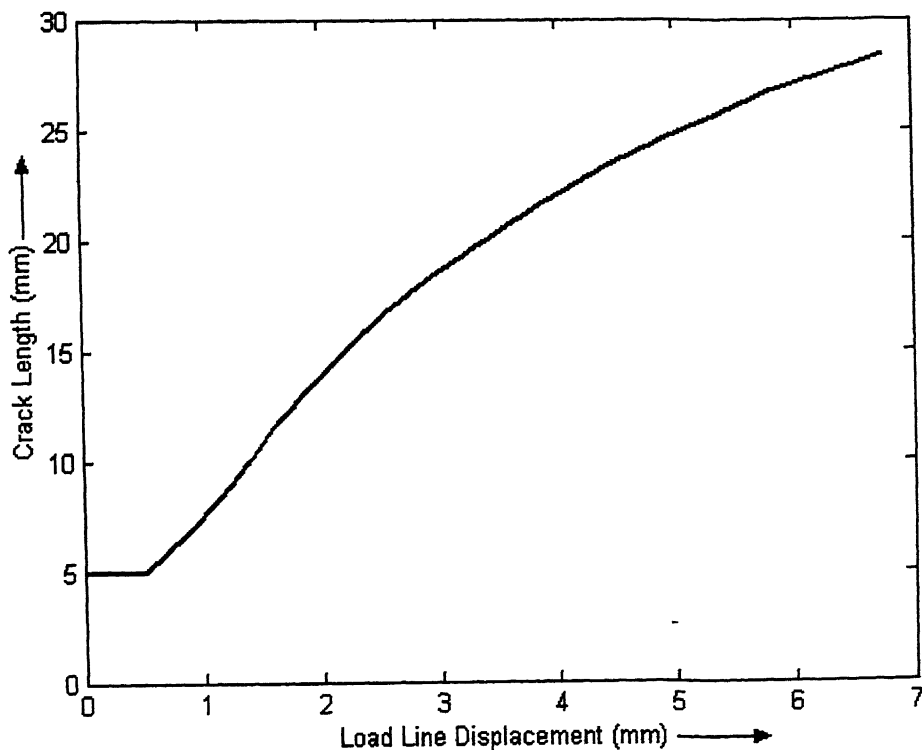
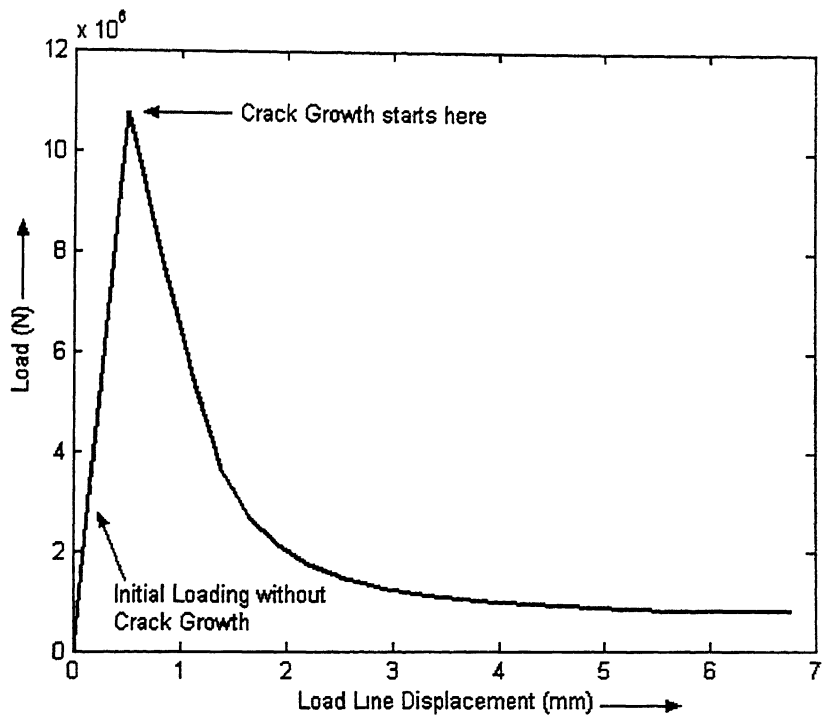
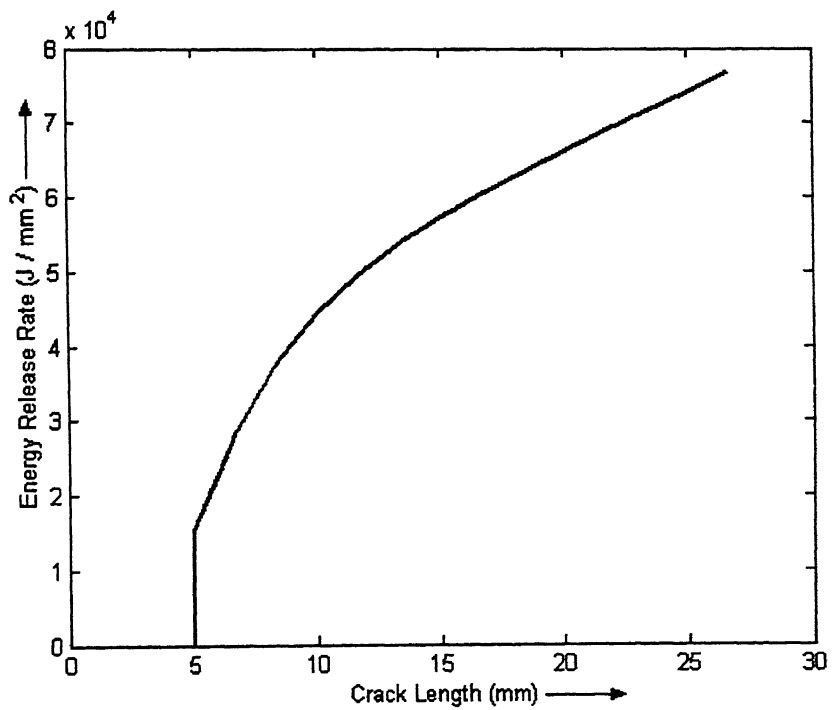


Figure 6.10 Crack propagation with increasing load line displacement.



**Figure 6.11 Variation of crack opening load with the load-line displacement.**



**Figure 6.12 Crack growth resistance curve.**

### 6.4.3 Crack Growth Analysis of a nozzle-corner crack

The method is finally used for the crack growth analysis of a given nozzle-corner crack. A quarter-circular crack of 60 mm depth is taken as the initial crack configuration for analysis. The nozzle-vessel-intersection is meshed in ABAQUS in the same manner as described in Chapter 4, except that 8-noded isoparametric brick elements are used in the region near the crack, instead of 20-noded brick elements. In addition, 200 cohesive elements are incorporated in to the FE model near the crack, as shown in Figure 6.13. The region shown protruded in the Figure is additionally modeled here and first meshed with 8-noded isoparametric brick elements in compatible mode with the brick elements in the region near the crack. These elements are then declared as user elements in the input file generated by ABAQUS and the upper and lower surfaces of these elements are merged together by editing the coordinates of the nodes on the upper (outer) surface.

As seen in Figure 6.13, 40 cohesive elements are taken along the crack profile and 5 elements are taken in the direction normal to the profile. The size of each cohesive element is about 2 mm along the profile and 1 mm normal to the profile.

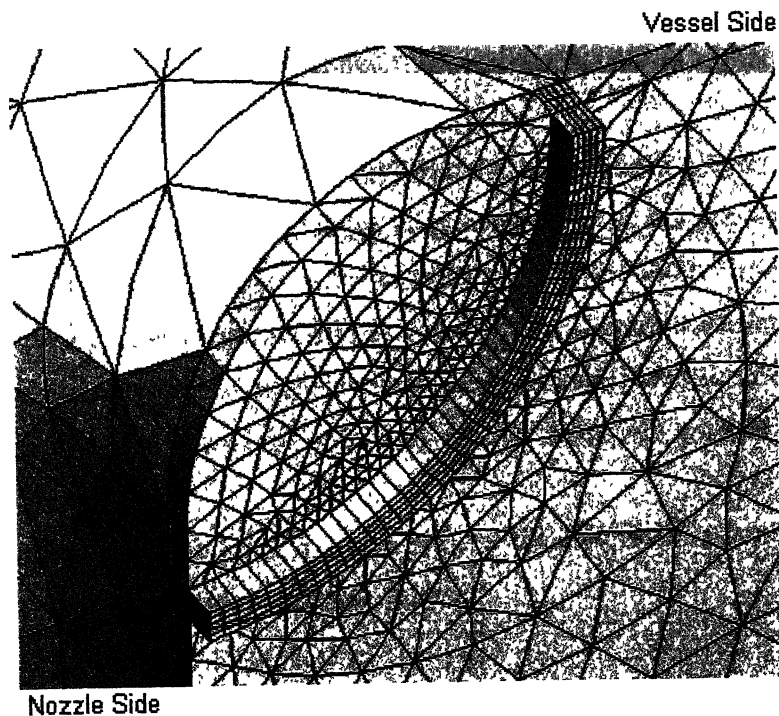


Figure 6.13 Cohesive elements near the crack.

The material properties of the bulk material and the parameters of the cohesive zone are taken in the similar manner as described in section 6.4.1. Internal pressure load of 15 MPa is applied and the boundary conditions are taken same as described in Chapter 4. In addition, the upper surface of the cohesive zone is fixed in all directions.

Load controlled incremental analysis is performed. The solution converged up to a pressure of 9.1 MPa, and after that, the rate of convergence became very low, requiring very small time increments. The crack growth results obtained from the analysis are presented in the following section.

#### **6.4.4 Results and Discussion**

Figures 6.14-6.19 show the status of the cohesive elements (failed or surviving), at different values of internal pressure. The elements shown in red have failed, and the elements shown in green are still surviving. The elements in which all the four gauss points have failed, are considered to have failed. The boundary between the two colours thus represents the current crack profile.

As seen in Figure 6.14, the crack has not yet started propagating at a pressure of 7 MPa. At a pressure of about 7.5 MPa, the crack has started propagating at the nozzle side. This is consistent with the SIF results obtained in Chapter 4, wherein it is seen that the SIF is higher at the nozzle-side of the crack.

It is further observed from Figures 6.15-6.19 that the rate of crack propagation increases with the increasing pressure, once the crack has started growing. Finally, at a pressure of about 9.1 MPa, the crack has grown by about 4 mm in the nozzle direction and about 1 mm in the vessel direction, thereby assuming almost a quarter-elliptical shape. This is again consistent with the SIF results, which showed that for a quarter-elliptical crack, the percentage variation of SIF is less than that for a quarter-circular crack, and hence an initially circular crack will grow in such a way to assume an elliptical shape.

Since the total crack growth is of the same order of the size of the cohesive elements, a finer mesh can be expected to produce even better results.

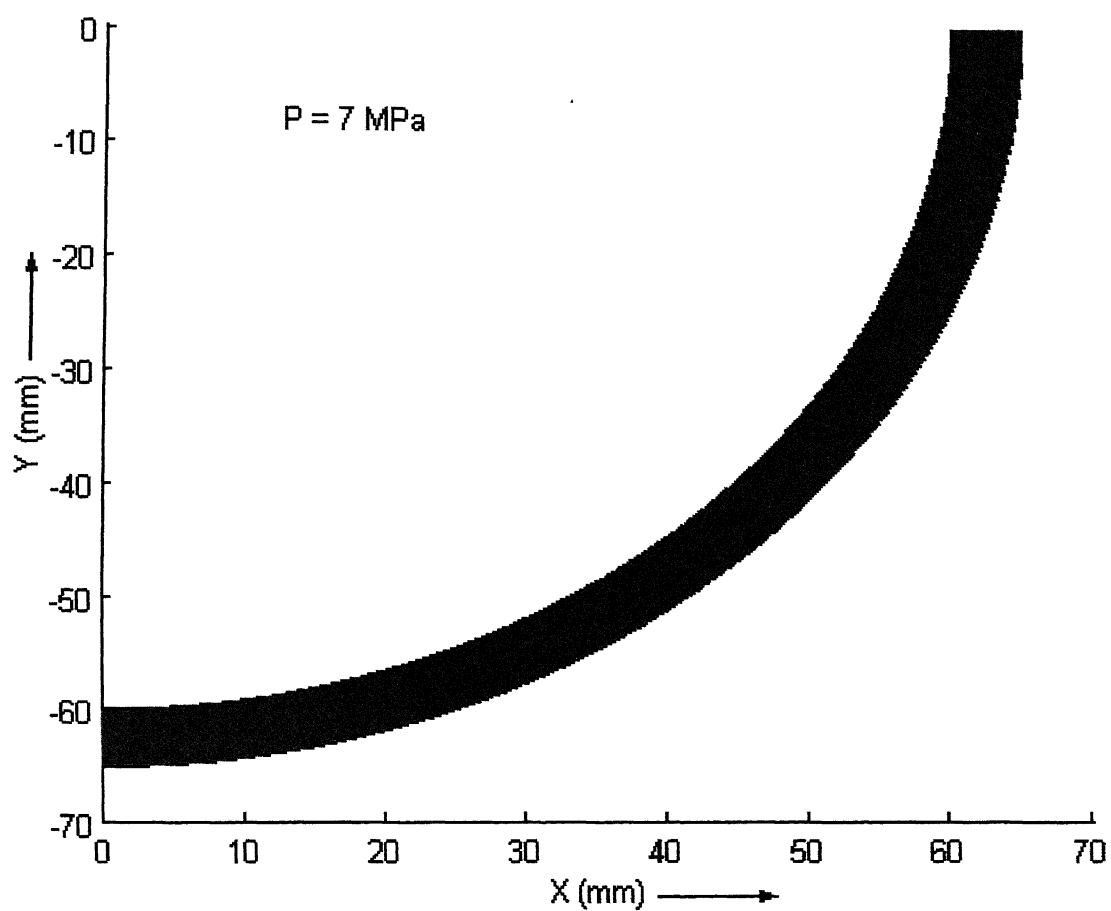


**Figure 6.14 Status of cohesive elements at internal pressure of 7 MPa.**

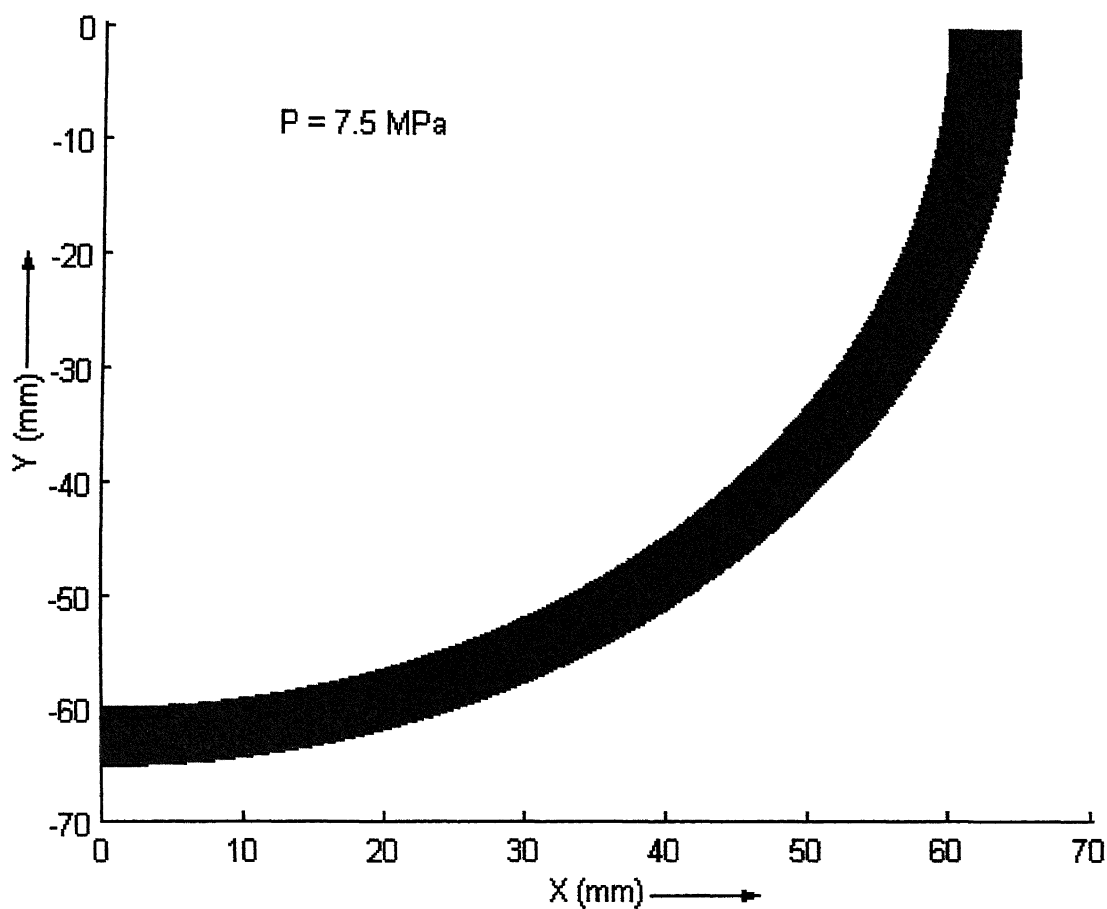


**Figure 6.15 Status of cohesive elements at internal pressure of 7.5 MPa.**

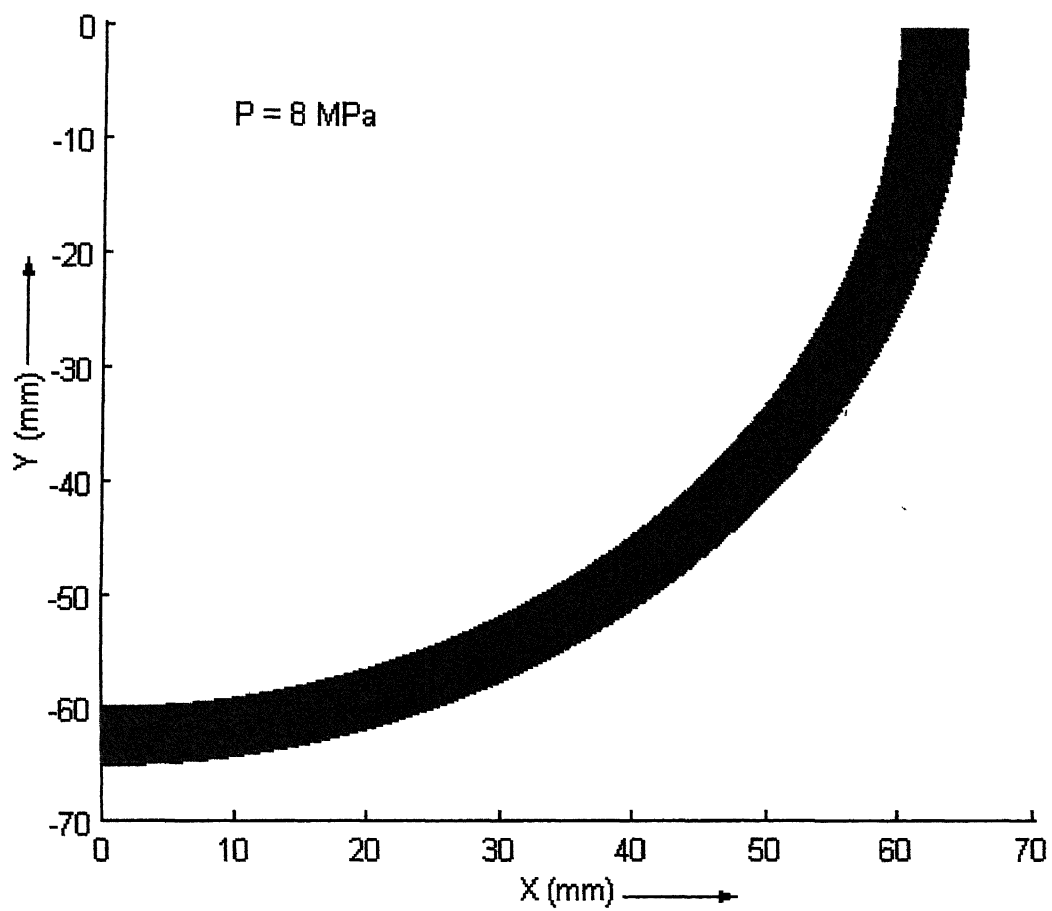


**Figure 6.16 Status of cohesive elements at internal pressure of 8 MPa.**

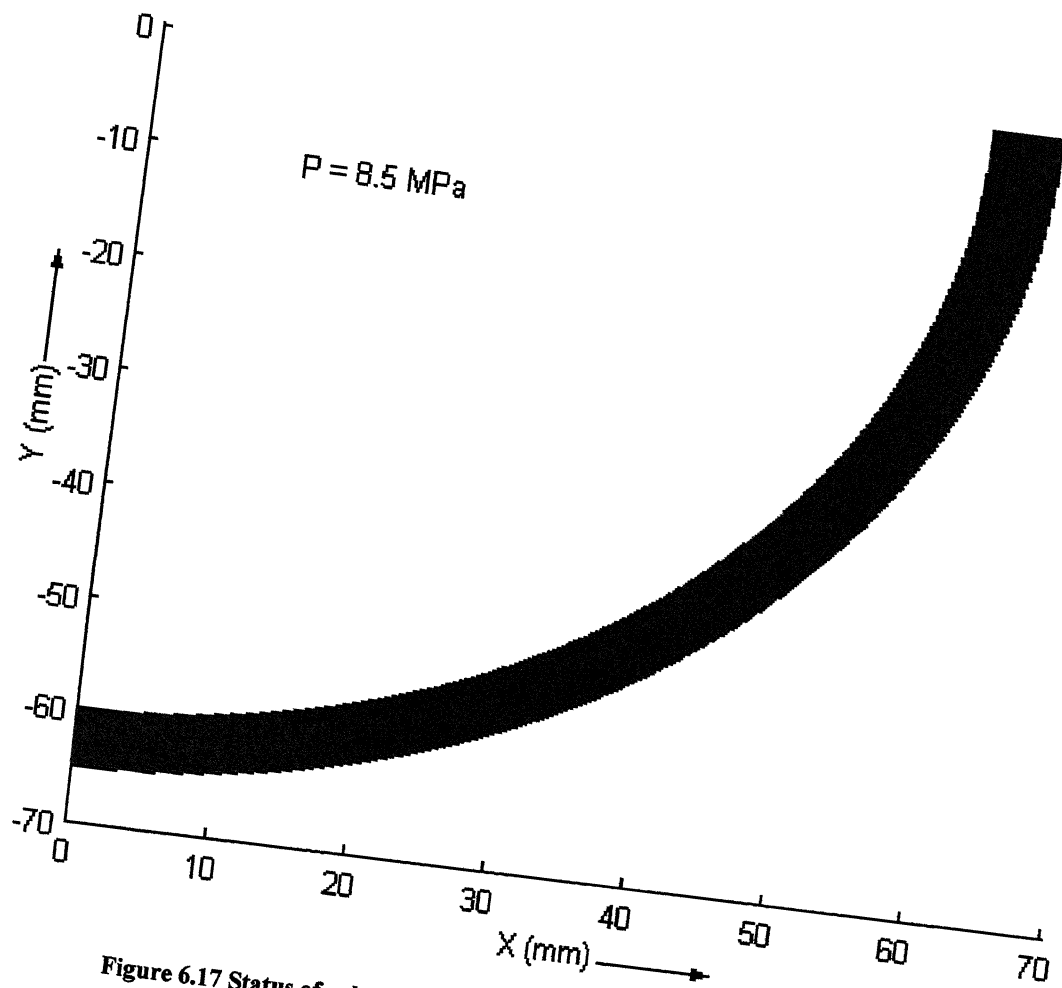
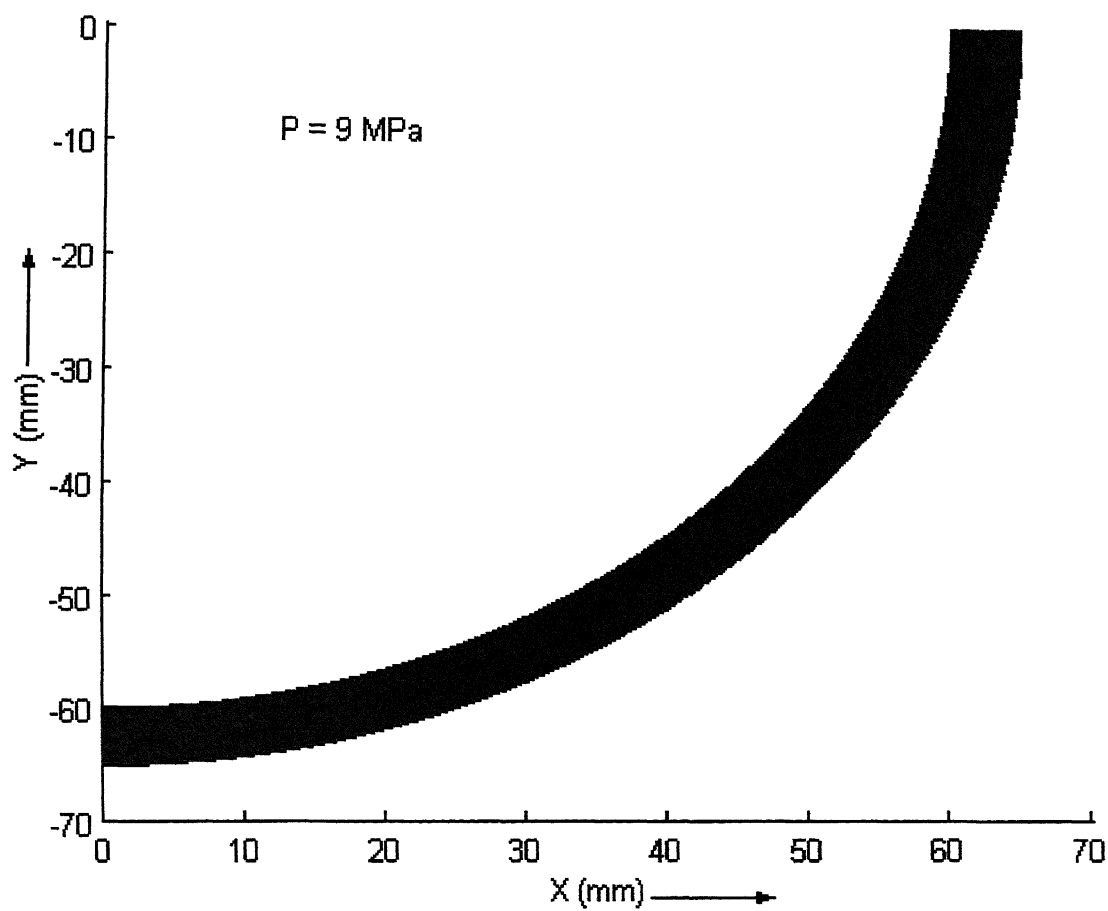
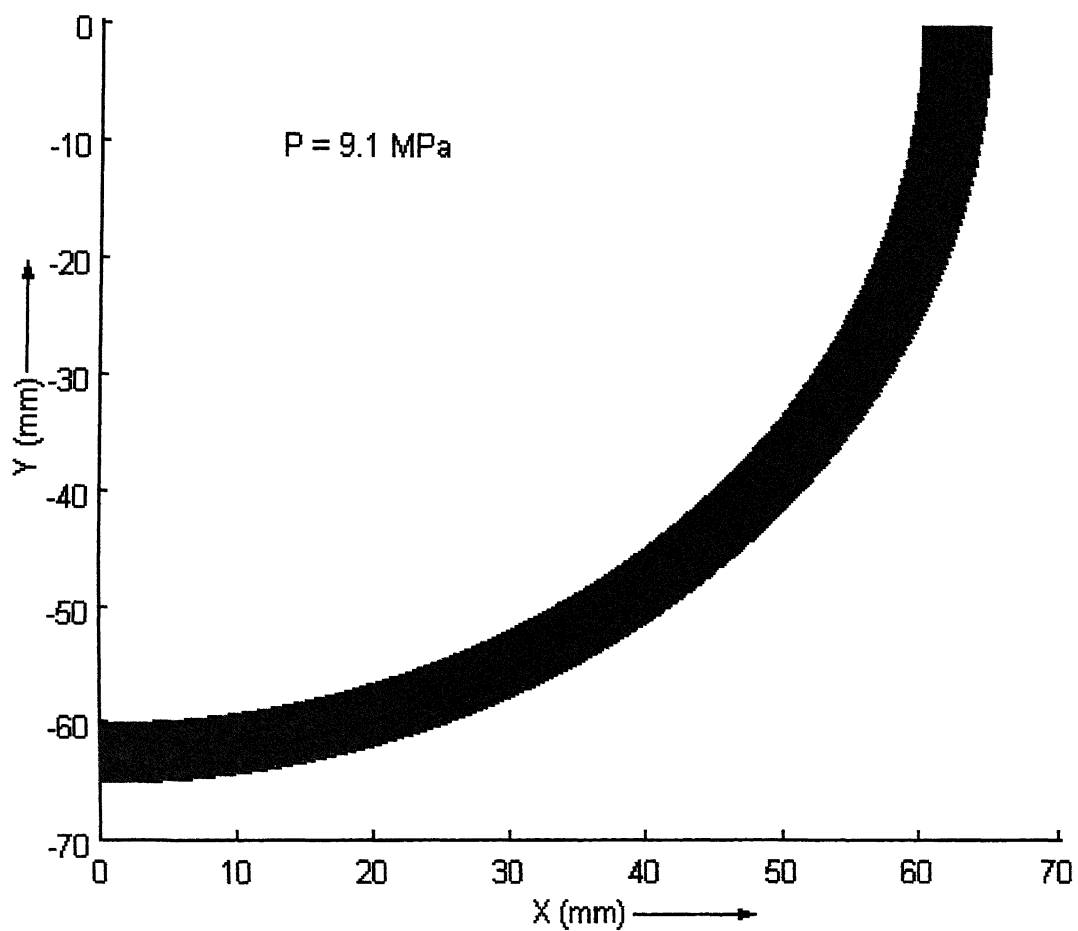


Figure 6.17 Status of cohesive elements at internal pressure of 8.5 MPa.





**Figure 6.18 Status of cohesive elements at internal pressure of 9 MPa.**



**Figure 6.19 Status of cohesive elements at internal pressure of 9.1 MPa.**

## 6.5 Closure

A three-dimensional formulation of the cohesive zone method for crack growth analysis has been presented. The method has been applied for the crack growth analysis of a DCB specimen and the results are found to match qualitatively well with the available literature. The methodology is then used for the estimation of stable crack growth in a given quarter-circular nozzle-corner crack under a constant internal pressure load (normal operational load). The pattern of crack growth has been found to be consistent with the pattern of variation of SIF along the profile of a quarter-circular crack as estimated in Chapter 4. The method can be conveniently extended to estimate the stable crack growth during a Pressurized thermal shock also.

## Chapter 7

# CONCLUSIONS AND SCOPE FOR FUTURE WORK

### 7.1 Conclusions

Structural Integrity of nuclear reactor pressure vessels with nozzle-corner cracks has been investigated under normal operational condition, and also under a loss of coolant accident. Linear Elastic Fracture Mechanics has been used for the purpose and the crack characterizing parameter, Stress Intensity Factor, has been evaluated along the profile of the nozzle-corner cracks for different geometrical and crack parameters. The results have been found to be within 4 % of accuracy. The individual effects of different parameters on Stress Intensity Factors have been studied. As an attempt to predict the stable crack growth of nozzle-corner cracks, the cohesive zone technique for three dimensional crack problems has been presented, and is applied for the crack growth analysis of a Double Cantilever Beam Specimen. The following are the main conclusions drawn from the present work:

- 1) Use of quarter point elements developed by a simple shift of mid side nodes, rather than the face-collapsed wedge shape quarter point elements, to simulate the singularity near the crack, has been found to produce sufficiently accurate results.
- 2) Under the normal operational load condition, sufficient factor of safety (greater than 5) exists, even for the half thickness cracks. Nozzle side of the corner-crack has a higher value of Stress Intensity Factor, and hence, there seems to be a possibility of Leak-before-Break.

- 3) The normalized average Stress Intensity Factor has been found to be almost independent of the crack aspect ratio.
- 4) The Stress Intensity Factor has been found to bear simple relationships with all the parameters individually, thereby indicating the possibility of development of more accurate empirical relations for its calculation, than already available in the literature.
- 5) Under the faulted condition, LOCA, the cracks sufficiently safe earlier, may become critical. Also, since the vessel side of the corner-crack has a higher value of Stress Intensity Factor during the faulted condition, the possibility of Leak-before-Break does not seem to be there.
- 6) The cohesive zone technique has been realized to be a powerful tool for the estimation of stable crack growth. The consistency between the pattern of growth of the given nozzle-corner crack and that of SIF variation over the crack profile, suggests that the crack growth results are satisfactorily well.

## 7.2 Scope for Future Work

The present work provides some insight to the assessment of structural integrity of nuclear reactor pressure vessels having nozzle corner cracks, but the following work is also of interest and can be pursued as a future work:

- 1) Elasto-Plastic Fracture Mechanics can be applied to capture the effect of plastic zone near the crack. J-integral can be evaluated over the crack profile, following an Elasto-Plastic stress analysis.
- 2) Stress Intensity Factor and J-integral database can be generated, followed by development of empirical relations for their calculation.
- 3) The possibility of crack arrest, in the event of a crack propagating after becoming critical, needs to be assessed.
- 4) The amount of stable crack growth during a Pressurized thermal shock can be estimated, so that, the number of such transients that the pressure vessel can withstand before becoming operationally unsafe, can be predicted.

## References

1. Rashid, Y. and Gilman, *First International Conference on Structural Mechanics in Reactor Technology*, Berlin (1971).
2. Shah, R. and Kobayashi, A., *Engineering Fracture Mechanics*, vol. 3 (1971).
3. Hellen, T.K. and Dowling, A.R., Three-dimensional Crack Analysis applied to an LWR Nozzle-Cylinder Intersection, *International Journal of Pressure Vessels and Piping*, vol. 3 (1975), pp. 57-74.
4. Schmitt, W., *International Journal of Pressure Vessels and Piping*, vol. 3 (1975).
5. Schmitt, W., Analysis of a Crack in a Nuclear Pressure Vessel Nozzle using Three-Dimensional Crack Tip Singularity Elements, *International Journal of Pressure Vessels and Piping*, vol. 3 (1975), pp. 123-136.
6. Broekhoven, M., *Cracks and Fracture*, ASTM STP, vol. 601 (1976), pp. 535-558.
7. Besuner, P., Cohen, L., McLean, J., *ibid.*, G4/5.
8. Kobayashi A., *Fourth International Conference on Structural Mechanics in Reactor Technology*, San Francisco (1977) G4/4.
9. Mohamed, M.A. and Schroeder, J., Stress Intensity Factor Solution for Crotch-Corner Cracks of Tee-Intersections of Cylindrical Shells, *International Journal of Fracture*, vol. 14 (1978), pp. 605-621.
10. Schmitt, W., Keim, E., Wellen, R. and Bartholome, G., Linear Elastic Stress Intensity Factors for Cracks in Nuclear Pressure Vessel Nozzles under Pressure and Temperature Loading, *International Journal of Pressure Vessels and Piping*, vol. 8 (1980), pp. 41-68.
11. Guozhong, Chai and Qichao, Hong, Approximate Stress Intensity Factor Solutions for Nozzle Corner Cracks, *International Journal of Pressure Vessels and Piping*, vol. 42 (1990), pp. 75-96.
12. Baisong, Wang, Dinggen, Xu, Weijuan, Ye, Yinbiao, He, and Xingyun, Liang, Computation of SIF of Corner Crack in Interior Wall of Nuclear Vessel, *International Journal of Pressure Vessels and Piping*, vol. 51 (1992), pp. 349-359.
13. Derby, R., *Experimental Mechanics*, vol. 12 (1972), pp. 580-584.
14. Broekhoven, M. and Ruijtenbeek, Van De, *Third International Conference on Structural Mechanics in Reactor Technology*, London (1975) G4/7.

15. Smith, C., Jolles, M. and Peters, W., Rep. VPI-E-76-25, Virginia Polytechnic Institute and State University, Nov. (1976).
16. Ruiz, C., *Strain*, vol. 9 (1973), pp. 7-9.
17. Smith, C.W., Peters, W.H. and Jolles, M.I., Stress Intensity Factors for Reactor Vessel Nozzle Cracks, *Transactions of the ASME, Journal of Pressure Vessel Technology*, vol. 100 (1978), pp. 141-149.
18. ASME Boiler and Pressure Vessel Code, July 1977.
19. Moini, H., Mitchell, T.P., Stress Analysis of a Thick-Walled Pressure Vessel Nozzle Junction, *International Journal of Pressure Vessels and Piping*, vol. 46 (1991), pp. 67-74.
20. Kim, I.S. and Kang, S.S., Dynamic Strain Aging in SA 508-Class 3 Pressure Vessel Steel, *International Journal of Pressure Vessels and Piping*, vol. 62 (1995), pp. 123-129.
21. Sattari-Far, Iradj, Constraint effects on behaviour of Surface Cracks in Cladded Reactor Pressure Vessels subjected to PTS transients, *International Journal of Pressure Vessels and Piping*, vol. 67 (1996), pp. 185-197.
22. Kumar, P., *Elements of Fracture Mechanics*, Wheeler Publishing, New Delhi, 1999.
23. Kanninen, M.F. and Popelar, C.H., *Advanced Fracture Mechanics*, Oxford University Press, New York, 1985.
24. Kassir, M., and Sih, G.C., Three Dimensional Stress Distribution Around an Elliptical Crack Under Arbitrary Loadings, *Transactions of the ASME, Journal of Applied Mechanics*, vol. 33 (1966), pp. 601-611.
25. Zienkiewicz, O.C., *The Finite Element Method*, Tata McGraw-Hill Publishing Company Limited, 1979.
26. Henshell, R.D. and Shaw, K.G., Crack Tip Elements are Unnecessary, *International Journal of Numerical Methods in Engineering*, vol. 9 (1975), pp. 495-509.
27. Barsoum, R.S., Triangular Quarter Point Elements as Elastic and Perfectly Elastic Crack Tip Elements, *International Journal of Numerical Methods in Engineering*, vol. 8 (1974), pp. 537-45.
28. Hibbit, H.D., Some Properties of Singular Isoparametric Elements, *International Journal of Numerical Methods in Engineering*, vol. 11 (1977), pp. 180-4.
29. Bathe, K.J., *Finite Element Procedures*, Prentice Hall of India, New Delhi, 2001.

30. Heliot, J., Labbens, R. and Pellissier-Tanon, A., Solution of Three Dimensional Crack Problems using the Boundary Integral Equation Method, *Proceedings of the second international conference, University College, Swansea*, 1980.
31. Murakami, Y., *Stress Intensity Factors Handbook*, Pergamon Press, Oxford, 1987.
32. John F. Harvey, P.E., *Theory and Design of Pressure Vessels*, CBS Publishers and Distributors, 1987.
33. Kothandaraman, C.P., Subramanyan, S., *Heat and Mass Transfer Data Book*, New Age International (P) Limited, Publishers, 1989.
34. Foulk, J.W., Allen, D.H. and Helms, K.L.E., Formulation of a Three-Dimensional Cohesive Zone Model for Application to a Finite Element Algorithm, *Computer Methods in Applied Mechanics and Engineering*, vol. 183 (2000), pp. 51-66.
35. Tvergaard, V., Effect of Fibre Debonding in a Whisker-Reinforce Metal, *Material Science and Engineering A* vol. 125 (1990), pp. 203-213.
36. Reddy, J.N., *An Introduction to the Finite Element Method*, McGraw-Hill, Inc., 1993.
37. Blauel, J.G., Hodulak, L., Hollstein, T. and Voss, B., Material Characterization by J-R Curves of a 20MnMoNi55 Forging, *International Journal of Pressure Vessels and Piping*, vol. 17 (1984), pp. 139-62.



**A**145108



A145108